João Baptista Dias Moreira

Full Waveform Inversion based on Integer Programming Topology Optimization

São Paulo
2023

João Baptista Dias Moreira

Full Waveform Inversion based on Integer Programming Topology Optimization

Revised Version

Ph. D. Thesis submitted to the Escola Politécnica, University of São Paulo, in partial fulfilment of the requirements for the degree of Doctor of Science.

Concentration area:
Control and Mechanical Automation Engineering (3152)

Advisor:
Prof. Dr. Emílio Carlos Nelli Silva

São Paulo
2023

Este exemplar foi revisado e corrigido em relação à versão original, sob responsabilidade única do autor e com a anuência de seu orientador.

São Paulo, _____ de _____ de _____

Assinatura do autor: _____

Assinatura do orientador: _____

Catalogação-na-publicação

Dias Moreira, João Baptista. **Full Waveform Inversion based on Integer Programming Topology Optimization**. 2023. 119 p. Ph. D. Thesis (Doctor of Science) - Escola Politécnica, University of São Paulo, São Paulo, 2023.

Approved in:

Examination Committee

Prof. Dr.   _____

Institution: _____

Judgement: _____

Prof. Dr.   _____

Institution: _____

Judgement: _____

Prof. Dr.   _____

Institution: _____

Judgement: _____

Prof. Dr.   _____

Institution: _____

Judgement: _____

Prof. Dr.   _____

Institution: _____

Judgement: _____

ACKNOWLEDGEMENTS

RESUMO

Problemas inversos consistem na identificação das características de um sistema a partir da resposta a uma determinada excitação, e tem aplicações em diversas disciplinas tais como imageamento medicinal, detecção de danos, testes não destrutivos, e imageamento geofísico. Na geofísica de exploração, a Inversão de Forma de Onda (no inglês, FWI) consiste em utilizar dados sísmicos de reflexão e refração para reconstruir o campo de velocidades da subsuperfície. A inversão é particularmente desafiante para modelos de velocidade com corpos de sal, cujas interfaces com alto contraste entre propriedades materiais amplifica erros na estimação do caminho de onda e tempo de trânsito. O problema de identificação do sal é extremamente relevante devido à sua abundância em importantes sítios de exploração de hidrocarbonetos como o golfo do México e a bacia de Santos. Dessa forma, com o intuito de incorporar a hipótese de interfaces materiais dentro do modelo, assim guiando a inversão, é proposto utilizar um framework baseado na técnica de projeto estrutural Otimização Topológica (OT). Mais especificamente, o campo de velocidades é descrito por uma variável de projeto inteira, e o problema de otimização associado é resolvido por Programação Linear Inteira Sequencial. A função objetivo mede a diferença entre dados colhidos de uma enquete sísmica com dados gerados sinteticamente através de um modelo computacional. O gradiente é calculado pelo método adjunto e dois filtros de sensibilidade são utilizados. Um filtro baseado em Equação Diferencial Parcial típico de OT é aplicado para controlar o surgimento de inclusões espúrias, e um filtro de médias móveis é aplicado com intuito de estabilizar o processo de inversão. A implementação da propagação de ondas foi feita utilizado Spyro, um pacote python construido sobre a biblioteca de elementos finitos Firedrake. A otimização por variável inteira é realizada através da biblioteca IBM CPLEX. Com objetivo de validar a metodologia, inversão acústica é aplicada à reconstrução de inclusões simples, e a influência de paramêtros de filtragem e da configuração do problema são analizados. Por fim, a metodologia é aplicada a um problema FWI com modelo de velocidades típico da bacia de Santos. Para esse modelo, três casos são mostrados, reconstrução do sal, reconstrução do sal e do reservatório, e reconstrução das camadas abaixo do sal.

Palavras-chave: Otimização Topológica, Programação Linear Inteira, Inversão de Forma de onda, Modelo de sal

ABSTRACT

Inverse problems usually consist in identifying characteristics of a system based on its response to a certain input, and have many applications in disciplines such as medical imaging, damage detection, non-destructive testing, and geophysical imaging. In seismic exploration, Full Waveform Inversion (FWI) takes the wave equation into account by incorporating it as one of the constraints of the inverse problem which seeks to identify properties from the subsurface of the Earth. Hydrocarbon exploration sites in salt basin areas such as the Gulf of Mexico and in the Brazilian coast deep waters are specially challenging for velocity model building, since the contrast in material properties between the salt region and its surroundings amplifies perturbations in the measured data, consequently making it harder to correctly place the salt interfaces. With the objective of incorporating the presence of sharp interfaces into the model, this work proposes applying Sequential Integer Linear Programming to FWI formulated as a Topology Optimization problem. The identification procedure for the material parameters of the subsurface consist in minimizing an objective function subject to the acoustic wave equation as a constraint and with the acoustic velocity described by an integer design variable. The objective function measures the misfit between data collected from a seismic survey and data coming from a computational representation of the subsurface. The gradient evaluation is carried out using the adjoint method. Two sensitivity filters are employed, a spatial filter based on Partial Differential Equations limits spurious inclusions, while a moving average filter is used to stabilize the inversion process. Wave propagation is carried out using Spyro, a Finite Element Method (FEM) software for seismic aplications built on top of Firedrake. The gradient evaluation employs the adjoint method, and integer linear programming is carried out with using the IBM CPLEX optimization library. Results are shown for velocity models with one or more inclusions, as well a velocity model representative of the Santos basin. Three cases are analyzed with this model, salt reconstruction, salt and reservoir reconstruction and subsalt reconstruction.

Key words: Topology Optimization, Integer Linear Programming, Full Waveform Inversion, Salt model

LIST OF FIGURES

LIST OF TABLES

ACRONYMS

ABC   Absorbing Boundary Conditions

ABL   Absorbing Boundary Layer

BESO   Bi-directional Evolutionary Structural Optimization

BFGS   Broyden-Fletcher-Goldfarb-Shanno

CPML   Convolutional Perfectly Matched Layers

CFL   Courant-Friedrichs-Lewy

DSL   Domain Specific Language

EIT   Electrical Impedance Tomography

FDM   Finite Difference Method

FEM   Finite Element Method

FVM   Finite Volume Method

FWI   Full Waveform Inversion

GLL   Gauss-Lobato-Legendre

ILP   Integer Linear Programming

LP   Linear Programming

LS   Level Set

MIP   Mixed Integer Programming

MNL   Mean Noise Level

MTV   Modified Total Variation

NDT   Non-Destructive Testing

OBN   Ocean Bottom Node

PML   Perfectly Matched Layers

RAMP   Rational Approximation of Material Properties

SEM   Spectral Element Method

SIMP   Solid Isotropic Material with Penalization

TO   Topology Optimization

TOBS   Topology Optimization of Binary Structures

TV   Total Variation

UFL   Unified Form Language

NOTATION

a	Design variable
a_i	Design variable value for i^{th} material
$\mathbf{b}$	Body force per unit mass
$d_{s,r}$	s^{th} synthetic signal recorded at r^{th} receiver
f	Objective function
g	Objective function gradient
$\hat{g}$	Objective function gradient filtered by spatial filter
$\tilde{g}$	Objective function gradient filtered by spatial and stability filter
m	Stability filter first moment
M	Upper bound on update vector
N_s	Number of sources
N_r	Number of receivers
$p_{0,s}$	s^{th} synthetic wave field
p_s	s^{th} predicted wave field
r	Spatial filtering radius
s	Volumetric source
$\mathbf{u}$	Displacement field
v	Stability filter second moment
v_p	Acoustic wave speed
Δa	Update vector
Δa_P	Positive contribution to update vector
Δa_N	Negative contribution to update vector
γ_m	Forgetting factor for first moment
γ_v	Forgetting factor for second moment
ε	Strain tensor
η	Damping coefficient
κ	Bulk modulus
λ	First Lamé parameter
λ_s	Adjoint variable to the sth state equation
$\lambda_s^{\dagger}$	Adjoint variable to the sth state equation reversed in time
μ	Second Lamé parameter
ρ	Density
ρ_i	Peak model standard deviation for i^{th} material
σ	Stress tensor
ω_c	Central angular frequency of source signal

CONTENTS

1 INTRODUCTION

1.1 Inverse problems

Inverse problems are a rich topic of research in Applied Mathematics, Physics, Engineering, and constitute the fundamental framework for many applicatons in medical imaging (LOUIS, 1992), non-destructive testing (ZAOUI et al., 2010), hydrocarbon exploration (MARCHETTI et al., 2014), geophyisical monitoring (MUNK; WORCESTER, 1988), besides many others (see Figure 1.1). However ubiquitous, inverse problems do not have a universal definition, and, as indicated by the name, presuppose the existence of a direct problem. According to the applied mathematician J. B. Keller, two problems are inverse to one another when the definition of one involves the solution of the other. He states that the older, more extensively studied problem is deemed as the direct one, while the inverse one is usually newer and not as well understood (KELLER, 1976).

Several of these are formulated as optimization problems constrained by partial differential equations. Consider a model represented by the equation:

$$L(u, m) = f \qquad \text{in} \ \ \Omega \times (0, T], \tag{1.1}$$

where L is a partial differential equation describing a transient process defined in the region Ω. L is parameterized by $m(\mathbf{x})$ and subject to the inhomogeneous term $f(\mathbf{x}, t)$. Given initial and boundary conditions, the quantity $u(\mathbf{x}, t)$ will evolve in a unique and determined way. Calculating it corresponds to solving the *direct problem*, since given a certain cause (the inhomogeneous term $f(\mathbf{x}, t)$, the boundary and the initial conditions) we are interested in determining the unique effect, in this case, the behaviour of $u(\mathbf{x}, t)$.

There are two types of inverse problem commonly associated to such a system (GROETSCH; GROETSCH, 1993). First, one could be interested in causation, which means, given the systems law of evolution, determining $f(\mathbf{x}, t)$, or initial conditions $u(\mathbf{x}, 0)$ from the current state. Second, one could be interested in the problem of identification, meaning estimating the parameters $m(\mathbf{x})$ from given input and output information. This relationship is summarized in Figure 1.2.

One common occurrence for inverse problems is that they are ill-posed (KIRSCH et al., 2011), i.e., they do not satisfy the Hadamard conditions for the mathematical representation of a physical system:

1. The solution exists.
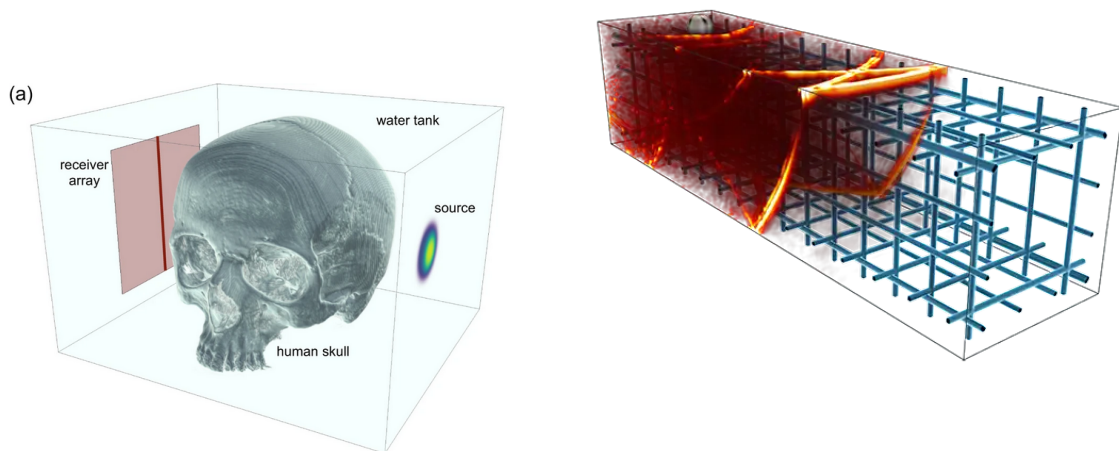
(a) Brain Imaging by acoustic inversion (GUASCH et al., 2020).

(b) Non destructive testing of reinforced concrete (AFANASIEV et al., 2019).
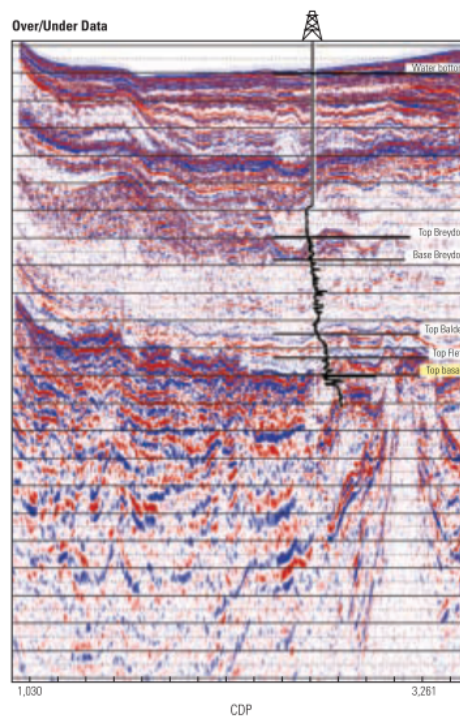
(c) Seismic imaging for reservoir characterization (BARCLAY et al., 2008).

Figure 1.1 − Inverse problem applications.

2. The solution is unique.

3. The solution depends continuously on the data.

The approach to the problem of ill-posedness varies according to application area. For instance, in the field of optimal design, which can be seen as a type of inverse problem, the non-existence issue was addressed by enlarging the solution space (KOHN; STRANG,

1986). This particular type of relaxation by the introduction of homogenization paved the way for the later appearance of Topology Optimization (BENDSØE; KIKUCHI, 1988). Non-uniqueness is typically related to a lack of information, which, if available, should be incorporated into the model. The third issue is the most critical when solving an inverse problem by numerical methods. If small variations in the data can lead to arbitrarily large variations in the solution, the process will not be stable, noise and small numerical errors will compound and one cannot rely on the solutions obtained.

The lack of stability can be dealt with by introducing regularization methods, which approximate the ill-posed problem by neighbouring well-posed ones, or by the addition of *a-priori* information about the solution (ENGL; HANKE; NEUBAUER, 1996).

1.2 Subsurface salt imaging

Studying the Earth's subsurface is an important task in several disciplines. In geotechnical and underground planning, knowledge of burried objects is important in order to mitigate and control project risks (NGUYEN; NESTOROVIĆ, 2018). In an environmental context, understanding the subsurface is needed for evaluating the feasibility of sustainability initiatives such as carbon sequestration and storage. In Geoscience, imaging the Earth's interior is fundamental in order to comprehend the nature of hotspots, plate movements and earthquake activity. In the energy sector, subsurface imaging is the main taks of geophyisical exploration, targeted at locating mainly hydrocarbon reservoirs (SHERIFF; GELDART, 1995).

Among several types of formations, the presence of salt structures is particularly relevant in subsurface imaging applications. These formations appear when thick layers of evaporite salts are covered by sediments, and over geological timescales deform and migrate due to their lower density compared to the sediments, resulting in a variety of structures (HUDEC; JACKSON, 2007). One such structure is the salt dome, where salt pushes upwards to form a dome-like shape. Salt domes are prevalent in exploration sites such as the Gulf of Mexico (GoM). In other places, such as the coast of Brazil, extensive layers of salt remain relatively flat, creating large horizontal salt beds (or layers). These
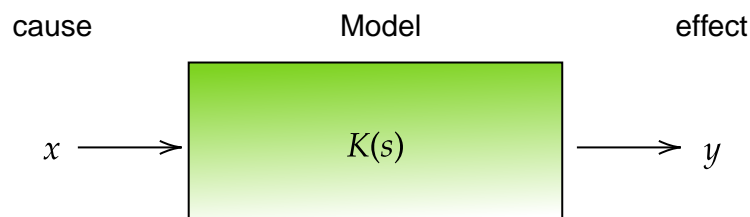
Figure 1.2 − Representation of a system $y = K(s)x$, which could be associated to the inverse problems of retrieving either x (causation) or s (parameter identification).

salt layers are made primarily of halite(NaCl), although other evaporites such as gypsum ($CaSO_4$ - 2 H_2O) and anhydrite ($CaSO_4$) may also appear.

The presence of these salt structures has significant implications for hydrocarbon reservoirs. The impermeability of salt tends to form seals that trap hydrocarbons within or adjacent to it. Furthermore, the deformation of salt layers can generate structural traps where hydrocarbons may accumulate (HUDEC; JACKSON, 2007). For instance, in the case of the pre-salt layer off the Brazilian coast, the salt overlies potentially rich hydrocarbon reservoirs in the underlying carbonate rocks.

Subsurface imaging involves the estimation of the Earth's medium properties based on mechanical or electromagnetic measurements, a process that constitutes an inverse problem. A specific method employed in this context is seismic imaging, which utilizes active seismic sources to generate waves. These waves are subsequently recorded at strategically chosen locations, as schematically represented in Figure 1.3. The ultimate goal of this process is to reconstruct the properties of the subsurface in such a manner that a simulated signal aligns as closely as possible with the recorded one. The specific type of seismic inversion performed is determined by the equations governing wave propagation and the nature of the data collected.

Travel-time tomography, for instance, evaluates line-integrals along seismic raypaths in order to determine acoustic parameters of the subsurface. Such an approach relies on a high frequency approximation of the wave equation, and as a result, assumes that physical parameters vary slowly over sevel wavelengths. In addition, resulting images have a low resolution and are insensitive to velocity inversions (GUASCH, 2012). In order to obtain velocity fields with higher detail, techniques that model the whole wavefield are needed, instead of methods that employ approximations of the wave equation.

1.3 Full Waveform Inversion

Full Waveform Inversion (FWI) is a technique for identifying parameters in systems that model wave propagation. Despite having several applications such as medical imaging (AGUDO et al., 2018), (GUASCH et al., 2020), non-destructive testing (SEIDL; RANK, 2016) and CO_2 characterization (ROMDHANE; QUERENDEZ, 2014), FWI was first proposed in the context of seismic inversion by Santosa et al. (1984), Lailly e Bednar (1983), Tarantola (1984). FWI marked an advancement over previous methods such as Traveltime Tomography by incorporating phase information alongside wave transit time.

Using the full wave equation as state equation introduces non-linearity into the inversion problem, resulting in a computationally challenging task. As seismic imaging application, FWI can be broken down into the steps described in Section 1.2:

- The shot records are collected during a seismic survey(Figure 1.3)

- An initial guess, often obtained from another technique such as Traveltime Tomography, is defined.

- Initial guess and survey description are used to create a numerical wave propagation model, usually discretized by methods such as Finite Element Method (FEM) (ROBERTS et al., 2022), Spectral Element Method (SEM) (TRINH et al., 2017) or Finite Difference Method (FDM) (CHARARA; BARNES; TARANTOLA, 2005).

- The model parameters are updated within a Partial Differential Equation (PDE) constrained optimization framework.

The first implementation of FWI occurred in the latter half of the 1980s. It took one hour to perform five iterations of a problem with 40000 Degrees of Freedom (DoF) on a CRAY 1S supercomputer (GAUTHIER; VIRIEUX; TARANTOLA, 1986). The computational cost of FWI hindered its application, with the forward problem representing the main computational burden. Originally proposed in the time domain, wave propagation with explicit time integration may result in strict upper bounds on time step size depending on parameters such as source frequency, propagation velocity and mesh/grid size (FICHTNER, 2010). Pratt (1999) reformulated the problem in the frequency domain and efficiently implemented it, which led to successful fault delineation in a crosshole experiment (PRATT; SHIPP, 1999). One of the main limitations with this approach is the increasingly large size of matrix operators needed when using direct solvers (GUASCH, 2012).

Models have grown in complexity in tandem with computational power. The works cited up to this point have employed the acoustic approximation (Section 2.1). However, the use of the elastic wave equation and the consideration of 3D problems have become more prevalent following pioneering works. Gélis, Virieux e Grandjean (2007) and Sears, Singh e Barton (2008) solved FWI for elastic parameters. Regarding 3D modeling Warner,
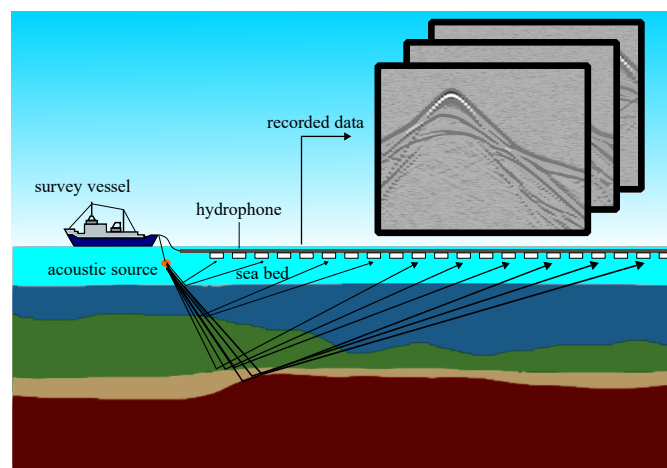
Figure 1.3 − A seismic survey, which collects phase and amplitude data necessary for FWI.

Stekl e Umpleby (2007), Sirgue et al. (2009) and Plessix et al. (2010) have used the acoustic approximation, while Epanomeritakis et al. (2008), Etienne et al. (2010) and Guasch et al. (2010) used elastic parameters.

Apart from the brodeaning of scope, FWI has several challenges inherent to a data fitting process with limited, noisy data. The lack of low frequency data has been addressed by Li e Demanet (2016), who proposes extrapolating low frequency data by separating events, by Hu et al. (2018), who reviewed existing methods for retrieving low frequency information, and by Sun e Demanet (2020), who trained a convolutional neural network to perform the extrapolation in the lower range frequency. Liu et al. (2016) proposed a modified L_2 misfit objective function in order to mitigate the effects of amplitude discrepancies between recorded and predicted data. In a sense, lack of low frequency data and amplitude mismatch are both related to the more general problem of cycle skipping, which is the convergence to local minima when the inversion initial guess is not close enough to the true model. In that regard, Alkhalifah (2014) suggested a gradient filter which mutes the low scattering angle contribution. Warner e Guasch (2016), on the other hand, put forward an objective function formulation that tries to match recorded and predicted data by the use of Wiener filters, mittigating cycle skipping severely according to the authors. Yao et al. (2019) proposed using "ìntermediary data" between observed and predicted values, such that nowhere the intermediary values exceeds half a wavelength from the predicted data. More recently, Li e Alkhalifah (2021) formulated an extended version of FWI that introduces parameters such as time lapses and scattering angles, while also adding a matching filter between observed and predicted data. The filter parameters are also included into the optimization search space.

1.3.1 Full Waveform Inversion in the presence of salt bodies

In hydrocarbon exploration, many sites are located in salt basins regions, such as the Gulf of Mexico and the Santos basin at east offshore of the brazilian coast. Indeed, most pre-salt resources there have yet to be produced, with the brazilian site expected to become one of the top 5 oil producers in the world (PETERSOHN, 2021).

FWI for subsurfaces with salt bodies is specially challenging due some of their characteristics, such as complex geometry and high impedance at the sediment-salt interfaces (see Figure 1.4 for synthetic velocity models that mimic this type of subsurface).

In particular, the misidentification of the salt body can lead to large timing errors in arrival time, and also to significant deviations in simulated wavepaths. The conventional workflow for dealing with salt bodies in velocity model building has been traditionally first applying FWI to identify the sediment layer above it. Next, flood migration would be employed for characterizing the top of salt, then the bottom. Finally, a number of salt
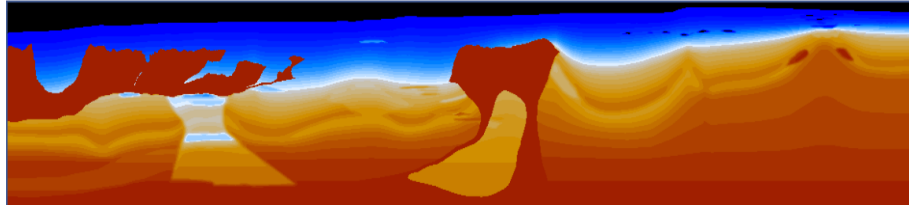
(a) BP 2004 velocity model. Salt structures are in red (BILLETTE; BRANDSBERG-DAHL, 2005).
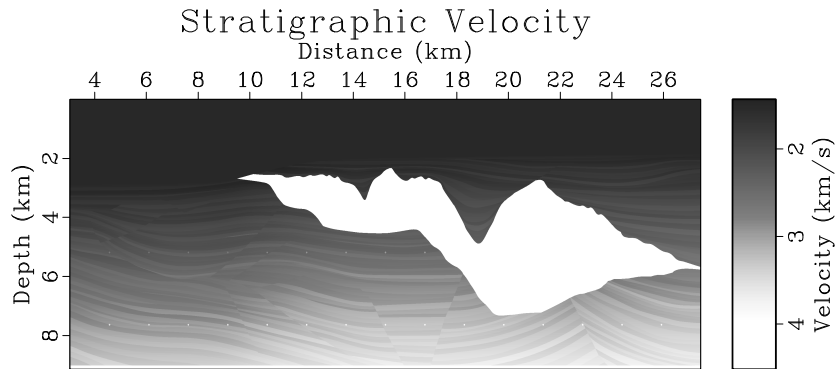
(b) Siegsbee2A velocity model. The salt body is the white structure (IRONS, 2001).

Figure 1.4 − Two synthetic velocity models with presence of salt structures.

scenarios would be tested in order to resolve the geometry (WANG et al., 2019).

Works have been published about salt velocity model building using synthetic velocity models (GUASCH; WARNER; HERRMANN, 2016; KADU; LEEUWEN; MULDER, 2016). Breakthroughs in field applications were obtained by Shen et al. (2018), who corrected misinterpretations for an exploration field in the Gulf of Mexico, and Zhang et al. (2018), who addressed issues of cycle-skipping and amplitude discrepancy using field data from areas with complex shallow salt bodies (again in the Gulf of Mexico).

Since salt bodies are problematic for conventional FWI, while also exhibiting characteristic features, the use of models that incorporate this *a-priori* information has been employed by several authors with the use of a Level Set (LS) parametrization (GUO; HOOP, 2012; GUO; HOOP, 2013; KADU; LEEUWEN; MULDER, 2016; DORN; WU, 2021; ALBUQUERQUE; LAURAIN; YOUSEPT, 2021a). Another way of enforcing "blockiness" is to use an appropriate regularization scheme such as Total Variation (TV) (ANAGAW; SACCHI, 2011), or its variations designed specifically for seismic, for instance, the Modified Total Variation (MTV) from Lin e Huang (2014) or the assymetric TV from Esser et al. (2016). Lately, higher order regularizations that deal better with complex, noisy data than TV have been also proposed (GAO; HUANG, 2019).
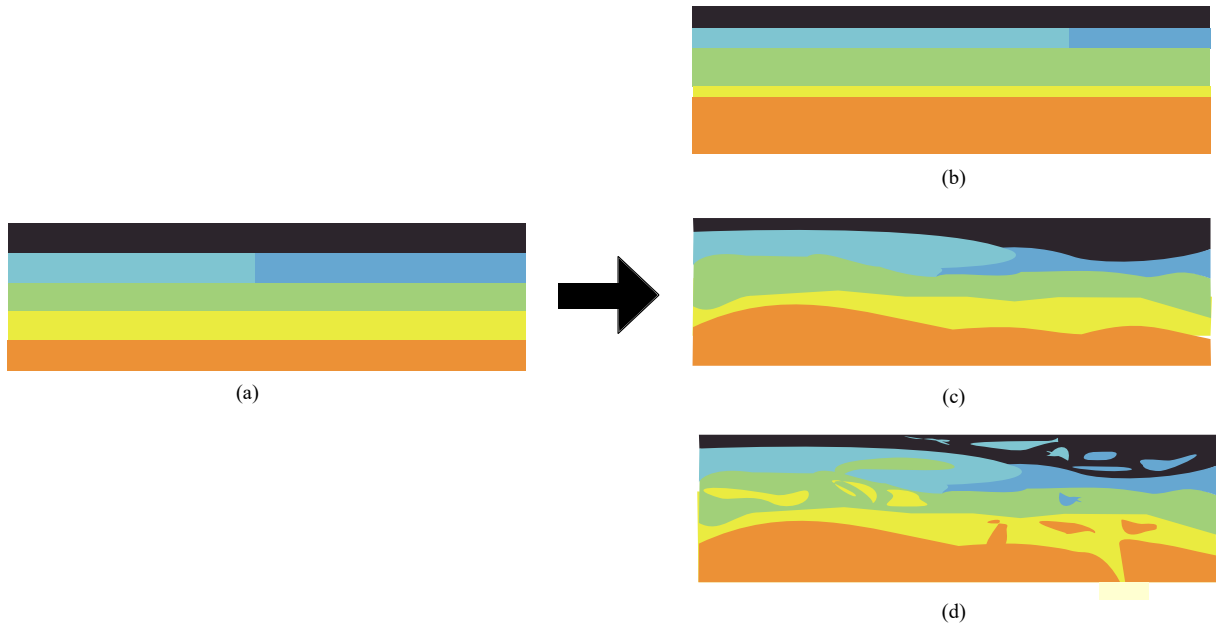
Figure 1.5 – Types of optimization given the same (a) initial domain: (b) Size, (c) shape, and (d) topology optimization.

1.4 Topology optimization

The objective of Topology Optimization (TO) is to determine the optimal material distribution on a certain domain. Although this problem is centuries old (M.C.E, 1904), it was only after the formulation given by Bendsøe and Kikuchi (BENDSØE; KIKUCHI, 1988) that the discipline of TO experienced substantial growth, both in volume of research and scope. Originally applied to structures subject to mechanical loads, TO was generalized in order to solve multiphysics problems considering diverse phenomena such as heat transfer, aeroelasticity, electromagnetic fields, and many others (DEATON; GRANDHI, 2014). The TO designation distinguishes it from other design techniques that only alter characteristic dimensions (parametric optimization) or the boundary definition (shape optimization), but do not allow the nucleation or closure of holes, see Figure 1.5.

In a single material framework, the design domain Ω is discretized into a set of elements or nodes, each one associated to a design variable ρ_i. The region Ω_D where $\rho = 1$ defines the presence of material, while $\Omega \backslash \Omega_D$ where $\rho = 0$ defines its absence. The design process then consists in extremizing some measure such as stiffness, first natural frequency or dissipated power, for instance. In practice, a naïve TO implementation as described above suffers from severe numerical instabilities and requires the use of relaxation schemes and regularizations (SIGMUND; PETERSSON, 1998). In addition, the methodology is not restricted to single material design, and several multimaterial approaches have been proposed (BENDSØE; SIGMUND, 1999; YIN; ANANTHASURESH, 2001; ZUO; SAITOU, 2017).

Besides structural design, TO has already been applied to several inverse problems. The design of metamaterials, for instance, is a type of inverse problem where, instead of evaluating the material properties from the microstructure, a given microstructure

is obtained by minimizing a misfit between predicted and given material properties. In this field, Larsen, Sigmund e Bouwsta (1997) designed and manufactured compliant micromechanisms with negative Poisson's ratio, while Sigmund e Torquato (1996) investigated composites with extremal thermal expansion coefficients. Byun et al. (2000) applied TO to the permittivity identification problem using the concept of mutual energy in sensitivity evaluation. Lima et al. (2007) developed a TO formulation for Electrical Impedance Tomography (EIT) and used experiments to assess its effectiveness. Mello et al. (2008) expanded the TO EIT approach to 3D and also performed tests with experimental data. (RYUZONO et al., 2019) employed TO in the problem of Non-Destructive Testing (NDT), combined with visualization of ultrasonic wave propagation. TO has also been applied in the context of acoustic parameter identification under different formulations. Lanznaster et al. (2021) employed a LS based representation of inclusions, Goncalves et al. (2020), Goncalves e Silva (2021) used continuous variables, and Moreira et al. (2023) applied a discrete control variable approach. In particular, Gonçalves e Silva (2023) considered the reconstruction problem in the context of FWI.

TO is pertinent to FWI problems characterized by sharp interfaces, such as salt bodies or layers. In these cases, the combination of limited sub-salt penetration and significant wavepath deviation renders the positioning and estimation of regions beneath these geological formations challenging with conventional methods. Alternative approaches like level set methods and TV regularization possess inherent limitations. Current implementations of level set FWI (KADU; LEEUWEN; MULDER, 2016; DORN; WU, 2021; ALBUQUERQUE; LAURAIN; YOUSEPT, 2021b) are constrained by the topology of initial estimates. On the other hand, TV regularization produces unwanted inversion artefacts (LIN; HUANG, 2014). Given these considerations, there is a demand for an inherently discrete TO approach that offers greater flexibility for topology changes and also effectively mitigates the generation of spurious artifacts through proper filtering techniques (SIGMUND; PETERSSON, 1998; GUEST; PRÉVOST; BELYTSCHKO, 2004).

1.4.1   Material models

TO is intrinsically discrete, given that a certain material (or void) is assigned to each point of the domain. As an ill-posed optimal design problem (KOHN; STRANG, 1986), its first iterations (BENDSØE; KIKUCHI, 1988) regularized the original problem by employing anisotropic materials with composite microstructures, and evaluated effective material parameters by applying homogenization techniques. This formulation however introduces considerable complexity, whilst adding subjectivity if it's desired to interpret the resulting composite material distribution as a discrete design.

Bendsøe (1989), Zhou e Rozvany (1991) suggested an alternative approach, now known as Solid Isotropic Material with Penalization (SIMP), where materials properties are

interpolated as powers of the control variable. If we are optimizating for a certain property ϕ as a function of the control variable $0 \leq a \leq 1$, a possible SIMP interpolation could be:

$$\phi = a^P \bar{\phi}, \tag{1.2}$$

where P is the so called penalization exponent, which is expected to force ϕ either to 0 or to the maximum value $\bar{\phi}$. This approach is mesh dependent, although filtering functions acting over either the sensitivity or the control variable can limit this problem by enforcing a minimum design characteristic length (SIGMUND; MAUTE, 2013).

In general, material models act by modyfing the solution space, either enlarging or restricting it, and as such can be convenient for "steering" solutions of optimization problems to a certain behaviour, instead of directly introducing extra constraints in the optimization problem.

1.4.2 Discrete control variables

In topology optimization, perhaps the most common approach is to use so called density methods (SIGMUND; MAUTE, 2013), which employ a continuous pseudo density to assign either the presence of material or a void to a certain region. Albeit appropriate for many applications, density methods face difficulties in some types of problems. For instance, continuous variables are innapropriate for accurately representing material interfaces given the propensity to generate "transition regions" where intermediate control values map neither to a certain material nor to its absence.

These and other particular challenges motivated the development of methodologies that keep clear discrete designs. Level Set and and Bi-directional Evolutionary Structural Optimization (BESO) can be highlighted as popular approaches within this framework (DEATON; GRANDHI, 2014). While level set methods utilize a continuous field in order to implicitly define a discrete characteristic function, BESO uses a discrete control variable to assign well defined materials (or void) to each point in the domain throughout the whole optimization process (HUANG; XIE, 2009). Its main drawback is in the heuristics update criteria, which makes generalization difficult for problems with constraints that deviate from the classical volume constraint.

Sivapuram, Picelli e Xie (2018a) developed a new methodology for dealing with discrete designs. Its formulation is straightforward as in the BESO method, however, the update process employs mathematical programming, making it more general and capable of handling any type and number of constraints (SIVAPURAM; PICELLI; XIE, 2018b). To the best of the authors knowledge, Topology Optimization of Binary Structures (TOBS) has only been implemented as a sequential integer linear programming problem (see 3.2.2). The Integer Linear Programming (ILP) problem solved at each iteration is

more computationaly complex than a Linear Programming (LP) solve, however, since the computational bottleneck of PDE-constrained optimization problems is to solve the forward problem and (possibly) calculating the gradient, this added cost is not significant to the whole optimization process, as shown in (SIVAPURAM; PICELLI, 2020).

1.5   Acoustic modelling

As closed form solutions for the wave equation are only available for fairly simple domain geometries and boundary configurations, the application of numerical methods are a necessity in waveform imaging. In order to solve the wave equation numerically, it is necessary to discretize it both in space and time.

Time discretization usually consists in approximating time derivatives by low order finite differences. More sophisticated variants such as multi-step predictor-corrector or high order Runge-Kutta methods are not common due to empirical studies showing that i) the improvement in accuracy does not offset the added computational cost, but mainly that ii) spatial discretization error is dominant over time discretization error (FICHTNER, 2010). Besides applying finite differences to time derivatives, an alternative is to formulate the wave equation in the frequency domain. If the bandwidth considered is relatively narrow, a large number of sources has to be considered, and an efficient solver is available, a frequency-domain implementation is to be favoured. This is the case since direct factorization for each frequency can be reutilized for any given source if memory resources allows it, or when this characteristic can be explored by iterative solvers. For wider bandwidths a larger number of frequencies has to be solved for, thus an explicit timestepping scheme may be more cost-efficient (VIRIEUX; CALANDRA; PLESSIX, 2011).

The most significant distinction between numerical methods, however, is in spatial discretization, that is, how are the spatial derivatives approximated, and what are the characteristics and properties of the the resulting algebraic system. In the context of waveform modelling, Virieux, Calandra e Plessix (2011) suggests grouping numerical methods in three classes: Spectral, strong or weak formulations.

Spectral Methods are formulated in the dual waveform space. There, analytical or semi-analytical solutions can be constructed by means of Cagniard-De Hoop path integrals (AKI; RICHARDS, 2002). It is customary to expand the solution using special functions, and to employ numerical integration techniques for relatively complex geometries. A considerable hindrance with this approach is the restriction to laterally invariant 3D media. Even though alternatives such as fast moment methods exist for laterally varying media (CHAILLAT; BONNET; SEMBLAT, 2008), Spectral methods are not a viable alternative for rapidly changing lateral variations or when there are abrupt property changes such

as is the case for velocity models with salt bodies (VIRIEUX; CALANDRA; PLESSIX, 2011).

Strong formulations consist of methods satisfied locally, either over grid points or finite volumes. The Finite Difference Method is likely to be still the most common method applied to waveform imaging (AFANASIEV et al., 2019). According to Fichtner (2010), the viablity of Finite Differences for 3D problems hinges in the use of staggered grids, which reduces numerical dispersion by decreasing average grid spacing, and its popularity resides in low computational cost for a given accuracy in the modeling of body waves. Nevertheless, FDM has several drawbacks such as difficulty in capturing complex material interfaces, imposing non trivial boundary conditions, as well as representing complex geometries (AFANASIEV et al., 2019). Indeed, Zhebel et al. (2014) shows that, for a given accuracy, while for homogeneous material properties FDM is one order of magnitude faster than FEM, for a complex material distribution with strong topography, FEM is two order of magnitudes more efficient. In that front, the generalization of rectangular grids by means of curvilinear coordinate transforms (SHRAGGE, 2016) improve the modeling of complex geometries. Nevertheless, they still impose the use of continuous smooth surfaces(or curves), and only complicate further the implementation of boundary conditions. In the Finite Volume Method, the domain is partitioned into non-overlaping volumes, and an integral form of the wave equation is solved for each finite volume. The Finite Volume Method (FVM) introduces meshes, which consideraly improves the modelling of complex geometries and material interfaces. According to Afanasiev et al. (2019), although there are promising results with high order approximations, they are not as cost effective as discontinuous finite elements. Optimal operators are a method in which operators are specifically designed to minimize the discretization error near the eigenfrequencies of the model (FICHTNER, 2010). This is done by minimizing the inner product between the modes of the solution and the PDE residual (TAKEUCHI; GELLER, 2000).

Weak formulations are variational statements equivalent to the original PDE. Restricting our focus to Finite Element Galerkin Methods, the domain is partitioned into non-overlapping sub-domains, while test and trial functions are approximated using the same finite dimensional function space. Although more precise at characterizing irregular topographies and material interfaces, low order formulations have comparatively higher numerical dispersion when compared to other methods, and the use of explicit methods is difficultated by the fact that non-diagonal mass matrices demand the solution of a whole linear system at each time step, instead of matrix vector multiplications (AFANASIEV et al., 2019). The Spectral Finite Element Method (KOMATITSCH; VILOTTE, 1998) utilizes high order polynomials as basis functions and Gauss-Lobato-Legendre (GLL) techniques in order to obtain diagonal mass matrices and spectral converge in space (VIRIEUX; CALANDRA; PLESSIX, 2011). Discontinuous Galerkin methods are an approach to Finite Elements

which does not impose continuity between elements. While discontinuous elements can better capture discontinuous interfaces, they introduce fluxes between elements, which increases computational cost (FICHTNER, 2010), in addition to a more restrictive stability condition (AFANASIEV et al., 2019).

1.6 Motivation

Some inverse problems deal with imaging inherently discontinuous fields. For instance, NDT for crack detenction (SEIDL; RANK, 2016) and P-wave velocity reconstruction in the presence of salt bodies (WANG et al., 2019) seek to identify high constrast material interfaces. For these types of problems it seems fit to apply integer variable TO, which better represents the distribution of acoustic properties. Furthermore, using a TO framework also allows bringing methods from that field for dealing with ill-posedness while at the same time respecting the interface contrast throughout the imaging process.

In addition, sharp interfaces models are being researched as a viable tool for velocity model building in seismic in the presence of salt bodies. Integer Linear Programming applied to material distribution in problems with sharp interfaces has a growing field of applications (SIVAPURAM; PICELLI; XIE, 2018a; PICELLI et al., 2020; SIVAPURAM; PICELLI, 2020), including wave propagation (MOREIRA et al., 2023).

1.7 Objectives

The main objective of this work are the development and implementation of a seismologically relevant procedure for inverse problems subject to wave propagation, with the imposition of *a-priori* information about the presence of sharp interfaces by the use of Integer Programming. The implementation was carried using the open source wave-propagation simulation tool Spyro (ROBERTS et al., 2022), built on top of Firedrake (RATHGEBER et al., 2016a). The optimizer IBM-ILOG CPLEX was used to solve the Integer Linear Programming (ILP) updating sub problems (MANUAL, 1987). The goals of this work can be subdivided into:

- Implementation of an inversion procedure for discrete velocity models with a single type of inclusion.

- Verification of implementation by comparison with cases from the Literature.

- Implementation of a multimaterial inversion procedure for discrete velocity models, allowing for more than one type of inclusion.

- Application of multimaterial model to subsalt reconstruction case.

1.8   Scientific Contributions

The expected scientific contributions are the following:

- Assessment of Integer Programming to velocity model building in the presence of sharp interfaces.

- Extention of Integer Linear Programming to material distribution problems subject to wave propagation.

Four works have been produced:

- Presentation about Acoustic Tomography by Topology Optimization given on the 14th World Congress on Computational Mechanics (WCCM).

- Published paper on Acoustic Inversion by Topology Optimization in the frequency domain (GONCALVES et al., 2020).

- Published paper on Acoustic Inversion by Topology Optimization in the time domain (MOREIRA et al., 2023).

- Submitted paper on Acoustic Wave Propagation Modeling (SOUZA et al., 2022).

2 WAVE MODELING

This chapter introduces the wave equation formulation chosen for performing seismic inversion. The acoustic approximation of a linear elastic medium is discussed, as well as the choice of Absorbing Boundary Layers (ABL) and Absorbing Boundary Conditions (ABC) for modeling semi-infinite mediums. The time signature chosen to model a point source is displayed, and since this work uses the Finite Element Method (FEM), the variational formulation of the wave equation is presented.

2.1 P-wave propagation in elastic media

The governing equations of motion for a linear elastic isotropic medium Ω during an interval $(0, T)$ are given as:

$$\rho \partial_{tt} \mathbf{u} - \nabla \cdot \sigma = \rho \mathbf{b} \qquad \text{in} \quad \Omega \times (0, T], \tag{2.1a}$$

$$\sigma = \lambda \mathrm{Tr}(\varepsilon) \mathbf{I} + 2\mu \varepsilon, \tag{2.1b}$$

$$\varepsilon = \frac{1}{2} \left[\nabla \mathbf{u} + (\nabla \mathbf{u})^T \right], \tag{2.1c}$$

where the displacement $\mathbf{u}$, the stress σ and the strain ε may all depend on space and time. The Lamé parameters λ and μ, however, may vary only in space since expression (2.1b) hinges on the assumption of no viscoelastic effects (SPENCER, 2004). In order to arrive at the scalar wave equation we will further assume a homogeneous medium, with λ and μ being constants, and also that relative variations of the density ρ are negligible. $\mathbf{b}$ is the body force per unit mass.

A homogeneous isotropic medium supports two deformation modes, one associated with changes in volume without changes in shape (P waves), and another where changes in shape manifest without changes in volume (S waves) (CARCIONE, 2007). In geophysics exploration, computational costs associated with solving (2.1) leads practitioners to adopt the acoustic approximation, which albeit not as realistic as the full linear elasticity equations still models wave propagation to a degree deemed acceptable for applications that restrict data analysis to first-arriving P waves and model sources with explosive radiation patterns (FICHTNER, 2010).

Different paths can be taken to arrive at the acoustic approximation:

(i) Simply ignoring the constitutive parameter associated to shear μ (FICHTNER, 2010).

(ii) Describing **u** in terms of Lamé potentials, separating P and S waves into two uncoupled equations (ATKIN; FOX, 2005).

(iii) Applying the divergence operator to (2.1a), thus discarding information about shear strain.

In this work, route (iii) is taken. First, equations (2.1) are combined into a single expression in terms of the displacements:

$$\rho \partial_{tt} \mathbf{u} - \nabla \cdot \left\{ \lambda \ (\nabla \cdot \mathbf{u}) \, \mathrm{I} + \mu \, \left[\nabla \mathbf{u} + (\nabla \mathbf{u})^T \right] \right\} = \rho \mathbf{b}. \tag{2.2}$$

Expanding the expression under the divergent operator and applying the vectorial identity $\nabla \times \nabla \mathbf{u} = \nabla(\nabla \cdot \mathbf{u}) - \Delta \mathbf{u}$ leads to:

$$\rho \partial_{tt} \mathbf{u} - (\lambda + 2\mu) \, \Delta \mathbf{u} - (\mu + \lambda) \, \nabla \times \nabla \times \mathbf{u} = \rho \mathbf{b}. \tag{2.3}$$

The application of the divergent, use of the identity $\nabla \cdot (\nabla \times \bullet) = 0$ and division by ρ results in a variable density wave equation:

$$\frac{\nabla \rho}{\rho} \cdot \partial_{tt} \mathbf{u} + \partial_{tt} p - \frac{(\lambda + 2\mu)}{\rho} \Delta p = \frac{\nabla \rho}{\rho} \cdot \mathbf{b} + \nabla \cdot \mathbf{b}, \tag{2.4}$$

in terms of the volume strain $p = \nabla \cdot \mathbf{u}$ (for linear elasticity).

If it is assumed that the magnitude of the relative density variation $|\nabla \rho|/\rho$ is negligible with respect to second order variations of p in both space and time, then one can simplify further (ATKIN; FOX, 2005), arriving at the acoustic wave equation:

$$\partial_{tt} p - v_p^2 \Delta p = s, \tag{2.5}$$

where $v_p = \sqrt{(\lambda + 2\mu)/\rho}$ is the speed with which the wavefront travels and $s = \nabla \cdot \mathbf{b}$ is a volumetric source term.

It is worth nothing that, while leading to the same equation, route (i) would imply in a wave speed $v_p = \sqrt{(\lambda + \frac{2}{3}\mu)/\rho} = \sqrt{\kappa/\rho}$, which does not coincide with our derivation. An acoustic velocity given in terms of the bulk modulus κ is consistent with a derivation from the Euler equations for fluid media (COHEN, 2001). In that case p would not be the volume strain, it would be a mean stress value proportional to it, such that $p = -\kappa \nabla \cdot \mathbf{u}$. In any case, if we are to apply velocity model building with only v_p as design variable this distinction does not lead to divergent results.

2.2 Boundary conditions and source term

2.2.1 Boundary conditions

In applications where a finite solid body Ω is considered, such as non-destructive testing or medical imaging, the boundary $\partial\Omega$ is modeled as a rigid surface (COHEN, 2001). Mathematically, this means p is subject to Neumman boundary conditions:

$$\mathbf{n} \cdot \nabla p = 0 \qquad \text{on} \quad \partial\Omega \times (0, T], \tag{2.6}$$

where $\mathbf{n}$ is the unit vector normal to $\partial\Omega$.

For seismic applications on the other hand, the domain possibly has to be modeled as a semi-infite medium. Let $\partial\Omega = \Gamma_D \cup \Gamma_A$ be the boundary of the computational domain Ω, where the non-intersecting Γ_D and Γ_A are illustrated in Figure 2.1.

Figure 2.1 − Semi infinite domain typical of geophysics exploration.
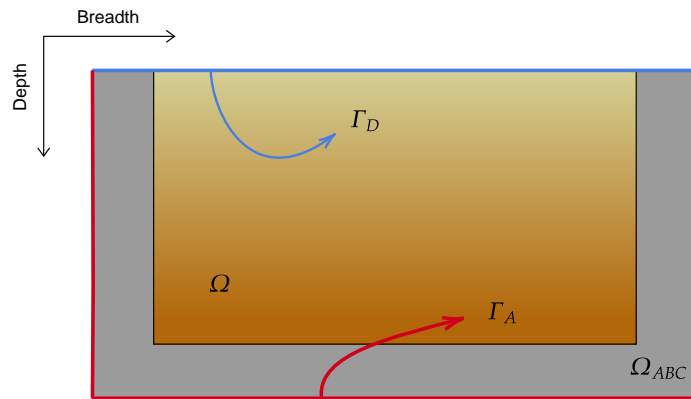
The boundary Γ_D is a contact surface between air and ground, or air and water. In any of these cases, the most appropriate conditions are homogeneous Dirichlet boundary conditions (COHEN, 2001):

$$p = 0 \qquad \text{on} \quad \partial\Omega \times (0, T]. \tag{2.7}$$

Unbounded domains in finite computational grids (or meshes) can be approximated to varying levels of efficiency. One can introduce a damping layer Ω_{ABC} around the original boundary such that the computational domain is augmented as $\Omega_{ext} = \Omega \cup \Omega_{ABC}$. In the extended region, a dissipative term is added to the wave equation in order to dampen reflective waves (CERJAN et al., 1985). Another approach is to use Absorbing Boundary Conditions (ABC). They impose a transparency condition (ENGQUIST; MAJDA, 1977), a global constraint which can be enforced locally to different orders of approximation. At last, there are Perfectly Matched Layers (PML), damping layers constructed in such a way
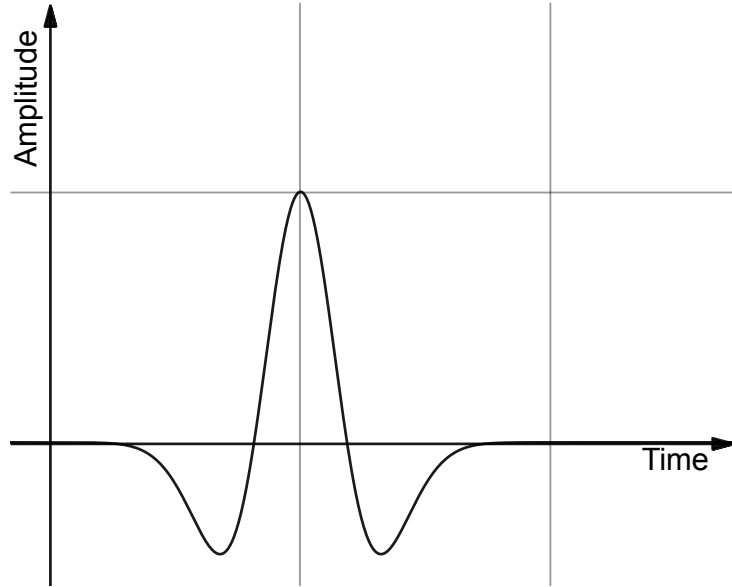
Figure 2.2 − Source signal corresponding to a Ricker Wavelet.

that no reflection occurs (BERENGER, 1994; GROTE; SIM, 2010), and Convolutional Perfectly Matched Layers (CPML) (KUZUOGLU; MITTRA, 1996), which solve some numerical problems introduced by the original PML formulation (COHEN; PERNET, 2017). In this work, a 0th order transparency condition (ENGQUIST; MAJDA, 1977) is used:

$$\frac{1}{v_p}\frac{\partial p}{\partial t} + \mathbf{n} \cdot \nabla p = 0 \qquad \text{on } \Gamma_A \times (0, T]. \tag{2.8}$$

In a few examples where comparisons to the literature are made, ABCs are used for consistency sake. In that case, the wave equation from 2.5 becomes:

$$\partial_{tt}p + \eta\partial_t p - v_p^2 \Delta p = s, \tag{2.9}$$

where η is an artificial damping coefficient which is different from zero only in Ω_{ABC} and has the sole purpose of dissipating reflected waves.

2.2.2 Source term

The Ricker wavelet is applicable to the simulation of mechanical wave propagation through homogeneous viscoelastic media emanating from a point source (WANG, 2015). In particular, it is applicable to wave simulation in elastic media. Since this work considers only the reconstruction of synthetic velocity models, the point source time signal is chosen to be a Ricker wavelet. Considering a source at $\mathbf{x_s} \in \Omega$, we may expand the right hand side of (2.5) as:

$$s(\mathbf{x}, t) = \left(1 - \frac{1}{2}\omega_c^2(t - t_0)^2\right) \exp^{-\frac{1}{4}\omega_c^2(t-t_0)^2} \delta_{\mathbf{x_s}}, \tag{2.10}$$

where ω_c is the central angular frequency of the excitation signal, t_0 is some delay time and $\delta_{\mathbf{x_s}}$ is a Dirac's delta distribution centered on $\mathbf{x}_s$. Figure 2.2 displays the time dependence

of the wavelet applied at some point $\mathbf{x_s}$. In real seismic imaging applications, it may be necessary to estimate the source time signal (VIRIEUX et al., 2017).

2.3 Variational formulation

In order to apply the Finite Element Method, the wave equation (2.5) is recast into an equivalent integral formulation (HUGHES, 2012). We search for a solution p belonging to $V \subset H^1(\Omega)$ such that, for any q in $\hat{V} \subset H_0^1(\Omega)$, we have:

$$\int_\Omega \partial_{tt}p\,q\,d\Omega + \int_\Omega \eta\partial_t p\,q\,d\Omega + \int_\Omega v_p^2\nabla p \cdot \nabla q\,d\Omega = \int_{\Gamma_A} gq\,d\Gamma + \int_\Omega sq\,d\Omega, \qquad (2.11)$$

obtained by multiplying the original PDE by a test function q and integrating by parts. V is the subset of $H^1(\Omega)$ of all functions satisfying appropriate essential boundary conditions for the problem at hand, while $\hat{V}$ is restricted to functions satisfying homogeneous essential boundary conditions, hence $H_0^1(\Omega)$ (HUGHES, 2012). The surface integral on the right hand side comes from the transparency condition in (2.8), with g corresponding to:

$$v_p^2\,\mathbf{n} \cdot \nabla p = -v_p\frac{\partial p}{\partial t} = g \qquad \text{on } \Gamma_A \times (0,T]. \qquad (2.12)$$

In order to simplify notation and ease manipulation of the variational problem, the following linear and bilinear forms are defined:

$$\begin{aligned}
(u,v) &:= \int_\Omega u\,v\,d\Omega, \\
(u,v)_\eta &:= \int_\Omega \eta\,u\,v\,d\Omega, \\
a(u,v) &:= \int_\Omega v_p^2\nabla u \cdot \nabla v\,d\Omega, \\
l(v) &:= \int_\Omega s\,v\,d\Omega + \int_{\Gamma_A} g\,v\,d\Gamma.
\end{aligned} \qquad (2.13)$$

If in addition we denote $\partial_t() = \dot{()}$, then (2.11) can be rewritten as:

$$(\ddot{p},q) + (\dot{p},q)_\eta + a(p,q) = l(q) \qquad \forall q \in \hat{V}. \qquad (2.14)$$

The convenient dismissal of $\dot{p}$ from the linear term $l(q)$ is allowed due to choosing a backward finite difference discretization for the boundary term as described in 4.1. In that case, at any given time s and g from 2.13 are known functions.

3 TOPOLOGY OPTIMIZATION APPLIED TO ACOUSTIC INVERSION

3.1 Acoustic Inverse Problem

Under adequate assumptions the scalar wave equation may describe propagation of mechanical waves in fluids or solids, being employed in the modeling of distinct phenomena such as vibrations, sound generation, seismic activity, ultrasound, among others.

The problem of identification, which relies on minimizing the discrepancy between simulated and experimental data, can exhibit considerable variations among applications. These variations may include aspects such as the boundedness of the domain, constraints on observability arising from the quantity and placement of sensors, and resolution dependent on characteristic dimensions, wave velocities, and frequencies employed. Nevertheless, the acoustic parameter identification problem may be written somewhat generally (SEIDL; RANK, 2017; VIRIEUX et al., 2017) as stated in (3.1) and ilustrated in Fig 3.1.

Let v_p be the parameter field and s be a point source at $\mathbf{x}_s$ from which excitations propagate throughout the domain Ω. During a time span of T, the amplitudes $p_{0,s}$ at $\mathbf{x}_r$ are recorded as the experimental values $d_{s,r}(t) = p_{0,s}(\mathbf{x}_r, t)$. The boundary $\partial\Omega = \Gamma_D \cap \Gamma_N \cap \Gamma_A$ may be split in sections which obey Dirichlet, Neumann or Robin type Absorbing boundary conditions as hinted by the subindices. The domain may be extended such that $\Omega_{ext} = \Omega \cup \Omega_{ABC}$. For a system subject to (2.5), one seeks v_p that minimizes the difference between $d_{s,r}(t)$ and $p_s(\mathbf{x}_r, t)$ for every source s at every receiver r.

In general, for the inversion procedure up to N_s sources and N_r receivers are employed instead of a single pair. The parameter identification problem can then be formulated as an optimization problem:

$$
\begin{aligned}
\underset{v_p}{\text{minimize}} \quad & f = \sum_s^{N_s} \sum_r^{N_r} \int_0^T \int_\Omega \left(p_s(\mathbf{x}, t)\delta_{\mathbf{x_r}} - d_{s,r}(t)\right)^2 \, d\Omega dt \\
\text{subject to} \quad & \partial_{tt}p_s + \eta\partial_t p_s - v_p^2 \Delta p_s = s(\mathbf{x}_s, t), \quad s = 1, \ldots, N_s \\
& p_s(\mathbf{x}, t) = 0 \quad \text{on} \quad \Gamma_D \\
& \partial_n p_s(\mathbf{x}, t) = 0 \quad \text{on} \quad \Gamma_N \\
& \frac{1}{v_p}\frac{\partial p}{\partial t} + \mathbf{n} \cdot \nabla p = 0 \quad \text{on} \quad \Gamma_A \\
& p_s(\mathbf{x}, 0) = 0 \quad \text{in} \quad \Omega_{ext} \\
& \partial_t p_s(\mathbf{x}, 0) = 0 \quad \text{in} \quad \Omega_{ext}
\end{aligned}
\tag{3.1}
$$
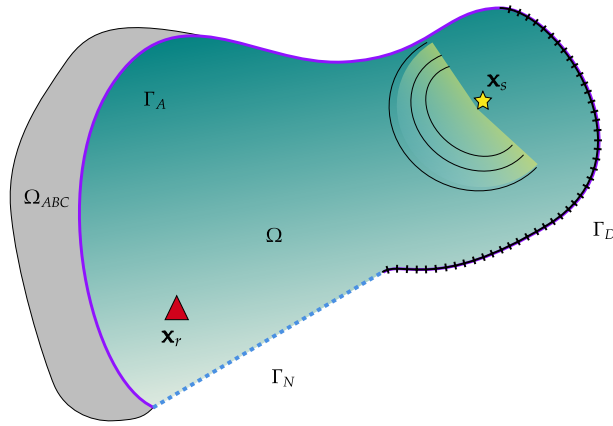
Figure 3.1 − Acoustic system for a single source-receiver pair.

3.2 Topology Optimization Problem Formulation

A generic TO problem may be stated as follows: a certain variable of interest must be extremized, and an equation of state describing a certain physical process has to be satisfied. A minimization problem, for instance, becomes:

$$
\begin{array}{lll}
\underset{\boldsymbol{\rho}}{\text{minimize}} & f(\boldsymbol{\rho}, \mathbf{S}) & \text{Objective Function} \\
\text{subject to} & \mathbf{R}(\boldsymbol{\rho}, \mathbf{S}) = \mathbf{0} \text{ in } \Omega & \text{State Equation} \\
& 0 \leq \boldsymbol{\rho} \leq 1 \text{ in } \Omega & \text{Box Constraints}
\end{array}
\tag{3.2}
$$

Here $\boldsymbol{\rho}$ describes the material distribution in the domain Ω, and each component of $\boldsymbol{\rho}$ is restricted to values between 0 and 1. We want to minimize the value of f while simultaneously keeping the residuals $\mathbf{R}$ of the state equations zero. The vector $\mathbf{S}$ designates the state variables of interest.

A category of TO problems known as density methods (SIGMUND; MAUTE, 2013) introduces the concept of a material model, where a pseudo-density that penalizes intermediary values for $\boldsymbol{\rho}$ is used. The material model concept can be explored by the choice of the interpolating function that connects the design variable $\boldsymbol{\rho}$ to the material parameter being interpolated, be it mass density, porosity or constitutive parameters such as Young's modulus and Poisson's ratio.

Material interpolation schemes affect the feasible space to which $\boldsymbol{\rho}$ belongs in different ways. The RAMP approach (STOLPE; SVANBERG, 2001) manipulates the convexity of the objective function so as to increase the probability of binary solutions. The interpolating material model introduced in (YIN; ANANTHASURESH, 2001) uses weighted Gaussian

distributions so as to coalesce the design around chosen mean values. This configuration allows for multimaterial modeling, since each Gaussian can be selected to correspond to a certain material.

In this work three material models are used, one that allows for a binary description of the model, and two other that allow multimaterial modelling. Multimaterial models describe material parameters as piecewise constant fields with possibly more than two different values.

3.2.1 Material models

The SIMP material model (BENDSØE, 1989) is used to approximately represent a binary field. In the context of acoustic imaging, it is useful for describing an obstacle embedded within a fixed background. In that case, the acoustic velocity is given as follows:

$$v_p(a(\mathbf{x})) = v_p^{min} + (v_p^{max} - v_p^{min})a(\mathbf{x})^p, \tag{3.3}$$

here $a(\mathbf{x})$ is the design variable, v_p^{max} and v_p^{min} are upper and lower bounds for v_p and p is a positive integer that penalizes intermediate values of a. In particular, $v_p(a = 0) = v_p^{min}$ and $v_p(a = 1) = v_p^{max}$. The exponent p affects the gradient with respect to the optimization variable a, however, its impact is much smaller than that of sensitivity filter parameters introduced in Section 3.4. Thus, In this work p is set to unity unless explicitly stated otherwise.

If it is desirable to identify more than just inclusion and background, a multimaterial model can be used. Let N_m be the number of acoustic values present in the model. For instance, $N_m = 3$ for a model with fixed background and inclusions with two distinct acoustic velocities. The design variable values $\{a_i\}_{i=1}^{N_m}$ may be mapped to the allowed acoustic values $\{v_{p,i}\}_{i=1}^{N_m}$ using Lagrange interpolating polynomials as follow:

$$v_p(a(\mathbf{x})) = \sum_{i=1}^{N_m} v_{p,i} \prod_{\substack{j=1 \\ j \neq i}}^{N_m} \frac{a(\mathbf{x}) - a_j}{a_i - a_j}. \tag{3.4}$$

Another interpolation scheme possible is the peak function material model used in (GONCALVES et al., 2020). In this approach the acoustic velocity is written as a sum of normalized gaussian curves:

$$v_p(a(\mathbf{x})) = \frac{1}{\sum_{j=1}^{N_m} \exp\left[\frac{(a(\mathbf{x})-a_j)^2}{2\sigma_j^2}\right]} \sum_{i=1}^{N_m} v_{p,i} \exp\left[\frac{(a(\mathbf{x}) - a_i)^2}{2\sigma_i^2}\right] \tag{3.5}$$

This interpolation introduces the standard deviation σ_i associated with the acoustic velocity $v_{p,i}$ as a free parameter. In this work, $\sigma_j = 0.3$ unless explicitly stated otherwise.

A plot of the peak model curve 3.5 for different values of σ_i and of the lagrange interpolation model 3.4 is shown in Figure 3.2. As can be seen there, the parameter σ_j allows manipulating the magnitude of the gradient of the material model with respect to the design variable at the allowed integer values, in this instance, $a \in \{0, 1, 2\}$. This in turn can be useful for amplifying or suppressing the magnitude of the gradient at selected value ranges of the design variable.
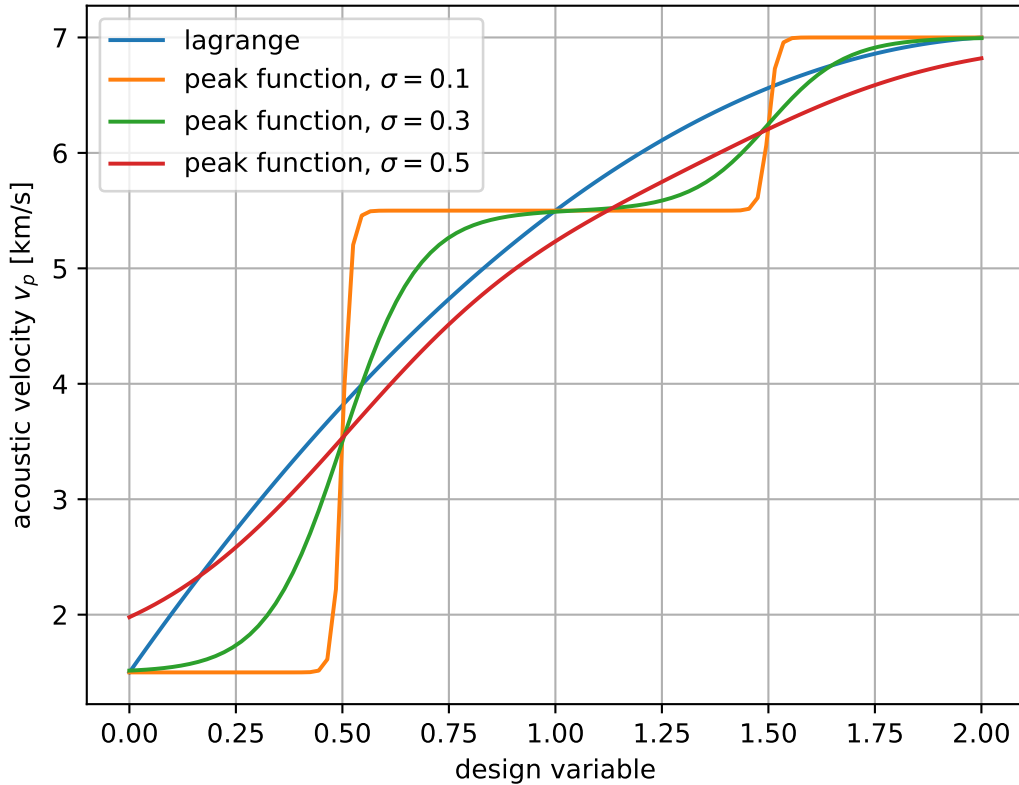
Figure 3.2 − Lagrange and peak function interpolating models. The peak function model is plotted with three different σ_j values to illustrate the influence of the parameter on the slope of the curve.

In this work, we propose formulating the acoustic imaging problem in the framework of TO, introducing the concept of material models and regularization through filtering of the sensitivities. The design variable is modeled as an integer field so as to better characterize sharp interfaces. In order to do so, the TOBS methodology from TO is employed. The parameter identification problem given in (3.1) is reframed into the TO formulation (3.2) via (3.3), (3.4) and (3.5), linking the acoustic velocity v_p with the design variable a.

3.2.2 TOBS method

For certain parameter identification problems such as damage detection and geophysical exploration, the correct positioning of material interfaces is crucial (WANG et al., 2019;

SEIDL; RANK, 2016). The TOBS method (SIVAPURAM; PICELLI, 2018), which incorporates discrete control variable values, seems fitting when tackling these problems via a TO based approach.

Let the design variable be $a \in \mathbb{R}^{N_{dim}}$ instead of $\boldsymbol{\rho}$, where N_{dim} is the dimension of vector a representing the optimization variable after spatial discretization by some method such as FDM or FEM. Each component $a_i \in \{0, 1, \ldots, N_m\}$, N_m being a positive integer. This formulation restricts the design variable to a piecewise constant field. The generic TO problem (3.2) can be rewritten in reduced form by noting that the state variable is implicitly defined by the design variable through the state equation. With these changes, the TO problem becomes:

$$\begin{aligned} \underset{a}{\text{minimize}} \quad & f(a) \\ \text{subject to} \quad & a_i \in \{0, 1, \ldots, N_m\}, \quad i = 1, \ldots, N_{dim} \end{aligned} \tag{3.6}$$

The optimization problem is then solved in a sequential fashion as shown in Algorithm 1.

Algorithm 1 Sequential Integer Linear Programming

1: $k \leftarrow 0$
2: $a^k \leftarrow$ design variable initial guess
3: Linearize $f(a) = f(a^k + \Delta a^k) \approx f(a^k) + \nabla_a f(a^k) \cdot \Delta a^k$
4: **while** stopping criteria not met **do**
5:     Solve linearized problem for integer Δa^k $\left(\triangleright\right) Eq.\ 3.8$
6:     $a^k \leftarrow a^k + \Delta a^k$
7:     $k \leftarrow k + 1$

Equation (3.6) is linearized around a certain a^k and truncated up to first order. The sub-problem seeking to minimize this linear approximation is:

$$\begin{aligned} \underset{\Delta a^k}{\text{minimize}} \quad & f(a^k) + \nabla_a f(a^k) \cdot \Delta a^k \\ \text{subject to} \quad & a_i \in \{0, 1, \ldots, N_m\}, \quad i = 1, \ldots, N_{dim} \end{aligned} \tag{3.7}$$

The solution Δa^k updates the design variable as $a^{k+1} = a^k + \Delta a^k$, which in turn generates a new sub-optimization problem for Δa^{k+1}. This procedure is repeated until a stopping criteria is met.

A bound M on the norm 1 of Δa^k is introduced to sub-problem (3.7). The objective is to limit the second order error in Δa^k, thus ensuring that the linearization of f stays a

reasonable approximation (PICELLI et al., 2020). Equation (3.7) then becomes:

$$
\begin{aligned}
\underset{\Delta a^k}{\text{minimize}} \quad & \nabla_a f \cdot \Delta a^k \\
\text{subject to} \quad & ||\Delta a^k||_1 \leq M \\
& a_i \in \{0, 1, \ldots, N_m\}, \quad i = 1, \ldots, N_{dim}
\end{aligned}
\tag{3.8}
$$

The constant $f(a^k)$ term was discarded from the objective function.

In order to actually implement the norm 1 bound as a linear constraint it is necessary to know the sign of Δa_i^k before (3.8) is solved. When $N_m = 1$ this is done by acknowledging that
$Delta a_i^k \in \{0, 1\}$ for $a_i = 0$ and $\Delta a_i^k \in \{-1, 0\}$ for $a_i = 1$. Hence, the norm constraint can be written as:

$$
||\Delta a^k||_1 = \sum_{i=1}^{N_{dim}} (1 - 2a_i^k)\Delta a_i^k \leq M
\tag{3.9}
$$

However, for $N_m \geq 2$ the sign of Δa_i^k is undetermined when $1 < a_i < N_m$. In order to keep the norm 1 constraint, the variation Δa^k is divided into a positive and a negative contribution such that $\Delta a^k = \Delta a_P^k + \Delta a_N^k$. Thus, Equation (3.8) can be rewritten as:

$$
\begin{aligned}
\underset{\Delta a^k}{\text{minimize}} \quad & \nabla_a f \cdot \Delta a^k \\
\text{subject to} \quad & \Delta a^k = \Delta a_P^k + \Delta a_N^k \\
& ||\Delta a_P^k||_1 \leq M/2 \\
& ||\Delta a_N^k||_1 \leq M/2 \\
& \Delta a_{i,P}^k \in \{0, 1 - 2H(a_i^k - N_m)\} \\
& \Delta a_{i,N}^k \in \{1 - 2H(a_i^k), 0\}
\end{aligned}
\tag{3.10}
$$

where $H(\cdot)$ denotes the Heaviside step function. The signs of $\Delta a_{i,P}^k$ and $\Delta a_{i,N}^k$ are known beforehand, allowing us to write the discretized version of (5.9) as an Integer Linear Problem (ILP).

Applying the TOBS formulation to the acoustic inverse problem (3.1), the optimization problem can be stated as:

$$
\begin{aligned}
\underset{a}{\text{minimize}} \quad & f = \sum_{s}^{N_s} \sum_{r}^{N_r} \int_0^T \int_\Omega (p_s(\mathbf{x}, t)\delta_{\mathbf{x}_r} - d_{s,r}(t))^2 \\
\text{subject to} \quad & \partial_{tt}p_s + \eta\partial_t p_s - v_p(a)^2 \Delta p_s = s(\mathbf{x}_s, t), \quad s = 1, \ldots, N_s, \\
& a_i \in \{0, 1, \ldots, N_m\}, \quad i = 1, \ldots, N_{dim}
\end{aligned}
\tag{3.11}
$$

It should be noted that the SIMP material model from Section 3.2.1 is restricted to binary configurations, that is, $N_m = 1$.

3.3 Sensitivity Analysis

In this section, the expression for the gradient of the objective function in 3.11 with respect to the control variable is obtained by the adjoint method (HINZE et al., 2008). Before that, a few useful properties from the Gateaux derivative are remembered.

3.3.1 Notation and properties

Consider an element $a \in V$, where V is some function space. For the mapping $v_p = v_p(a)$, the Gateaux derivative of v_p with respect to a in the direction δa is defined as:

$$Dv_p(a)[\delta a] := \lim_{\epsilon \to 0} \frac{1}{\epsilon}[v_p(a + \epsilon \delta a) - v_p(a)] \tag{3.12}$$

Now say there is some composite mapping $p = p(v_p(a))$. The Gateaux derivative of p in the direction δa is:

$$Dp(a)[\delta a] = \lim_{\epsilon \to 0} \frac{1}{\epsilon}[p(v_p(a + \epsilon \delta a)) - p(v_p(a))], \tag{3.13}$$

which from (3.12) equals:

$$Dp(a)[\delta a] = \lim_{\epsilon \to 0} \frac{1}{\epsilon}[p(v_p(a) + \epsilon \overbrace{Dv_p(a)[\delta a]}^{\delta v_p}) - p(v_p(a))] = Dp(v_p)[\delta v_p], \tag{3.14}$$

so the chain rule is valid. Besides, expanding (3.12) around $\epsilon = 0$ yields:

$$Dv_p(a)[\delta a] = \lim_{\epsilon \to 0} \frac{1}{\epsilon}[v_p(a) + \epsilon \partial_a v_p(a)\delta a + O(\epsilon^2) - v_p(a)] = \partial_a v_p(a)\delta a, \tag{3.15}$$

which shows that $Dv_p(a)[\delta a]$ is linear with respect to the differentiation direction δa. Lastly, if v_p is linear, then:

$$Dv_p(a)[\delta a] = \lim_{\epsilon \to 0} \frac{1}{\epsilon}[v_p(a) + \epsilon v_p(\delta a) - v_p(a)] = v_p(\delta a). \tag{3.16}$$

3.3.2 Gradient by the adjoint method

The objective function from (3.11) is rewritten as:

$$
\begin{aligned}
f &= \sum_{s=1}^{N_s} \sum_{r=1}^{N_r} \int_0^T \int_\Omega (p_s(\mathbf{x}, t)\delta_{\mathbf{x}_r} - d_{s,r}(t))^2 \\
&= \sum_{s=1}^{N_s} \int_0^T \int_\Omega \underbrace{\sum_{r=1}^{N_r} (p_s(\mathbf{x}, t)\delta_{\mathbf{x}_r} - d_{s,r}(t))^2}_{g_s(p_s)} \\
&= \sum_{s=1}^{N_s} \langle 1, g_s(p_s) \rangle,
\end{aligned}
\tag{3.17}
$$

where $\langle \cdot, \cdot \rangle$ is a compact way of expressing the integral over $\Omega \times (0, T]$. The acoustic wave equation is represented by the differential operator:

$$L(a, p) = \partial_{tt}p + \eta \partial_t p - v_p(a)^2 \Delta p. \tag{3.18}$$

In order to evaluate the gradient, the Lagrangian corresponding to the optimization problem is formed. Since the box constraints are handled by the optimizer, only the PDE constraint is considered:

$$\mathcal{L}(p_1, \ldots, p_{N_s}, a, \psi_1, \ldots, \psi_{N_s}) = \sum_{s=1}^{N_s} \langle 1, g_s(p_s) \rangle - \sum_{s=1}^{N_s} \langle \lambda_s, L(a, p_s) - s(\mathbf{x}_s, t) \rangle. \tag{3.19}$$

Taking the variation of the Lagrangian with respect to the control variable we obtain:

$$
\begin{aligned}
D_a \mathcal{L}[\delta a] &= \sum_{s=1}^{N_s} \langle 1, D_a g_s(p_s(a))[\delta a] \rangle - \sum_{s=1}^{N_s} \langle \lambda_s, D_a L(a, p_s)[\delta a] \rangle \\
&= \sum_{s=1}^{N_s} \langle 1, D_{p_s} g_s(p_s)[\delta p_s] \rangle - \sum_{s=1}^{N_s} \langle \lambda_s, \partial_a L(a, p_s)[\delta a] + \partial_{p_s} L(a, p_s)[\delta p_s] \rangle \\
&= \sum_{s=1}^{N_s} \langle \delta p_s, \partial_{p_s} g_s \rangle - \sum_{s=1}^{N_s} \langle \lambda_s, \partial_a L(a, p_s)[\delta a] \rangle - \sum_{s=1}^{N_s} \langle \lambda_s, \partial_{p_s} L(a, p_s)[\delta p_s] \rangle,
\end{aligned} \tag{3.20}
$$

where $\delta p_s = D_a p_s[\delta a]$. In particular, the evaluation of δp_s is computationaly expensive, and it would be preferable to avoid it altogether. Assuming the existence of an operator $L^\dagger$ such that:

$$\langle \delta p_s, \partial_{p_s} L^\dagger(a, p)[\lambda_s] \rangle = \langle \lambda_s, \partial_{p_s} L(a, p)[\delta p_s] \rangle, \tag{3.21}$$

then (3.20) can be written as:

$$
\begin{aligned}
D_a \mathcal{L}[\delta a] &= \sum_{s=1}^{N_s} \langle \delta p_s, \partial_{p_s} g_s \rangle - \sum_{s=1}^{N_s} \langle \lambda_s, \partial_a L(a, p_s)[\delta a] \rangle - \sum_{s=1}^{N_s} \langle \delta p_s, \partial_{p_s} L^\dagger(a, p)[\lambda_s] \rangle \\
&= - \sum_{s=1}^{N_s} \langle \lambda_s, \partial_a L(a, p_s)[\delta a] \rangle - \sum_{s=1}^{N_s} \langle \delta p_s, \partial_{p_s} L^\dagger(a, p)[\lambda_s] - \partial_{p_s} g_s \rangle.
\end{aligned} \tag{3.22}
$$

Furthermore, if we can find λ_s such that:

$$\partial_{p_s} L^\dagger(a, p)[\lambda_s] - \partial_{p_s} g_s, \quad s = 1, \ldots, N_s, \tag{3.23}$$

then the expression for the gradient becomes:

$$D_a \mathcal{L}[\delta a] = - \sum_{s=1}^{N_s} \langle \lambda_s, \partial_a L(a, p_s)[\delta a] \rangle \tag{3.24}$$

The expression $\partial_a L(a, p_s)$, while general, obfuscates the dependence of the gradient on the selected material model. As detailed in Section 3.2.1 and illustrated in Figure 3.2, varying the material model and parameter selections alters the interpolation curve's slope,

consequently affecting the gradient concentration around sharp interfaces.

3.3.2.1 Adjoint equation

In order to solve (3.23) it is necessary first to derive appropriate boundary and initial conditions. Since L is linear in p_s, the right hand side of (3.21) can be rewritten as:

$$\langle \lambda_s, \partial_{p_s} L(a,p)[\delta p_s] \rangle = \langle \lambda_s, L(a, \delta p_s) \rangle = \langle \lambda_s, \partial_{tt}\delta p_s \rangle + \langle \lambda_s, \eta\partial_t\delta p_s \rangle + \langle \lambda_s, v_p^2\,\Delta\delta p_s \rangle. \quad (3.25)$$

Integrating by parts, the terms containing the time derivatives can be expanded as:

$$
\begin{aligned}
\langle \lambda_s, \partial_{tt}\delta p_s \rangle &= \int_\Omega \lambda_s\partial_t\delta p_s\Big|_0^T - \int_\Omega \partial_t\lambda_s\delta p_s\Big|_0^T + \langle \delta p_s, \partial_{tt}\lambda_s \rangle \\
&= \int_\Omega \lambda_s(\cdot,T)\partial_t\delta p_s(\cdot,T) - \int_\Omega \partial_t\lambda_s(\cdot,T)\delta p_s(\cdot,T) \\
&\quad - \int_\Omega \lambda_s(\cdot,0)\partial_t\delta p_s(\cdot,0) + \int_\Omega \partial_t\lambda_s(\cdot,0)\delta p_s(\cdot,0) + \langle \delta p_s, \partial_{tt}\lambda_s \rangle \\
&= \int_\Omega \lambda_s(\cdot,T)\partial_t\delta p_s(\cdot,T) - \int_\Omega \partial_t\lambda_s(\cdot,T)\delta p_s(\cdot,T) + \langle \delta p_s, \partial_{tt}\lambda_s \rangle \\
&= \langle \delta p_s, \partial_{tt}\lambda_s \rangle,
\end{aligned}
\quad (3.26)
$$

$$\langle \lambda_s, \eta\partial_t\delta p_s \rangle = \int_\Omega \lambda_s\eta\delta p_s\Big|_0^T - \langle \eta\delta p_s, \partial_t\lambda_s \rangle = -\langle \eta\delta p_s, \partial_t\lambda_s \rangle \quad (3.27)$$

if λ satisfy quiescent terminal conditions $\lambda_s(\cdot,T) = \partial_t\lambda_s(\cdot,T) = 0$.

Similarly, the term containing the laplacian can be extended as:

$$
\begin{aligned}
\langle \lambda_s, v_p^2\,\Delta\delta p_s \rangle &= \int_0^T \int_{\partial\Omega} \lambda_s v_p^2\partial_n\delta p_s - \int_0^T \int_{\partial\Omega} \partial_n\lambda_s v_p^2\delta p_s + \langle \delta p_s, v_p^2\,\Delta\lambda_s \rangle \\
&= \int_0^T \int_{\Gamma_D} \lambda_s v_p^2\partial_n\delta p_s - \int_0^T \int_{\Gamma_D} \partial_n\lambda_s v_p^2\delta p_s \\
&\quad + \int_0^T \int_{\Gamma_N} \lambda_s v_p^2\partial_n\delta p_s - \int_0^T \int_{\Gamma_N} \partial_n\lambda_s v_p^2\delta p_s \\
&\quad + \int_0^T \int_{\Gamma_A} \lambda_s v_p^2\partial_n\delta p_s - \int_0^T \int_{\Gamma_A} \partial_n\lambda_s v_p^2\delta p_s + \langle \delta p_s, v_p^2\,\Delta\lambda_s \rangle.
\end{aligned}
\quad (3.28)
$$

The boundary terms where Dirichlet conditions are imposed vanish if $\lambda_s(\Gamma_D, \cdot) = 0$. Likewise, Neumann terms vanish if $\partial_n\lambda_s(\Gamma_N, \cdot) = 0$. On Γ_A, where the transparency boundary conditions (2.8) are imposed, we have:

$$
\begin{aligned}
\int_0^T \int_{\Gamma_A} \lambda_s v_p^2\partial_n\delta p_s - \int_0^T \int_{\Gamma_A} \partial_n\lambda_s v_p^2\delta p_s &= -\int_0^T \int_{\Gamma_A} \lambda_s v_p\delta\dot{p}_s - \int_0^T \int_{\Gamma_A} \partial_n\lambda_s v_p^2\delta p_s \\
&= -\int_{\Gamma_A} \lambda_s v_p\delta p_s\Big|_0^T + \int_0^T \int_{\Gamma_A} \dot{\lambda}_s v_p\delta p_s \\
&\quad - \int_0^T \int_{\Gamma_A} \partial_n\lambda_s v_p^2\delta p_s \\
&= \int_0^T \int_{\Gamma_A} (\frac{1}{v_p}\dot{\lambda}_s - \partial_n\lambda_s)v_p^2\delta p_s,
\end{aligned}
\quad (3.29)
$$

which equals zero if the transformed adjoint variable $\lambda_s^\dagger(\cdot, t) = \lambda_s(\cdot, -t)$ also satisfies (2.8). This is the case since λ_s needs to be subjected to a reflection in the time axis $t \to -t$ in order to transform terminal conditions into initial ones. As a consequence, the first derivative is also transformed as $\dot{\lambda}_s \to -\dot{\lambda}_s^\dagger$. Note that this transforms the sign of the adjoint damping.

The adjoint condition can then be recast as:

$$\begin{aligned}
\langle \lambda_s, L(a, \delta p_s) \rangle &= \langle \lambda_s, \partial_{tt}\delta p_s + \eta\partial_t\delta p_s - v_p^2\,\Delta\delta p_s \rangle \\
&= \langle \delta p_s, \partial_{tt}\lambda_s - \eta\partial_t\lambda_s - v_p^2\,\Delta\lambda_s \rangle = \langle \delta p_s, L(a, \lambda_s) \rangle,
\end{aligned} \tag{3.30}$$

which holds if $\lambda_s^\dagger$ satisfies the adjoint problem:

$$\begin{aligned}
\partial_{tt}\lambda_s^\dagger + \partial_t\lambda_s^\dagger - v_p^2\Delta\lambda_s^\dagger = s(\mathbf{x}_s, t), \quad s &= 1, \ldots, N_s \\
\lambda_s^\dagger(\mathbf{x}, t) &= 0 \quad \text{on} \quad \Gamma_D \\
\partial_n\lambda_s^\dagger(\mathbf{x}, t) &= 0 \quad \text{on} \quad \Gamma_N \\
\frac{1}{v_p}\frac{\partial\lambda_s^\dagger}{\partial t} + \mathbf{n}\cdot\nabla\lambda_s^\dagger &= 0 \quad \text{on} \quad \Gamma_A \\
\lambda_s^\dagger(\mathbf{x}, 0) &= 0 \quad \text{in} \quad \Omega_{ext} \\
\partial_t\lambda_s^\dagger(\mathbf{x}, 0) &= 0 \quad \text{in} \quad \Omega_{ext}
\end{aligned} \tag{3.31}$$

3.4   Regularization

3.4.1   Spatial filter

As an ill-posed problem, the inversion procedure can present numerical instabilities when tackled directly. In order to deal with those we utilize filtering applied to the sensitivity (SIGMUND; PETERSSON, 1998). In particular, we apply a Helmholtz-like PDE filter (LAZAROV; SIGMUND, 2011). Given a sensitivity field g, its filtered version $\hat{g}$ is computed as:

$$\begin{aligned}
-r^2\Delta\hat{g} + \hat{g} &= g, \\
\partial_n\,\hat{g} &= 0
\end{aligned} \tag{3.32}$$

where r is related to the degree of smoothness of the filtered field, see Figure 3.3.

3.4.2   Stability filter

As a highly sensitive identification problem with scarcity of information, the proposed sequential integer linear programming approach frequently results in objective funtions which oscilate wildly during the optimization process, see Figure 3.4a. This often leads to numerical instabilities that grow until the optimization result diverges. Seeking inspiration from methods that utilize only subsets of data such as Stochastic Gradient Descent
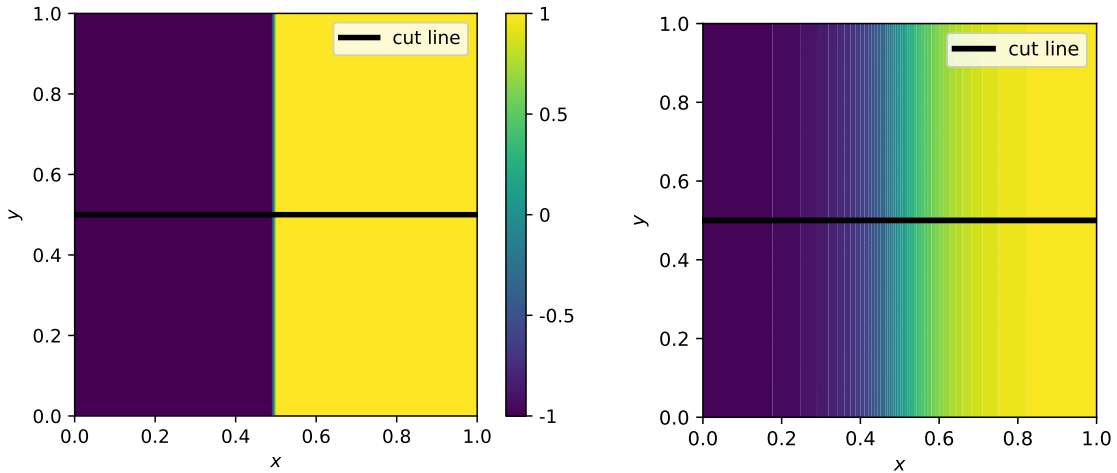
(a) Generic field $f(x, y)$ with sharp interface at $x = 0.5$. **(b)** Result of smoothing filter over $f(x, y)$ with $r = 0.1$.
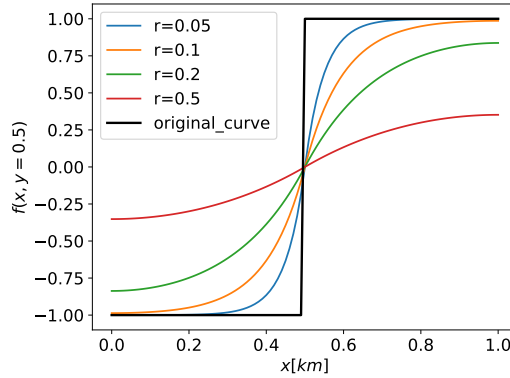
(c) Cross section of the field in (a) at the position $y = 0.5$, before and after the application of the smoothing filter with various choices of r.

Figure 3.3 − Illustration of the smoothing filter.

(RUDER, 2016), an Adam (KINGMA; BA, 2014) based damping filter which incorporates the whole history of sensitivities up to iteration k, instead of just the evaluation for the current control variable a is used. The process consists mainly in taking exponentially weighted averages of both the gradient, the element-wise product of the gradient with itself, and combining those using the average of the squares as a normalization factor for the average of the gradients.

After taking the filtered sensitivity $\hat{g}_k$ at iteration k, the moving average m of the gradients, also called first moment, is evaluated as:

$$m_k = \gamma_m m_{k-1} + (1 - \gamma_m)\hat{g}, \tag{3.33}$$

where γ_m is the so called forgetting factor. The second moment v at iteration k, which is the moving average of the Hadamard product of the gradient g by itself, is taken as:

$$v_k = \gamma_v v_{k-1} + (1 - \gamma_v)\hat{g} \odot \hat{g}, \tag{3.34}$$
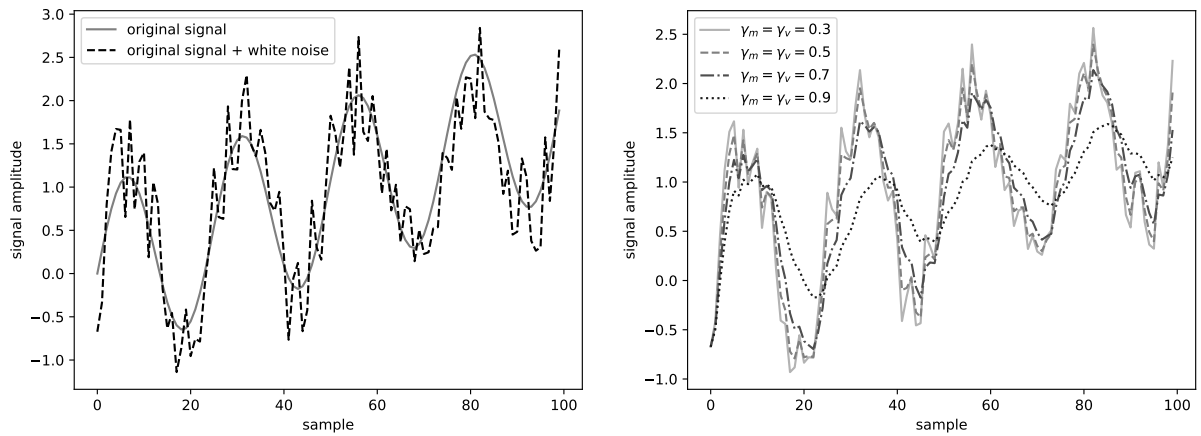
(a) Generic signal with high frequency oscillations. **(b)** Damped signals. The forgetting factors γ_m and γ_v are assumed equal.

Figure 3.4 − Illustrative example of the Adam based damping filter. A generic noisy signal is shown in Figure (a). The effect of the exponentially weighted averaging for different weight factors γ_m and γ_v is shown in Figure (b).

where γ_v is the forgetting factor for the "squared" gradient. Finally, the damped gradient is calculated as:

$$\tilde{g}_k = \frac{m_k}{\sqrt{v_k + \varepsilon}}, \tag{3.35}$$

where ε is a small number such as 10^{-6} so as to avoid singular divisions. Figure 3.4b shows the result of this averaging over a noisy signal.

4 NUMERICAL IMPLEMENTATION

In order to solve the wave propagation problem it is necessary to discretize the variational problem stated in a continuous setting. We do so by first chosing a time discretization in terms of finite differences in 4.1. Next, a spatial discretization convenient to wave propagation is presented in 4.2. This discretization is implemented through the spyro software, which is built on top of Firedrake (RATHGEBER et al., 2016b). The core concept of Firedrake is presented in 4.3. The IBM ILOG CPLEX software, through which the optimization is carried out, is briefly introduced in 4.4. The integration of spyro with CPLEX is discussed, and the whole procedure is summarized in 4.5.

4.1 Time discretization

The variational problem (2.14) can be solved either in the time or in the frequency domain, each more or less adequate depending on the problem at hand (VIRIEUX; OPERTO, 2009). A second order time-domain explicit discretization is chosen, mostly because of memory requirements of the frequency domain approach, and also because numerical errors are usually dominated by spatial discretization, rendering more elaborate schemes not worth the extra computational effort (FICHTNER, 2010).

Discretizing the time domain with $N + 1$ samples Δt apart, $p(\mathbf{x}, t)$ becomes $p(\mathbf{x}, t_n)$, or p_n for short. Employing a second order finite difference approximation leads to:

$$\ddot{p}_n = \frac{p_{n+1} - 2p_n + p_{n-1}}{\Delta t^2}. \tag{4.1}$$

Substitution on equation (2.14) at instant $t = n\Delta t$ leads to:

$$
\begin{aligned}
(p^{n+1}, q) = {} & 2(p^n, q) - (p^{n-1}, q) \\
& - \Delta t(p_n, q)_\eta + \Delta t(p_{n-1}, q)_\eta \\
& - \Delta t^2 a(p^n, q) + \Delta t^2 l(q)
\end{aligned}
\tag{4.2}
$$

4.2 Spatial discretization

The Finite Element Method is used to discretize the $N + 1$ variational problems in (4.1). Approximating V and $\hat{V}$ with the same finite dimensional space V^h of dimension N_d and basis ϕ_i, $i = 1, \ldots, N_d$, the finite element approximations of p_k becomes $p_k^h = \sum_j P_k^j \phi_j$.

Since q is arbitrary, we let its approximation q^h be $q^h = \phi_i$. Dropping the subindex in

p_{n+1}, one can write the system (4.1) as:

$$\sum_{j}^{N_d} (\phi_i, \phi_j) P^j = \Delta t^2 \left[l(\phi_i) - \sum_{j}^{N_d} a(\phi_i, \phi_j) P_n^j \right] + \sum_{j}^{N_d} 2(\phi_i, \phi_j) P_n^j - \sum_{j}^{N_d} (\phi_i, \phi_j) P_{n-1}^j, \quad (4.3)$$

valid for some integer i up to N_d. One can go further and use the fact that these basis functions have compact support to define the components of elementar and global matrices, cover reference elements, quadratures for evaluating the resulting integrals and so on (HUGHES, 2012). Since this work employs Firedrake, which automates these implementation steps, this discussion is skipped.

System (4.3) can be rewritten as:

$$\begin{aligned}
\mathbf{M}\mathbf{p}^{n+1} = {} & \mathbf{M} \left(2\mathbf{p}^n - \mathbf{p}^{n-1} \right) \\
& + \Delta t \mathbf{C} \left(2\mathbf{p}^{n-1} - \mathbf{p}^n \right) \\
& + \Delta t^2 \left(\mathbf{f} - \mathbf{K}\mathbf{p}^n \right),
\end{aligned} \quad (4.4)$$

where $\mathbf{M}$ is the mass matrix, $\mathbf{C}$ is the damping matrix, $\mathbf{K}$ is the stiffness matrix, $\mathbf{f}$ is the force vector and $\mathbf{p}_k$ is the pressure at instant k. Their components can be identified from (4.3) as:

$$\begin{aligned}
M_{i,j} &= (\phi_i, \phi_j) \\
C_{i,j} &= (\phi_i, \phi_j)_\eta \\
K_{i,j} &= a(\phi_i, \phi_j) \\
f_i &= l(\phi_i)
\end{aligned} \quad (4.5)$$

As can be seen from (4.4), $\mathbf{p}$ can be obtained at once by inverting the mass matrix $\mathbf{M}$. The problem with most choices of basis functions is that they do not generate diagonal mass matrices, or do render them diagonal, but only under certain circunstances, such as Lagrangian basis functions in hexahedral meshes with nodes collocated at so called GLL points (KOMATITSCH; VILOTTE, 1998). For unstructured triangular meshes, it is possible to utilize higher order bubble basis functions (CHIN-JOE-KONG; MULDER; VELDHUIZEN, 1999) in order to achieve diagonal mass matrices. These mass lumped elements were implemented in Firedrake (ROBERTS; OLENDER; FRANCESCHINI, 2021), and are utilized in this work.

4.3 Firedrake

The solution of (4.4) at each time step is implemented in Firedrake (RATHGEBER et al., 2016b). Firedrake is an automated system for the solution of partial differential equation using the Finite Element Method. It is an offshoot of FEniCS (ALNÆS et al., 2015), both software stacks which utilize Domain Specific Languages (DSL) to automatically generate

optimized C/C++ code from high level languages embedded in python.

The DSL embedded in python is Unified Form Language (UFL) (ALNÆS et al., 2014), which is used to write variatonal forms for FEM implementations. With the aid of the finite element library FinAT (HAM et al.,), the information about the variational problem and its FEM discretization is taken by a dedicated compiler that generates optimized C code (HOMOLYA et al., 2018). The solution of the discretized problem is achieved through integration with the linear algebra backend provided by PETSc (BALAY et al., 1997).

4.4   CPLEX

The IBM ILOG CPLEX Optimizer is used for solving optimization problems with continuous variables such as Linear Programming and Quadratic Programming, and most importantly for this work, it also allows modelling Mixed Integer Programming (MIP) problems, where some or all variables assume only integer values.

The ILP problem (3.8) is solved with CPLEX by a Branch & Bound algorithm (WOLSEY, 2020). After relaxation as an LP problem, the resulting feasible set is divided. This leads to the generation of new LP (Linear Programming) sub-problems. Solving these sub-problems helps to narrow down the feasible space and subsequently partition it more effectively, which guides the process towards finding the desired integer solution.

4.5   Procedure

The inversion procedure is carried out using spyro (ROBERTS; OLENDER; FRANCESCHINI, 2021), an acoustic wave modelling library built on top of Firedrake. The acoustic wave modelling for both the forward and adjoint problems is carried out in spyro, while the model updated is performed with CPLEX. The corresponding workflow is displayed in Figure 4.1.

The convergence criteria stipulate that the optimization should be carried out until either the objective function variation between two consecutive iterations or the norm 2 of the gradient becomes smaller than certain thresholds:

$$J^{i+1} - J^i \leq \tau_J \tag{4.6}$$

$$||\nabla J||_2 \leq \tau_G \tag{4.7}$$

where i is the iteration index, τ_J and τ_G are the convergence thresholds related to objective function J and gradient norm $||\nabla J||$, respectively. In addition, the optimization halts if a predetermined maximum number of iterations N_{max} is reached.
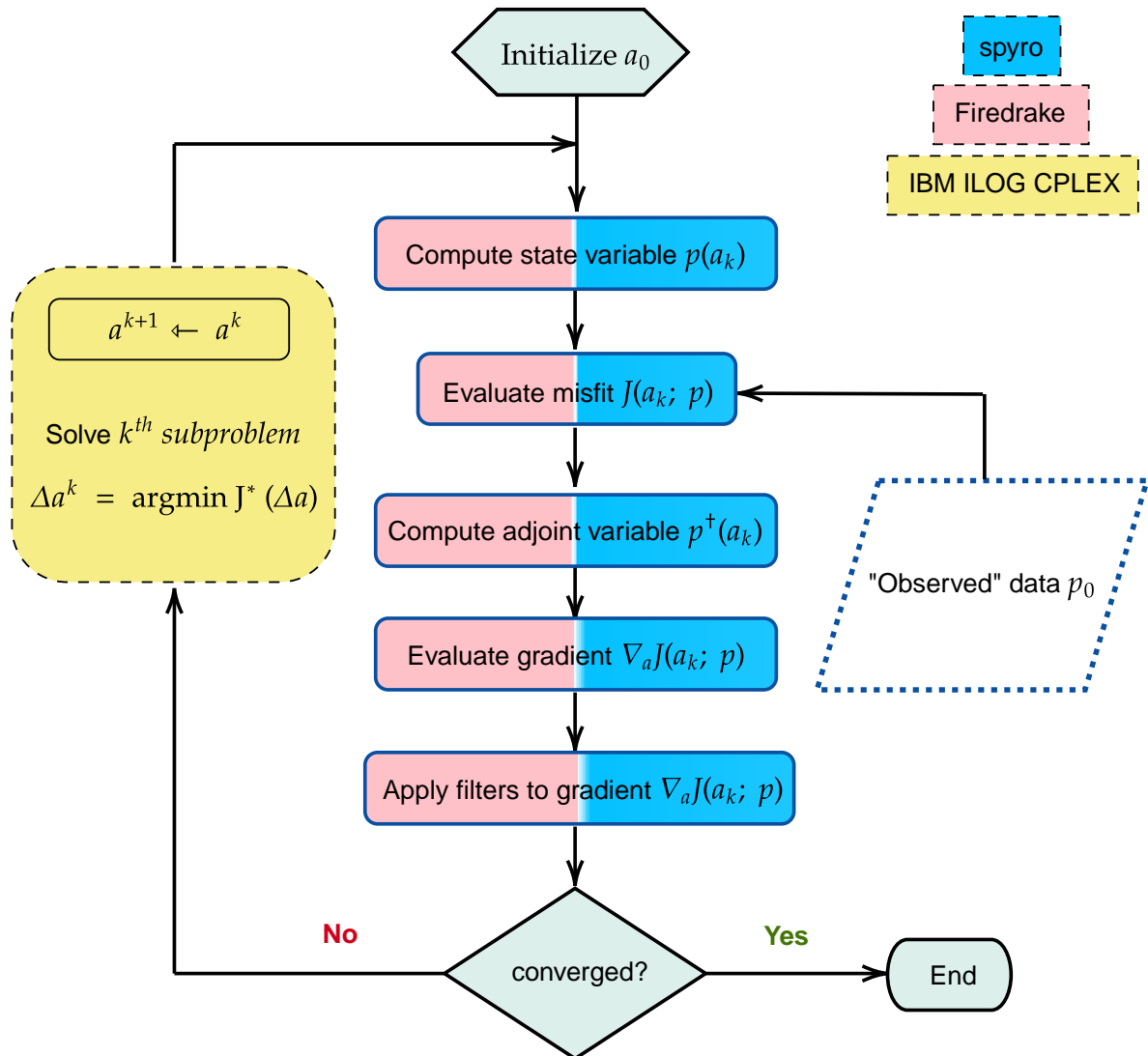
Figure 4.1 − Flowchart of the inversion procedure with integer variable.

5 RESULTS

In this chapter the proposed approach is applied to several numerical examples in order to showcase different characteristics from both the problem considered and method proposed.

In section 5.1 three examples of acoustic inverse problems are presented. First, the viablity and impact of parameters related to the method are evaluated. Then, the introduction of a multiscale approach is motivated and the influence of the inverse crime is discussed. Finally, a simple 3D case is presented.

In section 5.2, two cases in the context of FWI are presented. First, a velocity model with salt bodies embedded in a homogeneous medium is reconstructed. This example allows comparing the ILP approach to alternatives such as the Level Set method, assessing the impact of the initial guess and exploring the influence of physical parameters on the result. The last example studies a velocity model representative of the Santos Basin. This model in particular is caracterized by the presence of a thick salt layer. At first, the possibility of locating the salt is investigated. Then, the possibility of locating both the salt and a hydrocarbon reservoir ie explored. Finally, a more realistic example is explored, with a known top of salt, but unknown velocity distribution beneath it.

5.1 Acoustic Inverse Problem

5.1.1 Viability

To investigate the viability of the procedure, a single obstacle identification problem from Lanznaster et al. (2021) is chosen. Velocity model and geometry acquisition are shown in Figure 5.1. Parameters that describe the problem such as background and inclusion velocities, dimensions, signal from the source and acquisition configuration are displayed in Table 5.1. We refer to this example as case I.

In order to perform the identification procedure, reference data corresponding to the

Problem parameters			
background velocity	1 km/s	Number of sources N_s	3
inclusion velocity	3.5 km/s	Number of receivers N_r	42
length	2 km	source distance from surface	0.05 km
depth	2 km	receiver distance from surface	0.05 km
source central frequency	2 Hz	source offset	0.95 km
event duration	2.6 s	receiver offset	0.095 km

Table 5.1 − Parameters that describe the inversion problem case I.

Inversion parameters			
1-norm constraint M	0.02	objective function threshold τ_J	1×10^{-16}
Maximum number of iterations N_{max}	500	gradient threshold τ_G	1×10^{-14}

Table 5.2 − Inversion parameters used in case I.
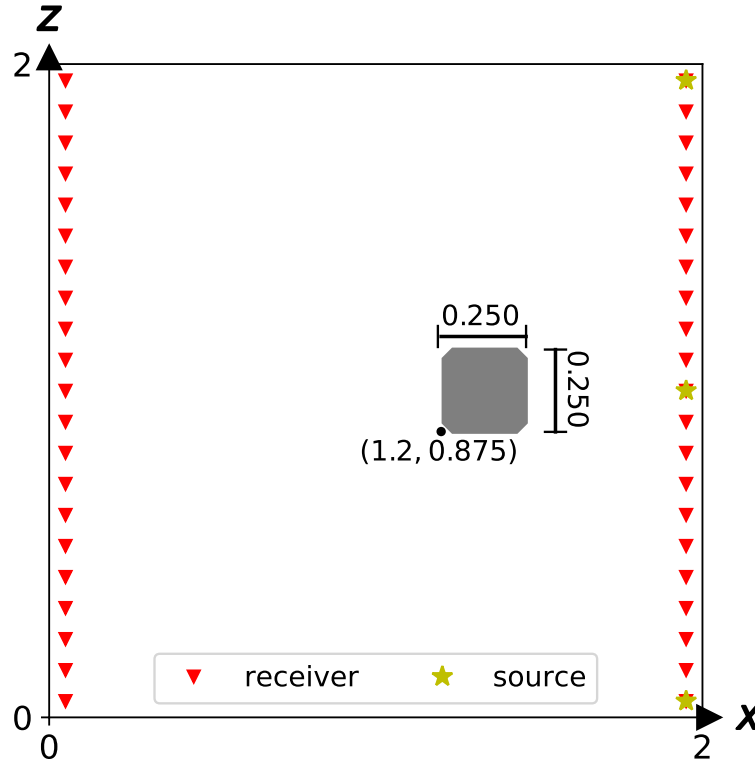
Figure 5.1 − Inclusion position and dimensions for case I.

target model is artificially generated. Each source is simulated individually and generates a "shot record", pressure disturbances that are measured at the receivers. The sources emit a pulse like signal corresponding to a Ricker wavelet (WANG, 2015).

The domain is discretized with a uniform triangular mesh of 14400 elements, and the timestep employed is $\Delta t = 0.001$ s. In this example the same mesh is used both for generating the synthetic signal and performing the inversion. The 1-norm constraint M from Equation 3.8 and the the stopping criteria parameters from Equation 4.6 are shown in Table 5.2. The inversion begins with a homogeneous velocity model corresponding to the background velocity $v_p = 1$ km/s.

Results at different points of the procedure can be seen in Figure 5.2. From the beginning several spurious inclusions appear, and only proliferate as the inversion goes on. This amplification of high frequency errors is typical of ill-posed problems (ENGL; HANKE; NEUBAUER, 1996), and serves as motivation for borrowing filtering techniques from other fields that deal with ill-posedness such as topology optimization (BOURDIN, 2001).

(a) At update 1.

(b) At update 4.

(c) At update 8.

(d) At update 19.
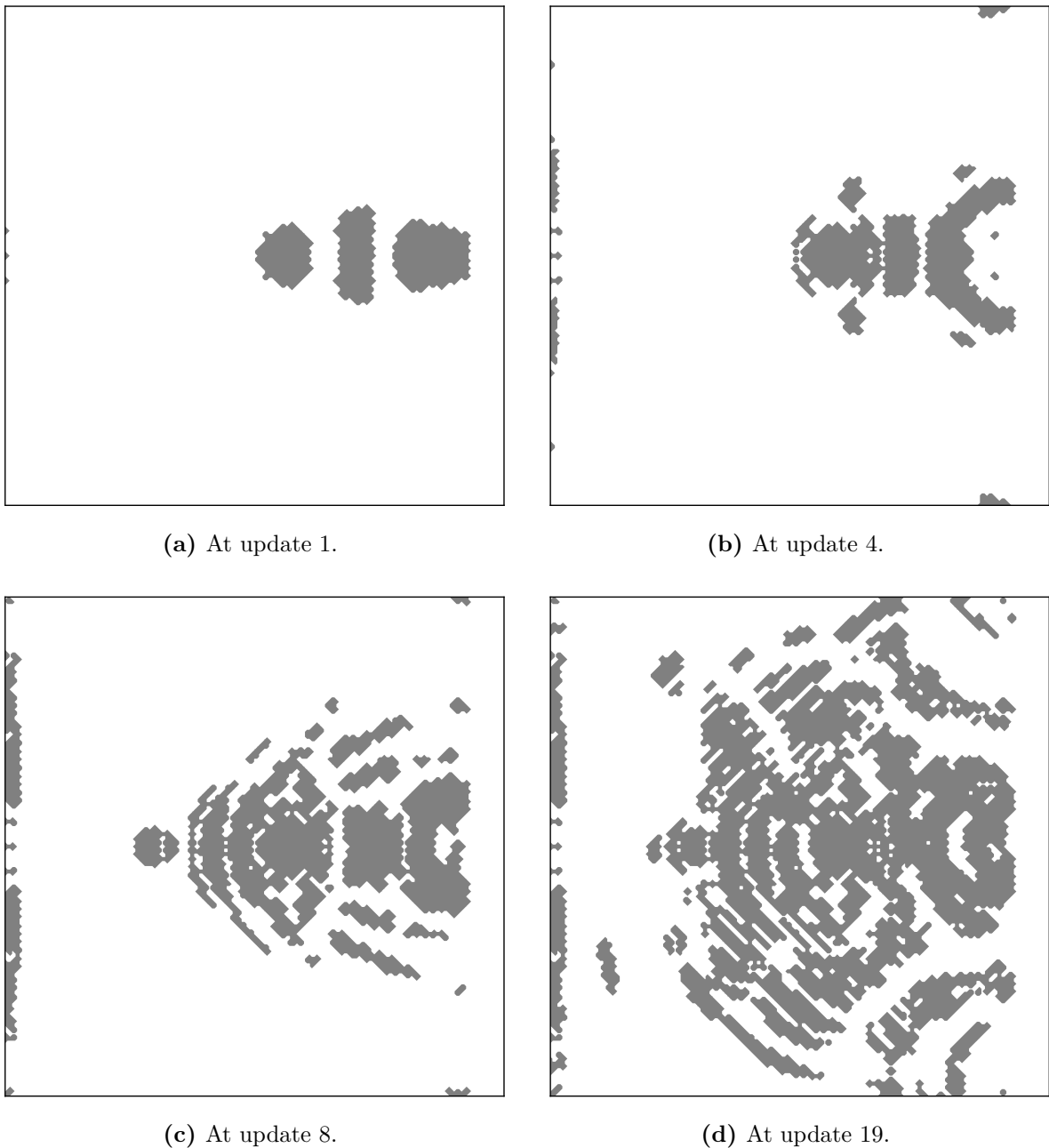
Figure 5.2 − Imaging evolution without sensitivity filtering.

Figure 5.3 shows the inversion procedure with the spatial sensitivity filter from Section 3.4.1 applied, here with filtering radius $r = 0.2$. In Topology Optimization, filters are known not only for alleviating ill-possedness but also for promoting some sort of length scale control (SIGMUND; MAUTE, 2012). A similar phenomenom can be seen here, as the appearance of spurious inclusions is delayed and, up to the first 50 iterations the scale of the obstacle being imaged is controlled.

The inversion is repeated once more, now with the combination of spatial and stabilization filter. The later, based on the Adam method (KINGMA; BA, 2014) popular in Machine Learning, is appropriate for problems which are very noisy or have sparse gradients.
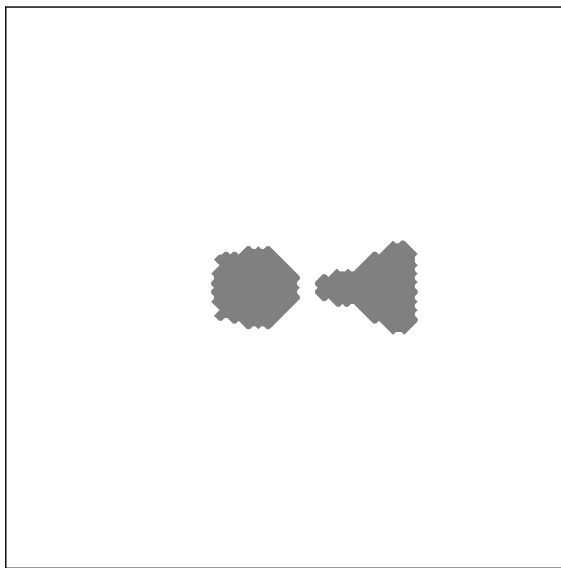
(a) At update 8.
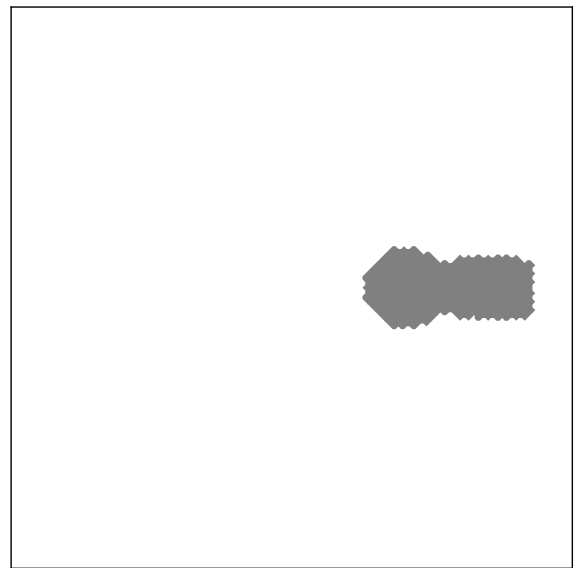
(b) At update 52.
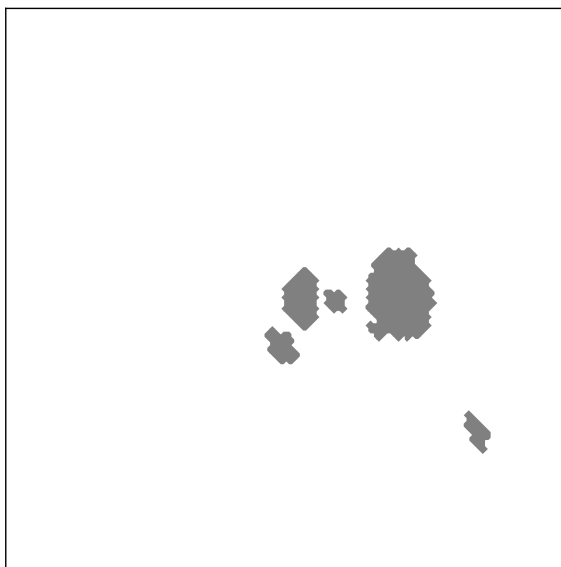
(c) At update 69.
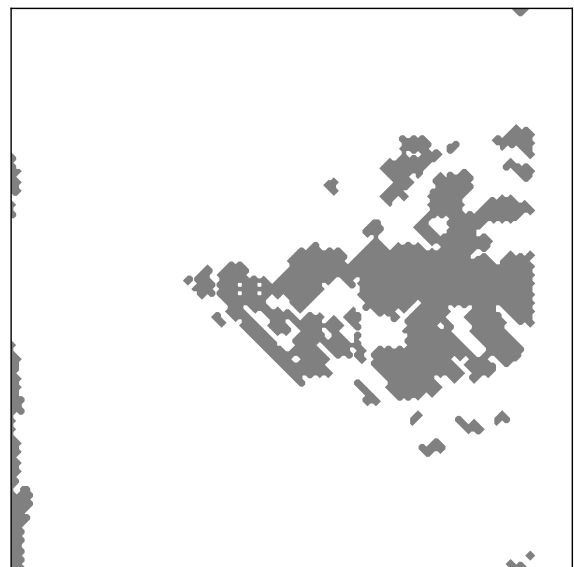
(d) At update 123.

Figure 5.3 − Imaging evolution with Helmholtz sensitivity filtering.

As a problem with restricted information, acoustic inversion seems like an appropriate fit for that methodology. The weighting parameters (From Equations (3.33),(3.34)) used here are $\gamma_m = \gamma_v = 0.999$. Results can be seen in Figure 5.4. The smoothing from the spatial filter is initially able to damp the propagation of spurious information from the gradient, thus restricting the scale of the inclusion being imaged until approximately iteration 52, when small artifacts start to appear and the optimization process diverges. The compound spatial filter with Adam-based averaging achieves results much closer to the true model.

It.	no regularization	Helmholtz filter	Helmholtz + Adam filter
8			
52			
69			
123			
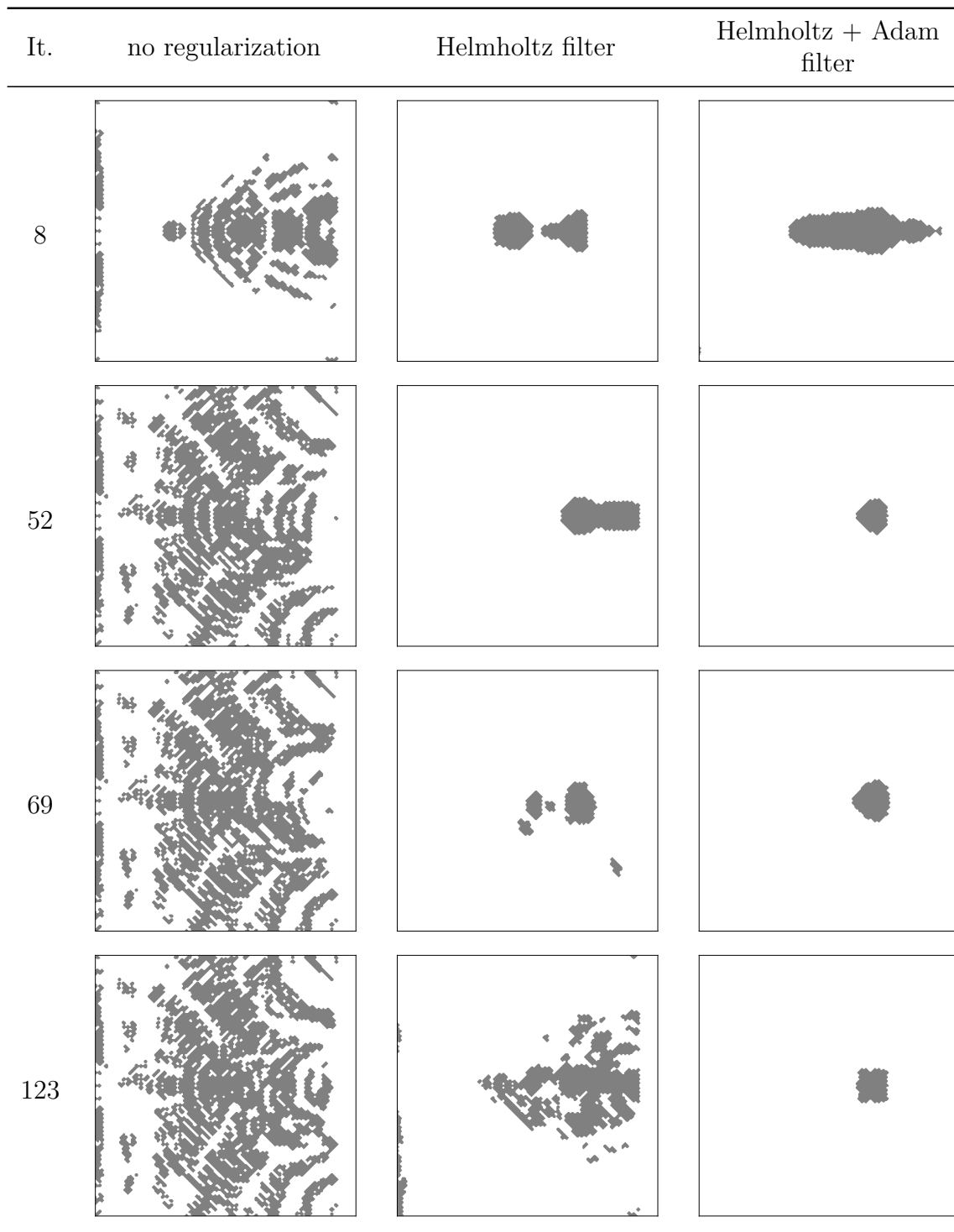
Figure 5.4 − Effect of the filters over the solution.

5.1.2 Frequency content

The timestep $\Delta t = 0.001$ s used in Section 5.1.1 was given without mention of stability or degree of accuracy. A brief justification for both is given in this Section. The same arguments apply for all remaining examples in this work.

The maximum timestep size is affected by the mesh size and acoustic velocity through the Courant-Friedrichs-Lewy (CFL) condition (FICHTNER, 2010). The wave propagator Spyro allows checking the stability condition for a mesh with triangular elements using Gershgoring disk theorem (ROBERTS et al., 2022). According to that criterion, the maximum timestep size is $\Delta t_{max} = 0.0055$ s. Furthermore, the timestep corresponds to the Nyquist sampling rate of a signal with frequency content up to $1/(2\Delta t) = 500$ Hz (BRIGHAM, 1988). Figure 5.5 and 5.6 show the shot record generated from the source at the center of the right boundary and its Fourier transform, respectively. As can be seen, the stability condition is far stricter than the sampling rate associated with the highest frequency present in the signal, and in general it is safe to assume that no content is being lost due the timestep being used.
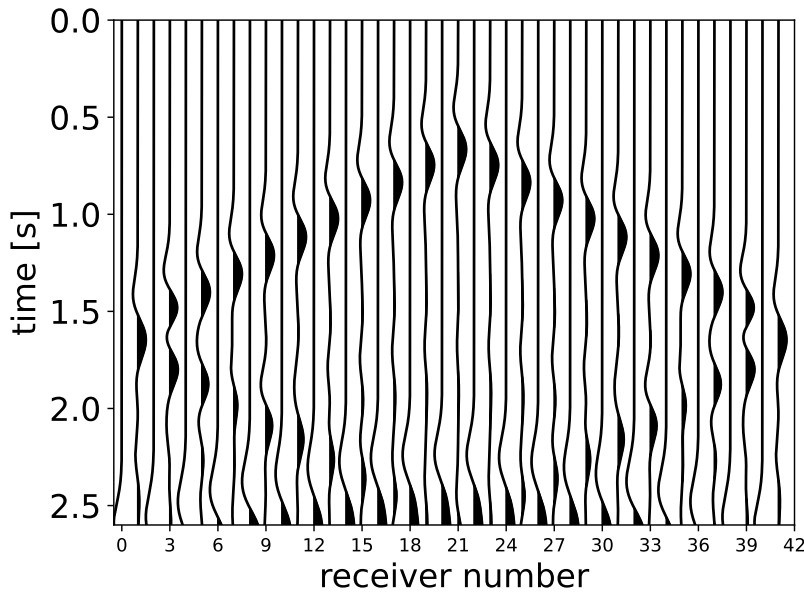
Figure 5.5 − Normalized signal in the time domain.

5.1.3 Parameter sweeping

The influence of the free parameters r (Helmholtz), γ_m, γ_v (Adam) introduced by the regularization and from the bound M over the $||\cdot||_1$ constraint (TOBS) are analyzed by solving a set of variants of (case I) with different source/receiver positioning as shown in Figure 5.7. All cases begin the inversion with an homogeneous acoustic velocity corresponding to the background value of $v_p = 1$ km/s. Most parameters are the same as those shown in Tables 5.1 and 5.2, with the exception of the maximum number of
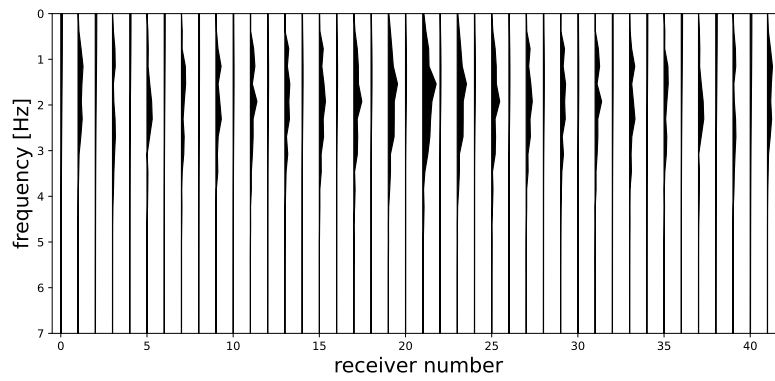
Figure 5.6 − Normalized signal in the frequency domain.

iterations allowed being set to $N_{max} = 200$, 1-norm constraint M and number of sources and receivers that now vary.
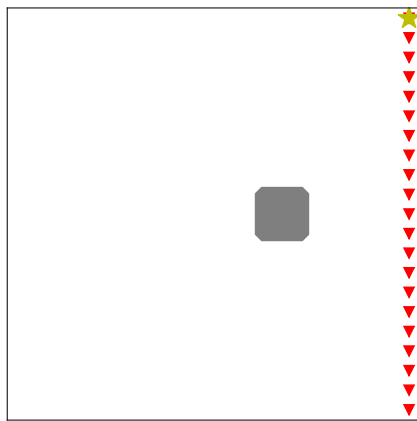
(a) case I.(i).
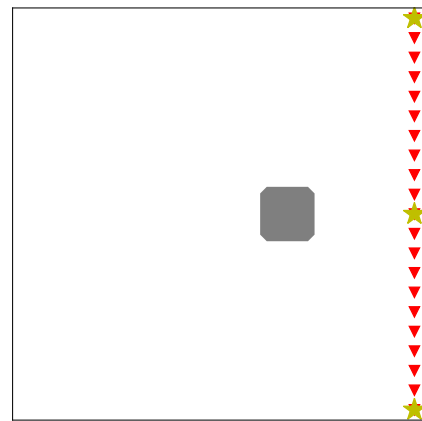
(b) case I.(ii).
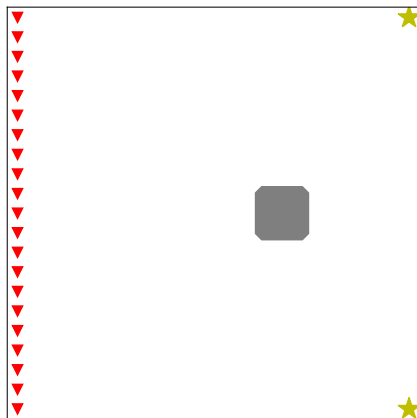
(c) case I.(iii).
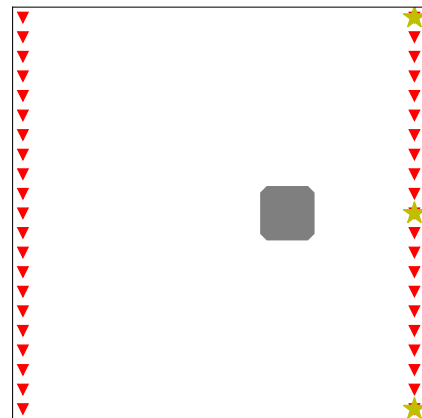
(d) case I.(iv).

Figure 5.7 − Source/Receiver configurations considered.

For each of these configurations, the following combination of parameters is considered:

- $r \in \{0.1, 0.2, 0.3, 0.4, 0.7, 1.0\}$,

- $\gamma_m, \gamma_v \in \{0.5, 0.9, 0.99, 0.999, 0.9999\}$,

- $M \in \{0.001, 0.005, 0.01, 0.02, 0.04\}$,

In total, 112 distinct cases are analyzed, with $\gamma_v = \gamma_m$ in all instances. Results are shown from Figures 5.8 to 5.11.

The symbols in the scatter plots are related to the optimization parameters used as indicated in the labels. The symbol shape indicates the Adam-based weighting parameters γ_m, γ_v. The area of each symbol is proportional to the filtering radius r from the spatial filter. The size of the 1-norm constraint is indicated by the colorbar to the right, so cooler colors indicate tight constraints and warmer colors correspond to more lenient values. The vertical axis shows the objective function values normalized by the value of the first iteration, while the dahsed line simply indicates the initial unitary value. The horizontal axis corresponds to the quality measure, defined as:

$$Q = \sqrt{|v_p(a) - \bar{v}_p|^2 d\Omega}, \tag{5.1}$$

where v_p is the acoustic velocity recovered from the inversion and $\bar{v}_p$ is the reference acoustic velocity field. Hence, smaller values of Q indicate better agreement with the true model.

In case I.(i) (Figure 5.8), very few simulation were able to considerably reduce the values of the objective function. This case can be regarded as the hardest one to image, since a single source is used in the acquisition scheme. The successful configurations have large damping weights ($\gamma \geq 0.999$), while the bound M is still the lowest one considered.

Case I.(ii) had an improved acquisition, with two extra sources with respect to case I.(i). It can be noted from Figure 5.9 that a larger number of cases were able to considerably reduce the objective function while also achieving a smaller quality measure. It can also be noted that large filtering radius r are mostly associated with a low quality measure.

Case I.(iii) had an acquisition associated with wave transmission instead of reflection, since sources and receivers are located at opposing ends. Similarly to case I.(ii), larger filtering radius result mostly in early stopping of the optimization process. The most striking differences with respect to the former examples is that only a mild damping weight of $\gamma = 0.9$ is able to reduce the objective function while also maintaining a low quality measure, and also that the associated $M = 0.04$ is in the mid range of the bound constraints considered. Interestingly, some configurations resulted in reductions larger than one order of magnitude in the objective function, although with a poor quality measure.

Case I.(iv) was the case with most favorable acquisition, having receivers positioned at both ends. This fact is reflected in Figure 5.11, where many configurations were able to significantly reduce the initial value of the objective function and also keep low quality measure values. It can be seen that lower values of M achieved the greatest reductions,
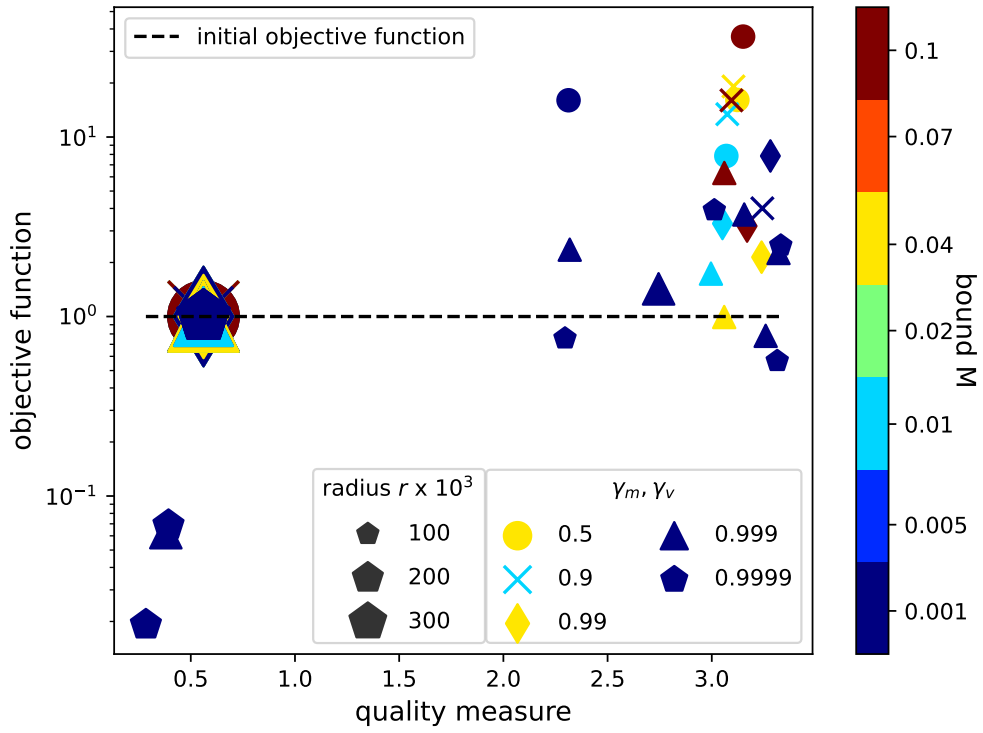
Figure 5.8 − Sweeping for case I.(i).
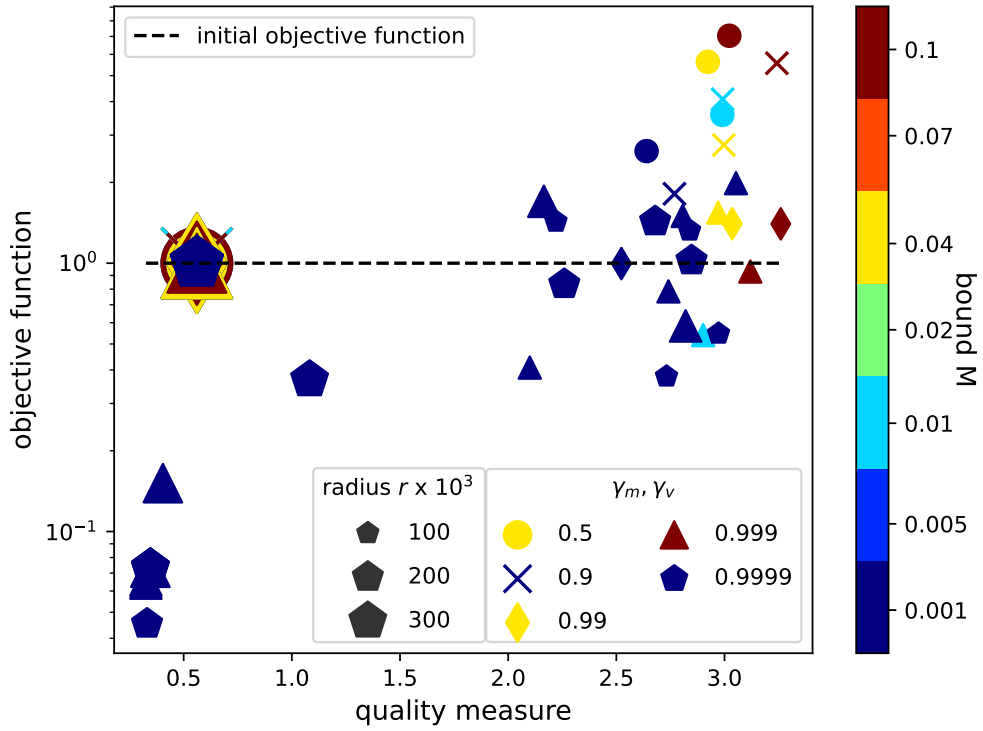
Figure 5.9 − Sweeping for case I.(ii).
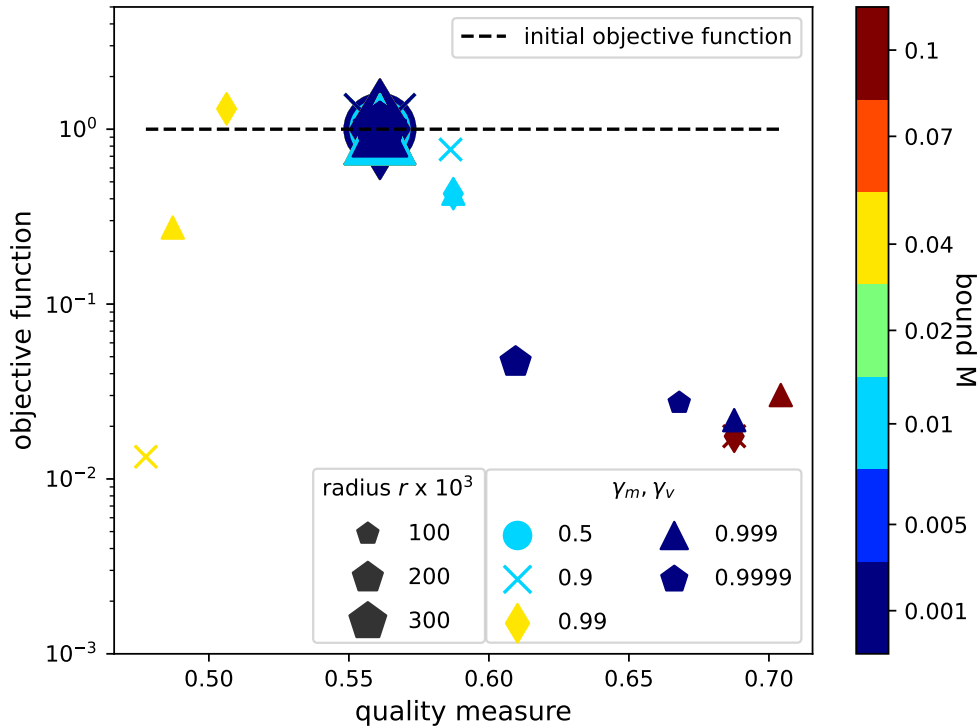
Figure 5.10 − Sweeping for case I.(iii).

Quality measure Q

	ILP	LS
Case I.(i)	0.3030	0.4357
Case I.(ii)	0.3296	0.2946
Case I.(iii)	0.4756	0.6863
Case I.(iv)	1.26×10^{-17}	1.33×10^{-17}

Table 5.3 − Quality measures for case I both with Integer Linear Programming and Level Set.

while all configurations below the threshold of 1×10^{-4} had a damping weight γ larger than 0.999.

The best results obtained for each case are compared qualitatively to those of Lanznaster et al. (2021) as shown in Fig 5.12. For both methods results are dependent of the acquisition configuration. In general the models obtained with Integer Linear Programming are at least capable of identifying location and approximating the shape of the obstacle, although delineation of the boundary not facing the receptors is still faulty as can be seen in Figures 5.12a, 5.12b. In particular, for case I.(iii) (Figure 5.12c) the ILP approach located more precisely the inclusion in comparison to the Level Set result. The optimization for the receiver abundant case I.(iv) was fairly successfully in both cases, although ILP lead to a closer fitting of interfaces.

In Table 5.3 the quality measure Q for both approaches is compared. By that criterion ILP is better in cases I.(i) and I.(iii), while LS is slightly better for case I.(ii). In the well iluminated case I.(iv) both approaches recover the target model up to machine precision.
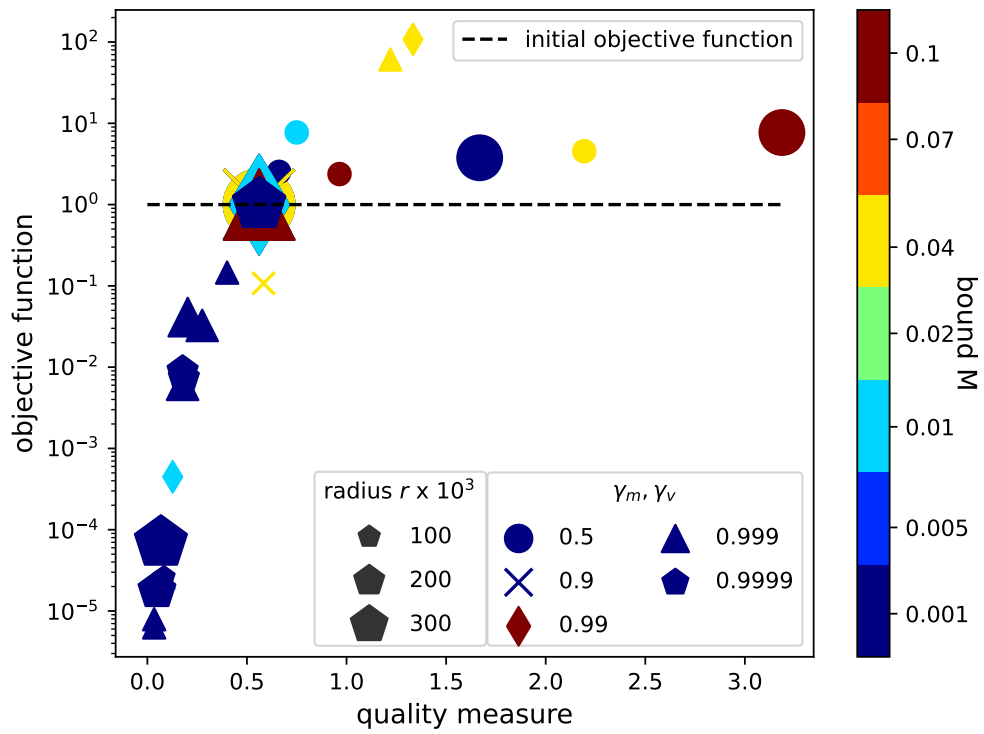
Figure 5.11 − Sweeping for case I.(iv).

(a) case I.(i).

(b) case I.(ii).

(c) case I.(iii).

(d) case I.(iv).
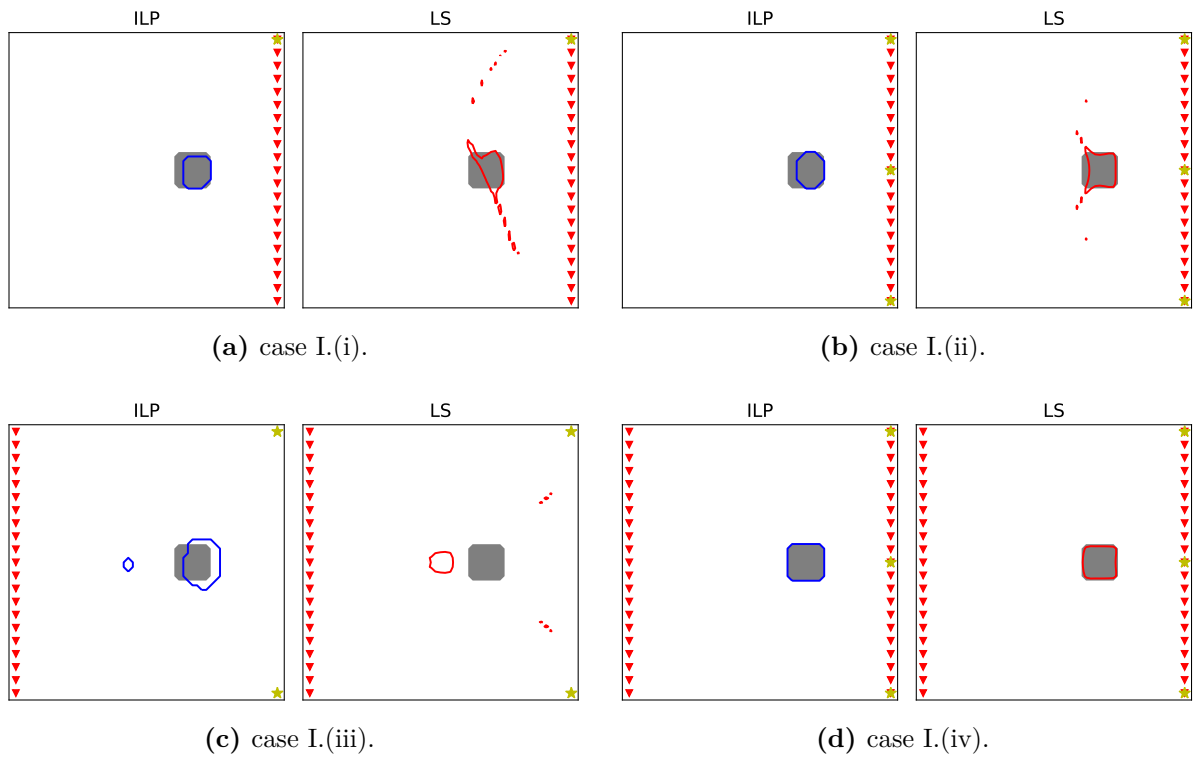
Figure 5.12 − Comparisons of results obtained by Integer Linear Programming (ILP) and those obtained through Level Set (LS).

Inversion parameters	
Maximum number of iterations N_{max}	200
objective function threshold τ_J	1×10^{-16}
gradient threshold τ_G	1×10^{-14}

Table 5.4 − Inversion parameters used in case II.

5.1.4 Two inclusions

The current numerical example explores the velocity model shown in Figure 5.13, and was also taken from Lanznaster et al. (2021). In order to investigate the effectiveness of the ILP approach, five different geometry acquisitions are used, and their results are compared to those obtained in the reference from the literature. The configurations are shown in Figure 5.14, and are refered to collectively as case II.

The problem parameters are the same as those in Table 5.1, with obvious exception to the number of sources and receivers, which vary according to the configuration. Inversion parameters are shown in Table 5.4. The domain is once again discretized with a uniform triangular mesh of 14400 elements and timestep $\Delta t = 0.001s$. The same mesh is used for creating the reference data and executing the forward problem during the inversion. A homogeneous velocity model with the background velocity $v_p = 1$ km/s is used as initial guess.
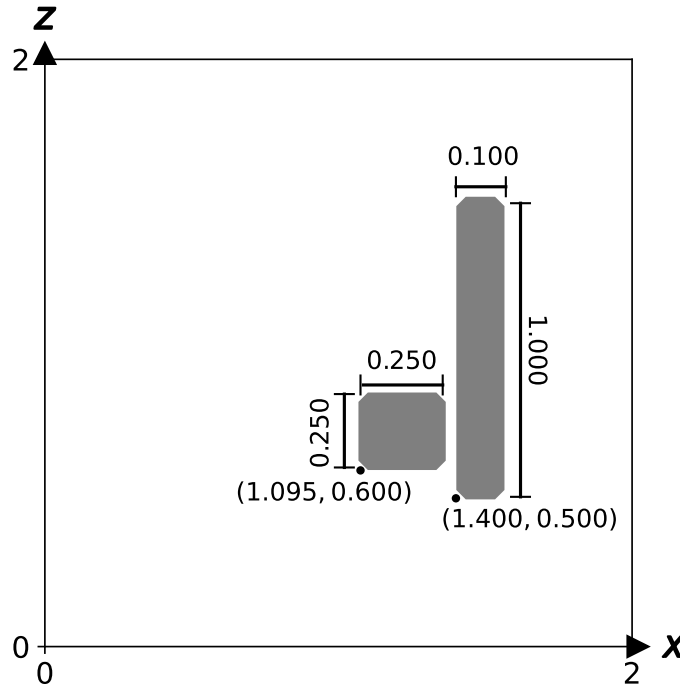
Figure 5.13 − Example with two inclusions.

A sweeping exploration of the inversion parameters γ_m, γ_v, r and M is carried out, similarly to Section 5.1.3. All configurations are optimized for r values between 0.1 and 0.4, γ_m, γ_v between 0.99 and 0.9999, and M bounds ranging from 0.0001 up to 0.05.

(a) case (i).   **(b)** case (ii).

(c) case (iii).   **(d)** case (iv).   **(e)** case (v).
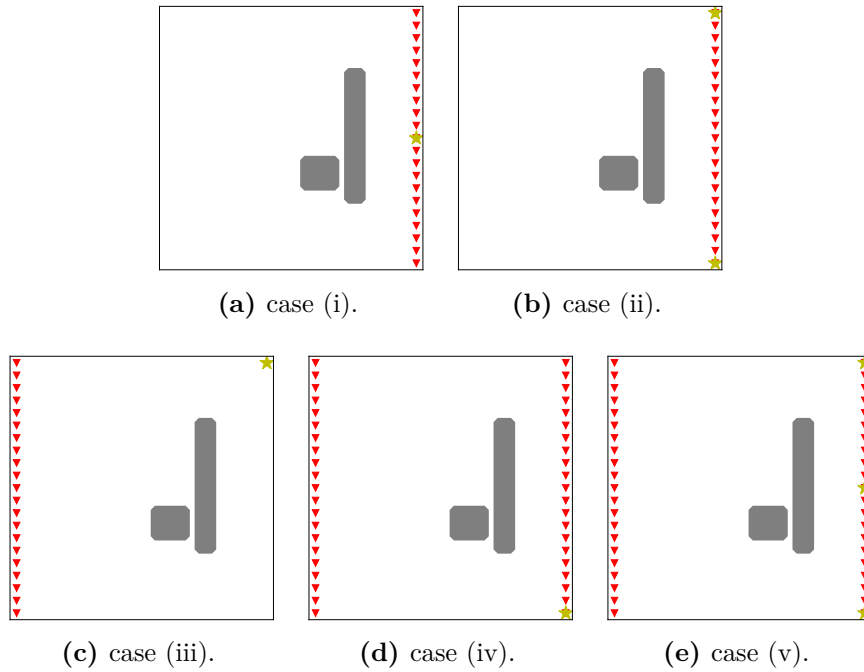
Figure 5.14 − Source/Receiver configurations considered.

The best results for each configuration are shown next to level set results in Figure 5.15.

Once again, result quality depends on configuration. ILP for cases II.(i) and II.(ii) in Figures 5.15a and 5.15b,respectively, struggled with identifying the smaller square inclusion, which is partially obstructed by the bigger rectangular inclusion with respect to the receivers. This created a pattern where, instead of finding small floating islands as of the LS method, ILP lead to the proliferation of spurious inclusion either "behind" or next to the identified rectangular obstacle. Case II.(iii) was poorly identified in both methods. The more favorable case II.(iv) led to partial identification with both methodologies. In particular, while ILP captured more of the obstructed square inclusion, it also lead to spurious inclusions in the upper region of the domain. As for case II.(v), it can be seen that both methods had a very close fit for the rectangular inclusion, and while Level Set missed the fit slightly on the top region, ILP overestimated its size near the square inclusion. For the smaller inclusion, while ILP in general overestimated its size, Level Set underestimated its location, while creating a small spurious inclusion even for the case with most sources and receivers.

A quantitative comparison can be made using the measure Q (Eq. (5.1)). Table 5.5 shows the quality measure obtained with the ILP and the LS method. It can be seen that the proliferation of spurious inclusion for cases II.(i) and II.(ii) led the ILP approach to considerably worse Q values when compared to the LS results. For case II.(iii) the inversion results are similarly bad in terms of the quality measure. The LS method obtained slightly better values for cases II.(iv) and II.(v), in most part due to spurious inclusions or

(a) case (i).

(b) case (ii).

(c) case (iii).

(d) case (iv).

(e) case (v).
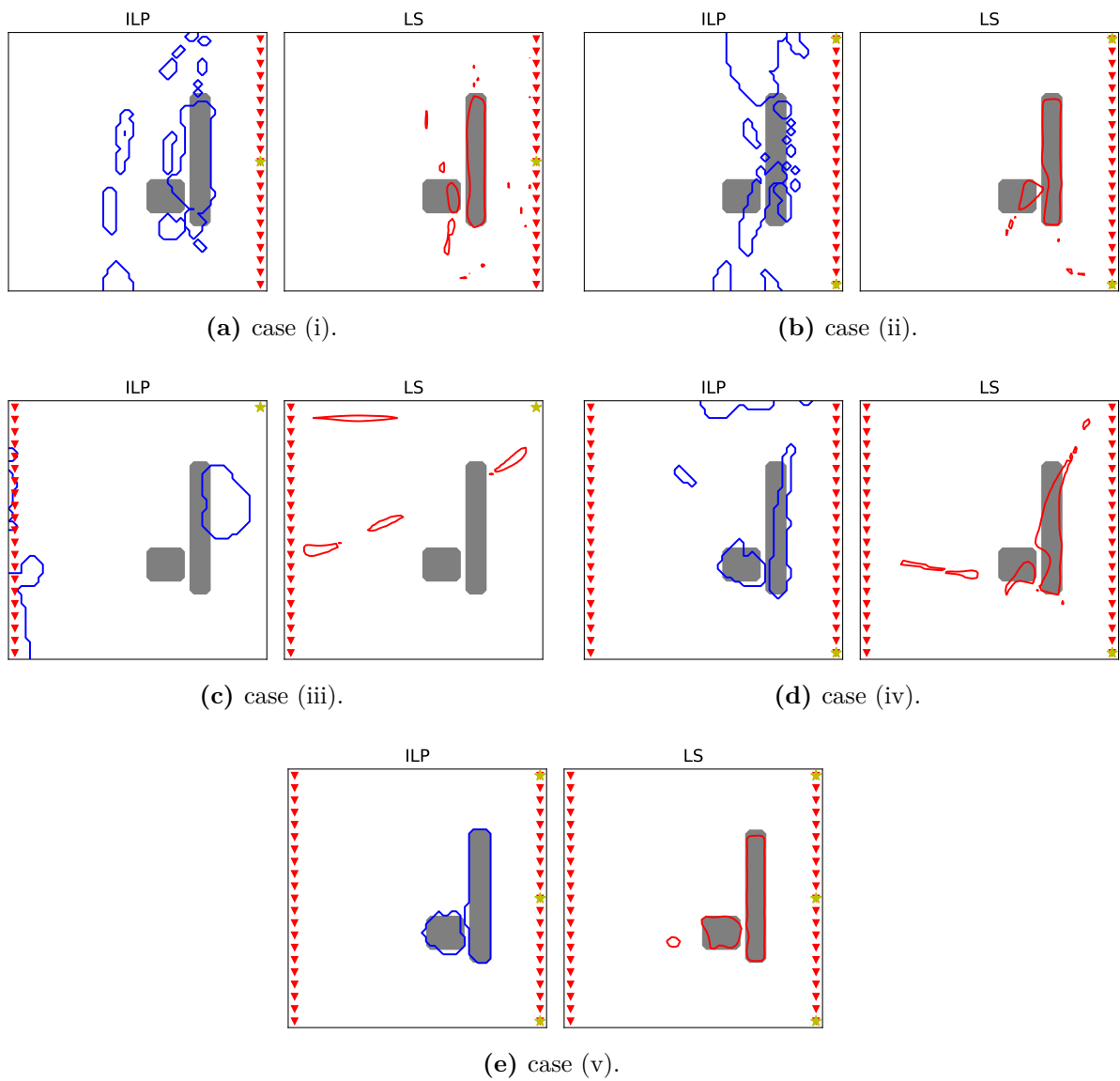
Figure 5.15 − Comparisons of results obtained by Integer Linear Programming (ILP) and those obtained through Level Set (LS).

overestimation of the obstacle boundaries by the ILP approach.

Quality measure Q

	ILP	LS
Case II.(i)	1.1219	0.6356
Case II.(ii)	1.1579	0.5853
Case II.(iii)	1.1579	1.1863
Case II.(iv)	0.9310	0.8172
Case II.(v)	0.3801	0.2887

Table 5.5 − Quality measures for case II both with Integer Linear Programming and Level Set.

(a) Geometry acquisition for case III. **(b)** Inversion result. Q=0.4575993.
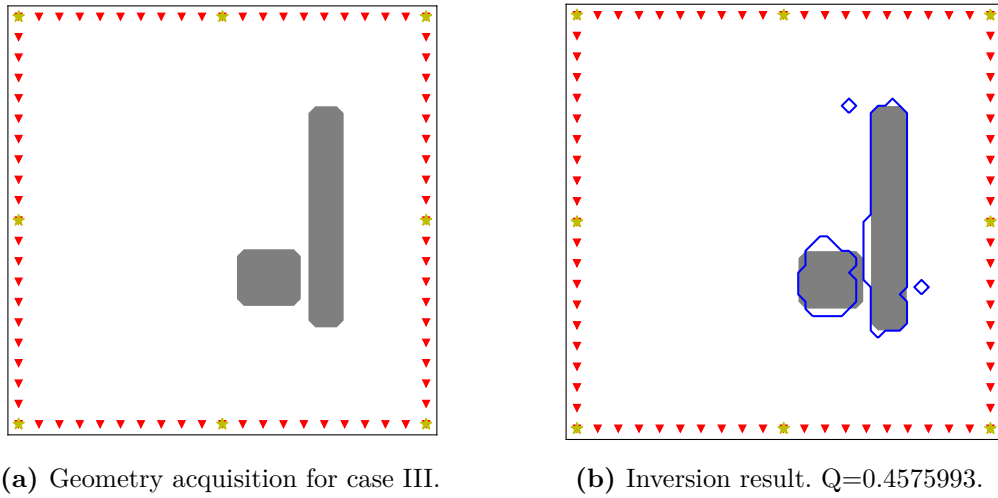
Figure 5.16 − Geometry acquisition and inversion result for case III.

Inversion parameters			
1-norm constraint M	0.005	objective function threshold τ_J	1×10^{-16}
Filtering radius r	0.1	gradient threshold τ_G	1×10^{-14}
Damping weights γ_m, γ_v	0.999	Maximum number of iterations N_{max}	600

Table 5.6 − Inversion parameters used in case III.

5.1.5 Multiscale

In previous sections the acquisition geometry proved to have significant impact over the success of the inversion procedure. In order to focus on the evaluation of the optimization procedure and to minimize the inherent observability problem, a new example with a more favourable setup is considered. The velocity model is the same considered in Section 5.1.4. We refer to this example as case III.

The problem parameters are the same as those in Table 5.1 except for the number of sources and receivers. The geometry acquisition with $N_s = 8$, and $N_r = 80$ is shown in Figure 5.16a. Meshing, timestep size and initial guess choice are the same as in Section 5.1.4. The inversion parameters are shown in Table 5.6.

The inversion result is shown in Figure 5.16b. Despite the better illumination, from Table 5.5 it can be seen that the quality measure Q is worse than case II.(v). In order to evaluate if the linearized nature of the ILP procedure impairs improvements over observability conditions, the experiment is repeated considering a multiscale approach (BUNKS et al., 1995).

In the multiscale approach, instead of considering all frequencies in the data, a bandpass filter is applied so that the inversion procedure only takes into account a certain frequency band at a time. More specifically, a low-pass filter that cuts the higher frequency content of the experimental data is applied, and the cutting frequency is repeatedly raised at every 100 iterations. The cutting frequencies are successively 1Hz, 2Hz, 3Hz, 4Hz, 5HZ
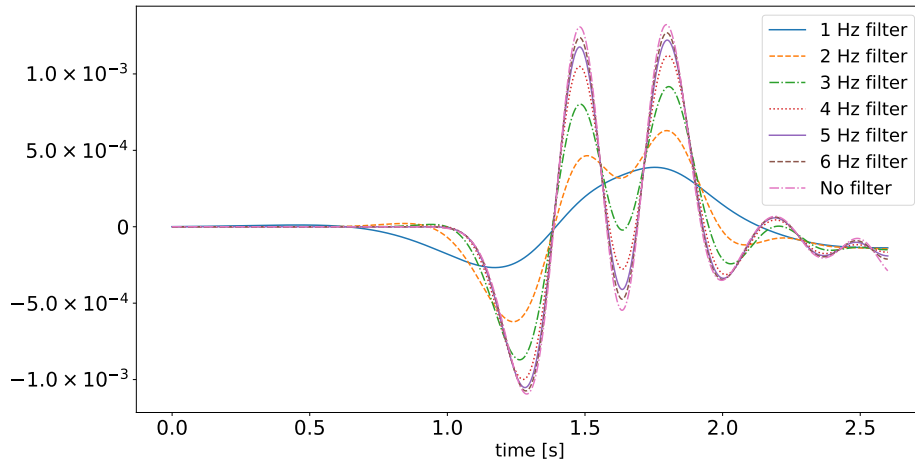
(a) Low-passed signal in the time domain.
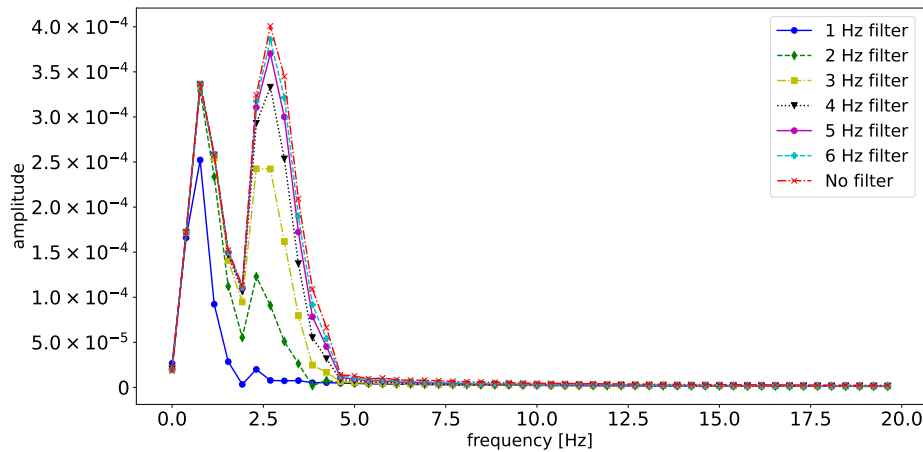
(b) Low-passed signal in the frequency domain.

Figure 5.17 − Reference data generated from source point located at $(1, 1.95)$. Receiver at $(0.145, 0.05)$, source and receiver positioning corresponding to case III.

and 6Hz. The choice of cutting values can be justified by looking at the frequency content of the data. Figure 5.17 shows the filtered signal collected at a single receiver, both in time and frequency. It can be seen that the signal filtered up to 6 Hz is very close to the unfiltered signal, meaning that the whole data frequency range is represented during the optimization.

The results with multiscale are shown in Figure 5.18b. The plots of the evolution history of both the objective function and the quality measure are shown in Figure 5.19.

The velocity model obtained with multiscale is improved, and as can be seen by the plots from Figure 5.19, each successive step where the cutting frequency is increased leads to lower levels for both misfit and quality measure. This experiment highlights how, even at favourable observability conditions, particular modelling considerations for the inversion still have a considerable impact over the quality of results.
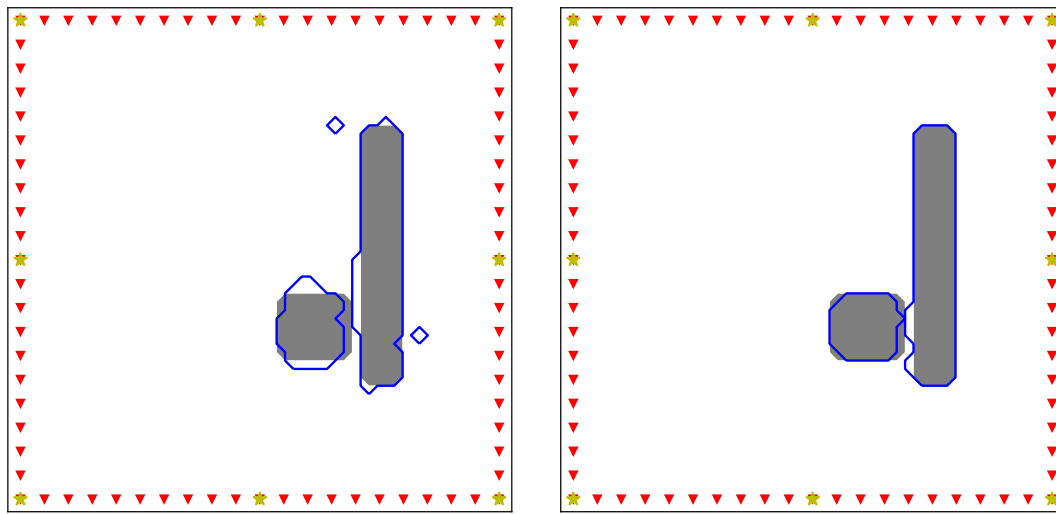
(a) Inversion result without multiscale.　　　**(b)** Inversion result with multiscale.

Figure 5.18 − Case III: Inversion result with and without multiscale.
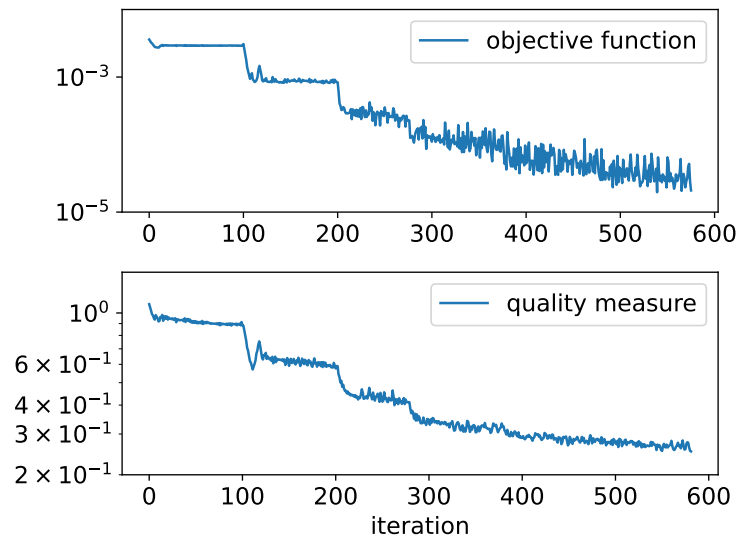
Figure 5.19 − Evolution of objective function and quality measure for case III.

5.1.5.1 Multiscale without inverse crime

All examples shown so far were tested under "inverse crime" conditions, that is, the same forward operator was employed both for generating the reference data and for performing the inversion procedure. This is deemed problematic for inverse problems, and methods for either generating the data with a different method or adding noise to it are warranted (COLTON; KRESS; KRESS, 1998).

In the multiscale case, we change the forward operator by changing the discretization of the mesh used for generating the data, now with 28800 elements. Apart from that, case III is repeated with exactly the same problem and inversion parameters.

Figure 5.20 shows the inversion results when inverse crime is taken into account, both
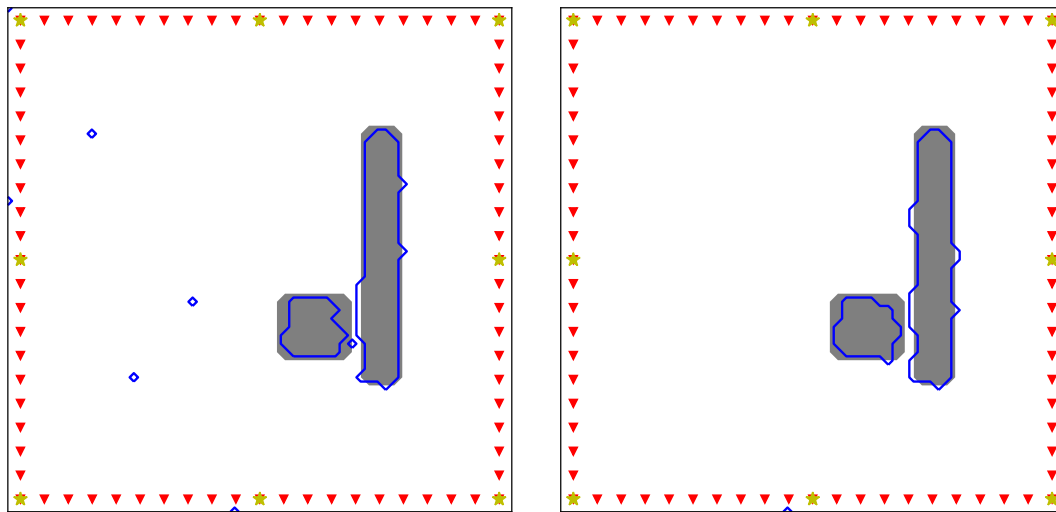
(a) Inversion result without multiscale (no inverse crime).

(b) Inversion result with multiscale (no inverse crime).

Figure 5.20 − Case III: Inversion result with and without multiscale, no inverse crime.

with and without multiscale. Shape innacuracies appear in both cases, however, when the multiscale approach is not used the result also contains small spurious inclusions. Figure 5.21 shows the evolution of the quality measure and objective function. Contrasting it with the results with inverse crime (Figure 5.19) it can be seen that the objective function achieves a considerably higher final value, nevertheless, the measure Q behaves similarly in both cases. Table 5.7 aggregates the quality measure for case III with and without multiscale, taking the inverse crime into account or ignoring it.
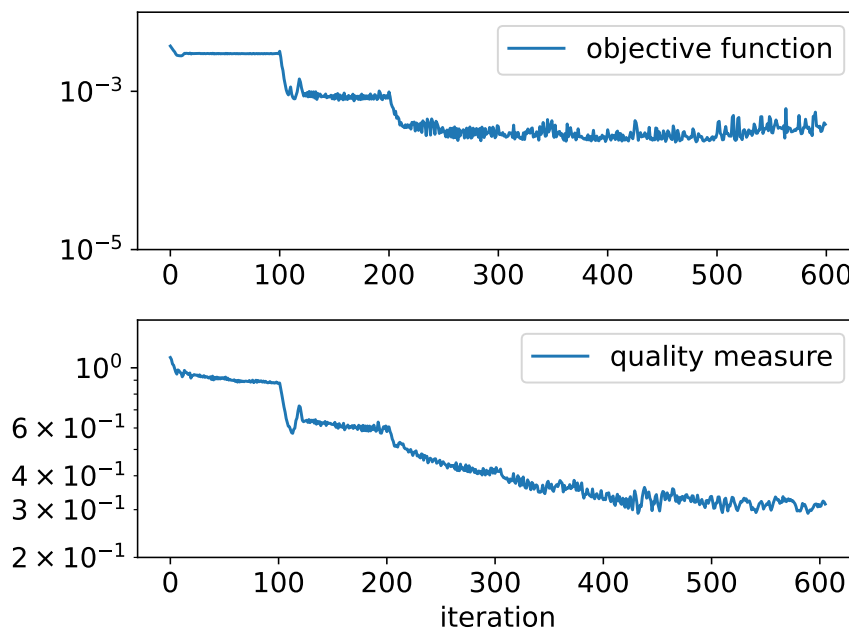
Figure 5.21 − Evolution of objective function and quality measure for the continuation in frequency case without inverse crime.

Quality measure Q

	without multiscale	with multiscale
with inverse crime	0.4575993	0.2819640
without inverse crime	0.3048622	0.2306276

Table 5.7 − Quality measures for case III.

5.1.6 3D example

All examples studied so far are two-dimensional. Albeit this formulation is relevant in many instances, several complex applications in medical imaging (LUCKA et al., 2021), NDT (AFANASIEV et al., 2019) and FWI are intrinsically three-dimensional. A few sharp-interface methods, cut element Level Set (ANDREASEN; ELINGAARD; AAGE, 2020) for instance, introduce ambiguities in boundary definition when translated from 2D to 3D. It is therefore important to investigate whether any complication appears when space dimensionality is increased. Towards this objective of establishing the ILP optimization framework as robust and versatile, a three dimensional case is solved. No conceptual change or special consideration is needed for applying the proposed optimization procedure in a setting with an extra space dimension. Indeed, the main challenge associated with this generalization is the computational cost of simulating 3D wave propagation. With respect to inverse crime, three scenarios are considered

- commit inverse crime by generating reference data and performing the inversion with the same operator.

- avoid inverse crime by generating reference data with a finer mesh.

- avoid inverse crime by generating reference data with higher order elements.

The velocity model considered can be seen in Figure 5.22. It consists of a cubic domain of side 1 km with homogeneous background acoustic velocity of 2 km/s, and a spherical inclusion with velocity of 3 km/s. In all three scenarios the initial guess is a velocity model consisting only of the 2 km/s acoustic velocity background and no inclusion. We refer to this example as case IV.

The acquisition geometry consists of $N_s = 9$ sources distributed regularly over one surface, and of and $N_r = 2601$ receivers regularly placed at the opposite side, as depicted in Figure 5.23. Both sources and receivers are at a distance of 20m from the closest surface. A transmission setup (with sources and receivers at opposing ends) with a large number of receivers was chosen in order to guarantee a well illuminated problem. The problem parameters describing geometry acquisition, velocity model and source signal are summarized in Table 5.8, while the inversion parameters related to the filters, update procedure and stopping criteria are displayed in Table 5.9.
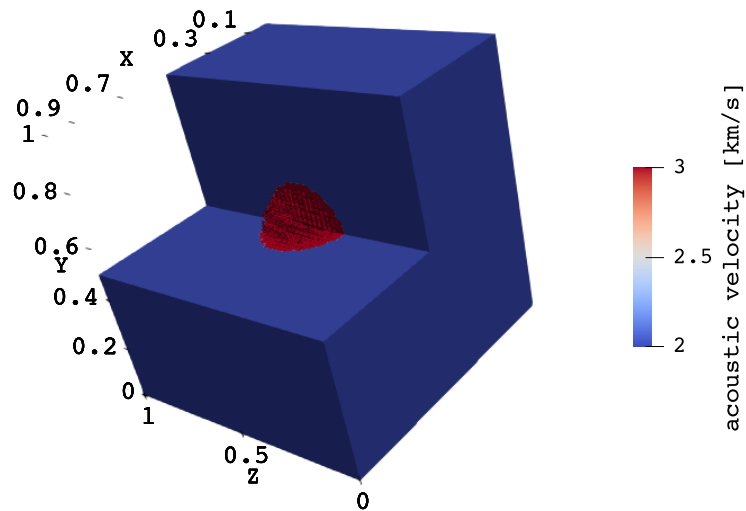
Figure 5.22 − Reference model for three dimensional case.
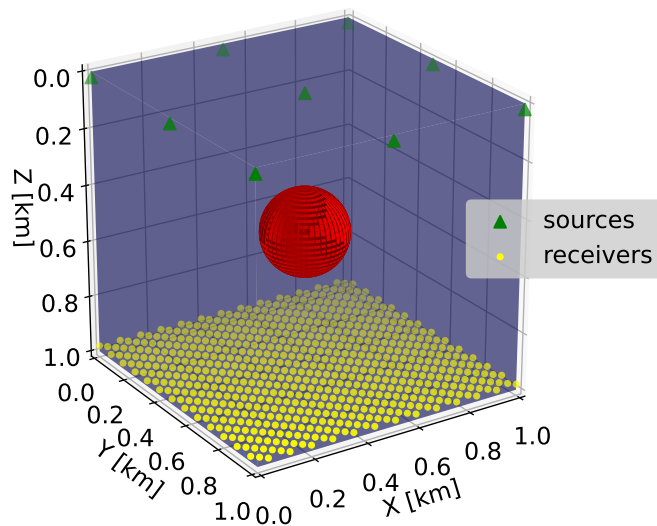
Figure 5.23 − Placement of sources and receivers for the 3D case.

A time step size of $\Delta t = 0.001$ s is employed, while the space discretization uses linear polynomials over a tetrahedral mesh with 750000 elements.

Snapshots of the velocity model together with the final result are shown in Figure 5.24. The evolution of the objective function and quality measure can be seen in Figure 5.25. While both of these measure increase in the first iteration of the inversion, Figure 5.24a shows that the central inclusion is correctly located. Indeed, Figure 5.24b indicates that at the 5th iteration the recovered model already matches the true model quite closely. During the rest of the optimization procedure, objective function and quality measure decrease orders of magnitude as recovered body and true body come to almost coincide (Figure 5.24d).

Similarly to Section 5.1.5.1, the impact of adding perturbations to the reference data

Problem parameters			
background velocity	2 km/s	Number of sources N_s	9
inclusion velocity	3 km/s	Number of receivers N_r	42
length	1 km	source distance from surface	0.02 km
depth	1 km	receiver distance from surface	0.02 km
width	1 km	source offset	0.5 km
source central frequency	4 Hz	receiver offset	0.02 km
event duration	2.0 s		

Table 5.8 − Parameters that describe the inversion problem case IV.

Inversion parameters			
1-norm constraint M	0.1	objective function threshold τ_J	1×10^{-16}
Filtering radius r	0.1	gradient threshold τ_G	1×10^{-14}
Damping weights γ_m, γ_v	0.999	Maximum number of iterations N_{max}	100

Table 5.9 − Inversion parameters used in case IV.

(a) 1st iteration.

(b) 5st iteration.

(c) 15st iteration.

(d) Result(54 iterations).
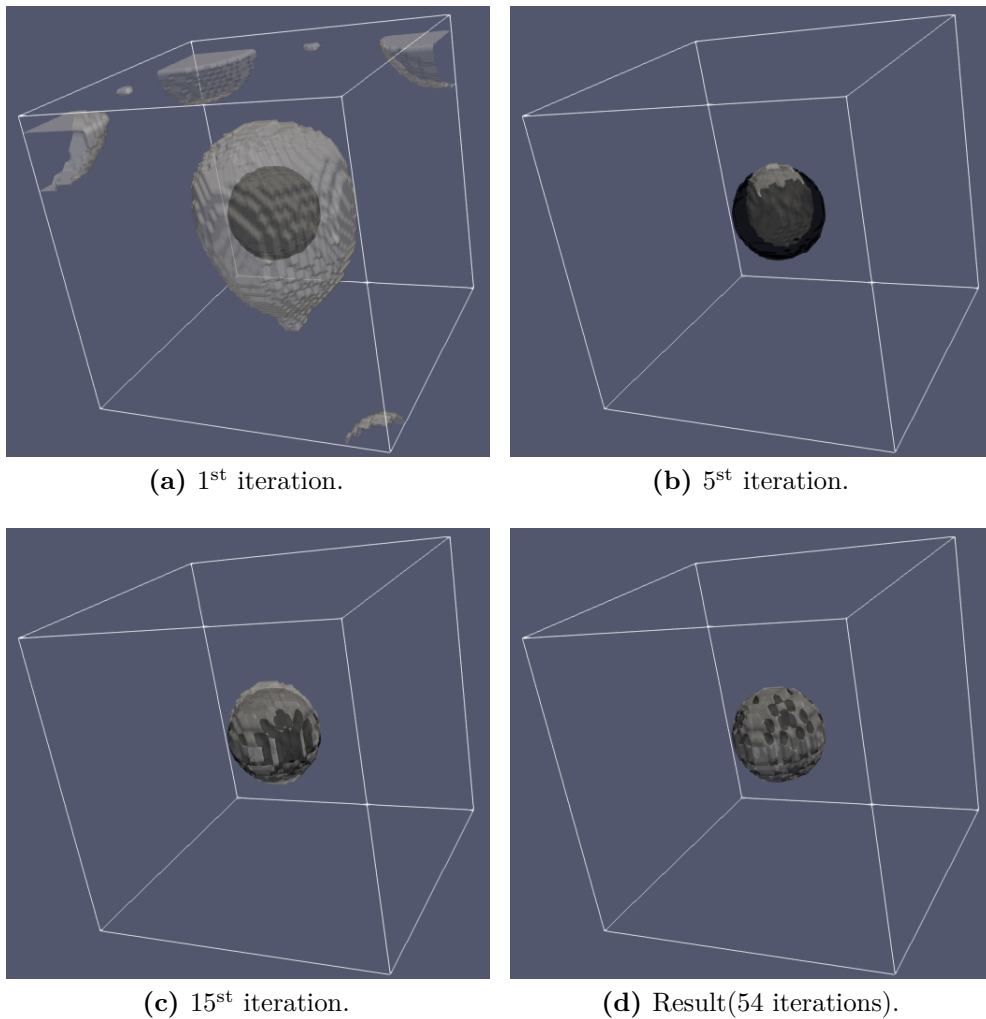
Figure 5.24 − Results for 3D case with inverse crime.

in order to avoid the inverse crime is assessed for the 3D case. In this example, however, in addition to using different meshes for data generation and inversion, a strategy employing
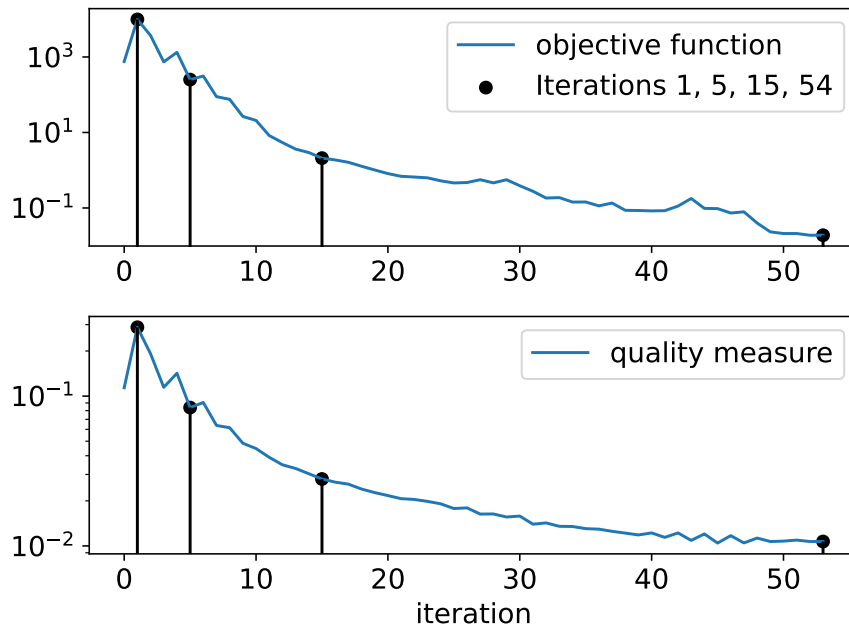
Figure 5.25 − Objective function and quality measure for 3D case.

higher order element for creating the reference data was also employed. All parameters from tables 5.8 and 5.9 were kept the same, except for the 1-norm constraint, which had to be reduced to $M = 0.005$.

The mesh used to generate the new reference results consisted of 6 million regular tetrahedral linear elements, while the mesh used for the inversion was the same as before. Figure 5.26 shows that the spherical inclusion was recovered, albeit also with the appearance of spurious artifact near the surface where the sources are located. Figure 5.27 show the objective function and quality measure now decreasing considerably less. The lower bound for both values is most likely due to the spurious artifacts, making these two measures less meaningfull regarding the ability of the procedure in recovering the central body, successful in this instance.

In the alternative method of avoiding the inverse crime the mesh still has 750000 elements, however, while the problem for running the forward problem during the inversion uses linear elements and has 132641 Degrees of Freedom (DoF), second order elements result in a model with 3295301 DoF for generating the reference data. The inversion results from Figure 5.28 show patterns similar to those in Figure 5.24. Although artifacts appear in the final result as well, they are more spread out, and not as concentrated near the sources. The evolution of the objective function and quality measure in Figure 5.29 show the same behaviour as that of Figure 5.27.

(a) 4st iteration.

(b) 10st iteration.

(c) 24st iteration.

(d) Result(100 iterations).
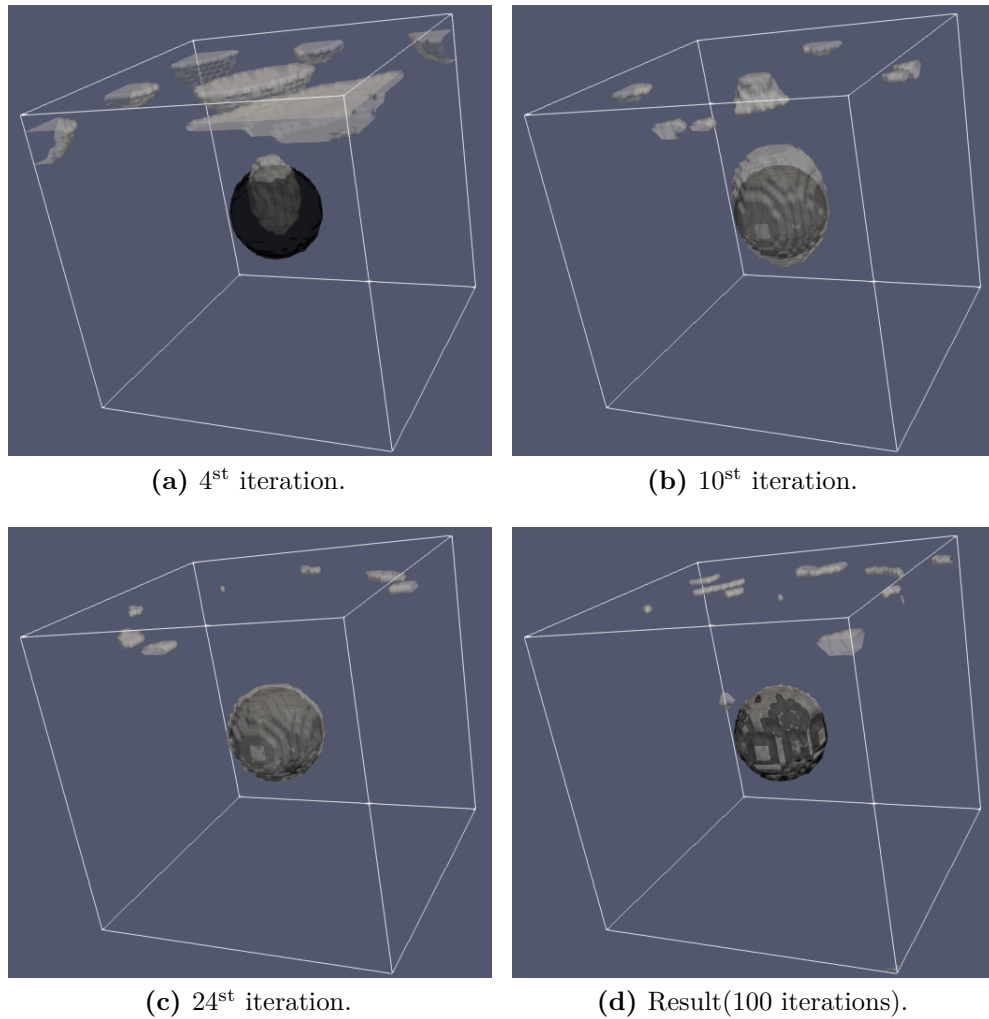
Figure 5.26 − Results for 3D case without inverse crime (different meshes).

5.2 Full Waveform Inversion

In this section, two Full Waveform Inversion cases are considered. Although FWI is an application of acoustic inversion, the following examples are qualitatively different from those in Section 5.1 with regards to the boundary conditions. Since in FWI the domain is unbounded, either a transparency condition (Eq. (2.8)) or an absorbing layer (Eq. (2.9)) must be used to attenuate the reflections coming from the boundaries of the computational domain.

5.2.1 Three salt inclusions

The first FWI example is taken from Albuquerque, Laurain e Yousept (2021b), who used a Hamilton-Jacobi based Level Set method. The velocity model consists of three irregular salt inclusions embedded into a homogeneous medium. In particular, the acoustic velocity of the inclusions is representative of salt structures. Furthermore, the rectangular domain consists of a free surface along which sources and receivers are distributed, and three boundaries extended by absorbing layers in order to emulate an infinite medium.
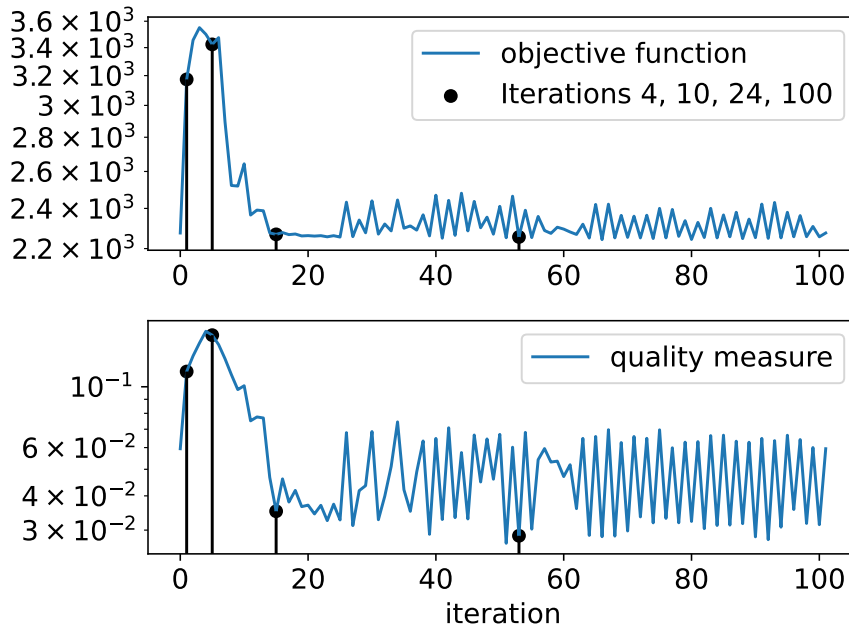
Figure 5.27 − Objective function and quality measure for 3D case avoiding the inverse crime by using different meshes.

Problem parameters			
background velocity	1.95 km/s	Number of sources N_s	10
inclusion velocity	4.12 km/s	Number of receivers N_r	80
length	1 km	source distance from surface	0.05 km
depth	0.65 km	receiver distance from surface	0 km
source central frequency	5 Hz	source offset	0.11 km
event duration	2.0 s	receiver offset	0.0225 km

Table 5.10 − Parameters that describe the inversion problem with salt inclusions.

Velocity model and geometry acquisition are shown in Figure 5.30, while the parameters describing the problem are grouped in Table 5.10. A multiscale approach was employed, with cutting frequency ranging from 2 Hz to 6 Hz by steps of 1 Hz. In order to have a model as close as possible to the original work from the literature, the inverse crime was avoided by adding gaussian noise to the reference signal.

The absorbing layer starts from a distance of 0.1 km from the outer boundary, as displayed in Figure 5.31a. The width was chosen so as to coincide with the referenced work. Figure 5.31b shows that the damping layer η (Equation (2.1)) varies quadraticaly with distance. The profile was adapted from Sochacki et al. (1987). The maximum allowed value of $\eta_{max} = 1$ was defined by inspecting boundary reflections for different η_{max}.

The gaussian noise added to the reference signal has mean equal to zero and standard deviation proportional to the maximum measured amplitude. By denoting the amplitude of the signal at point $\mathbf{x}_r$, instant $t = t_n$ due to an excitation from point $\mathbf{x}_r$ as $d_{r,s,n}$ and

(a) 4$^{\text{st}}$ iteration.

(b) 10$^{\text{st}}$ iteration.

(c) 24$^{\text{st}}$ iteration.

(d) Result(100 iterations).
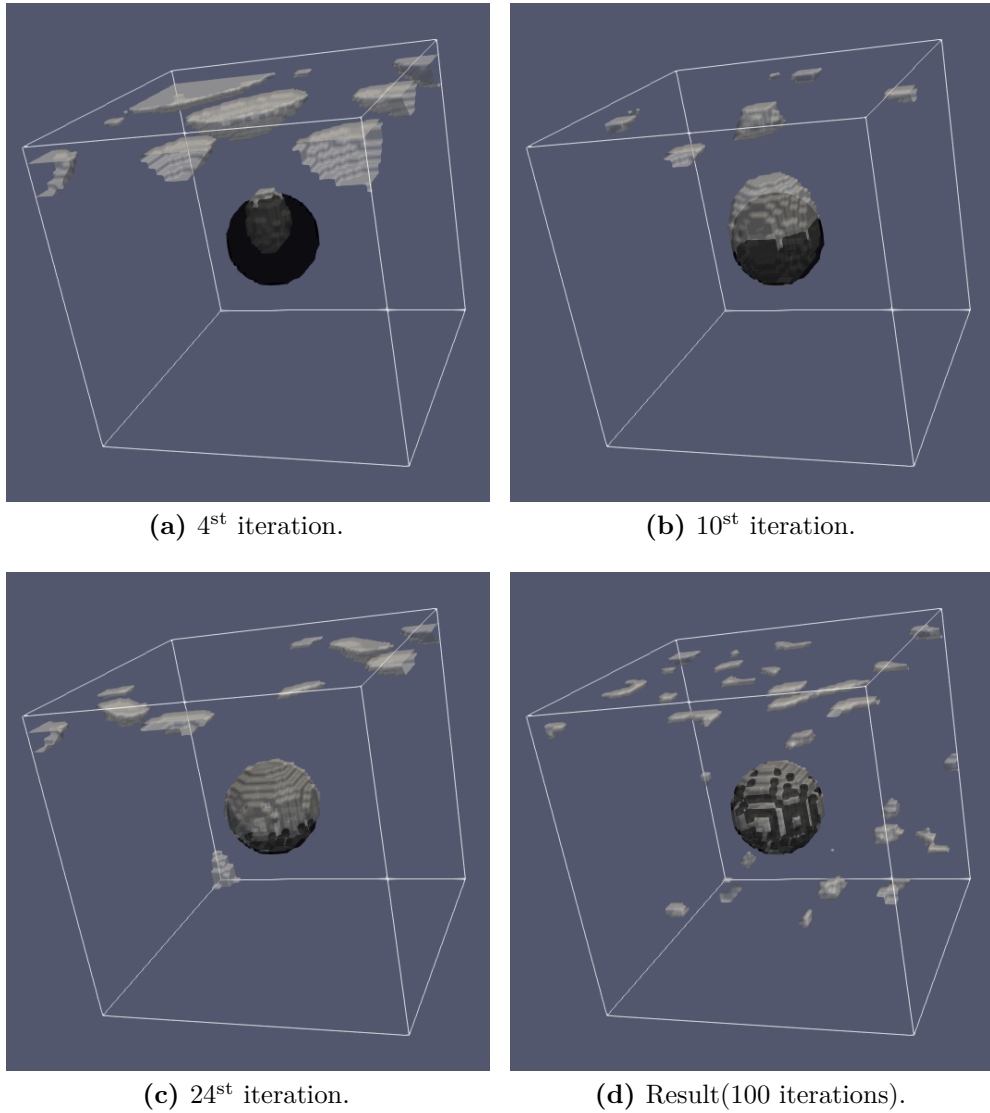
Figure 5.28 − Results for 3D case without inverse crime (different element polynomial order).

the corresponding reference signal as $\bar{d}_{r,s,n}$, the Mean Noise Level (MNL) is written as:

$$\frac{1}{N_s} \sum_{s=1}^{N_s} \frac{\sqrt{\sum_{r=1}^{N_r} \sum_{n=1}^{N_t} |d_{r,s,n} - \bar{d}_{r,s,n}|^2}}{\sqrt{\sum_{r=1}^{N_r} \sum_{n=1}^{N_t} |d_{r,s,n}|^2}} \tag{5.2}$$

The time step used was $\Delta t = 0.000485$ s, while the domain was discretized by a mesh of 52000 triangular elements. Two different initial guess choices were considered, one with a homogeneous background acoustic velocity and no inclusion, and the other with three circular inclusions located closed to the obstacles to be imaged, as was done in (ALBUQUERQUE; LAURAIN; YOUSEPT, 2021b) (see Figure 5.32). The MNL level was 9.57% and 9.56% for the homogeneous and circular inclusion guess, respectively. Inversion parameters are displayed in Table 5.11.

Figure 5.33 show the inversion results. It can be seen that the inclusions were recovered regardless of the initial guess chosen, and that spurious inclusions appeared in both
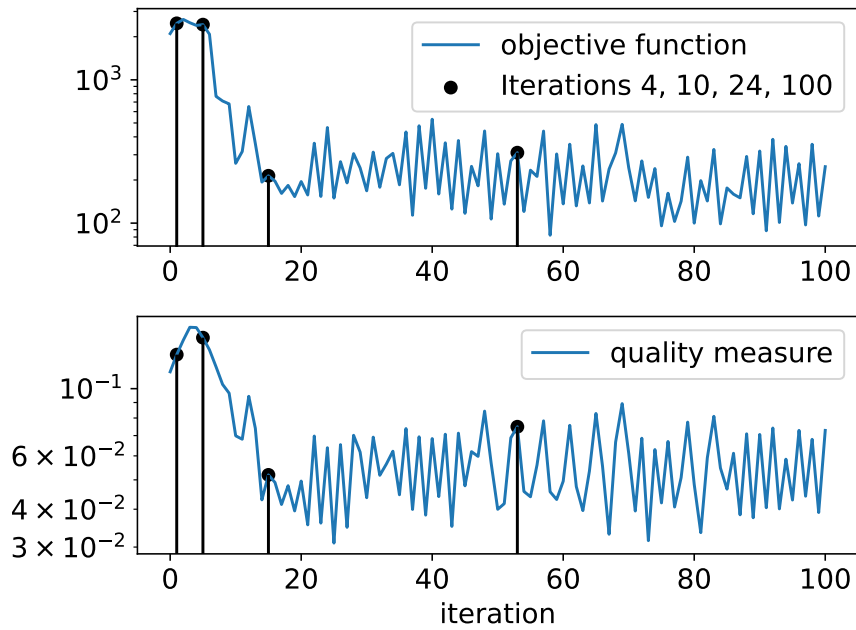
Figure 5.29 − Objective function and quality measure for 3D case avoiding the inverse crime by using different meshes.
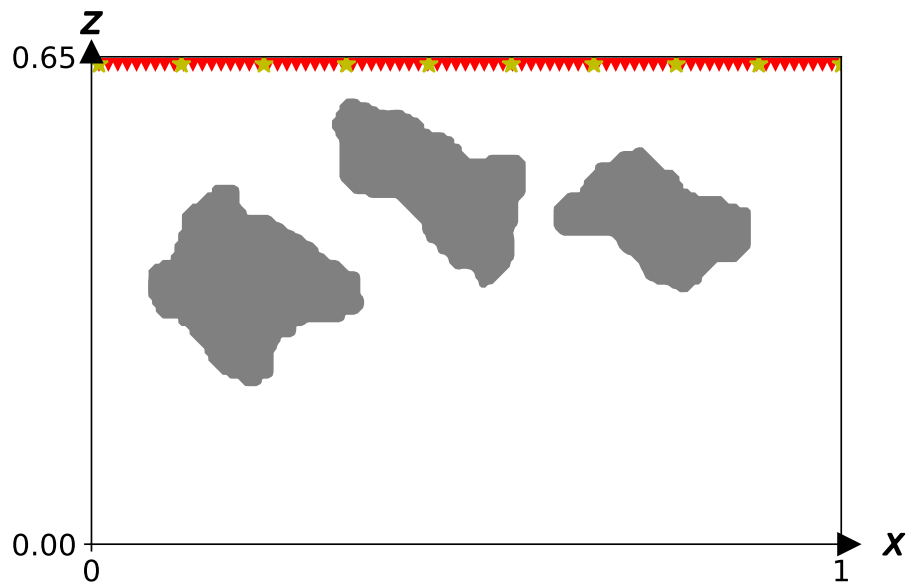
Figure 5.30 − Position of inclusions, domain dimensions and geometry acquisition.

cases. The biggest difference is the boundary pointing "protuberance" in the left most inclusion, which appears only for the homogeneous guess. It can be said that, while the Hamilton-Jacobi based Level Set approach led to more precise results (see Table 5.12), a more favourable initial guess with three circular inclusions was used. The ILP results, although less precise, also correctly placed the inclusions even without prior knowledge of their precise number or location. Hence, there seems to be a compromise where the proposed
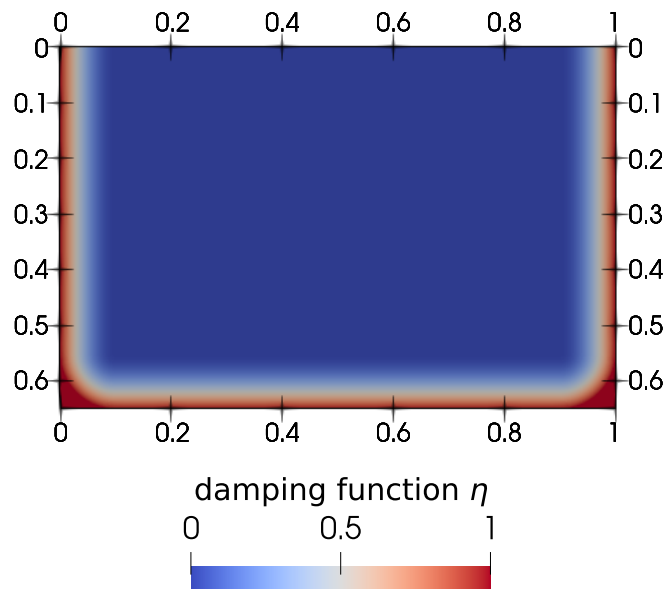
(a) Value of the damping function η.
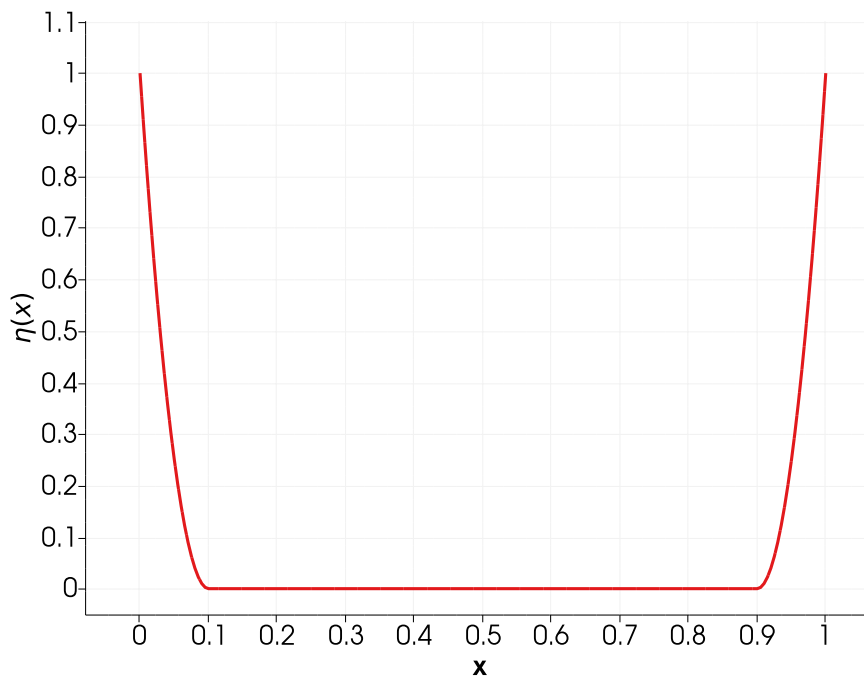
(b) $\eta(x)$ profile at depth $z = 0.325$.

Figure 5.31 − Absorbing boundary layer η. At a distance of 0.1 km from the boundary η grows quadratically from 0 to 1.

methodology yields rougher results, however, it eliminates the need for an initialization guess, which is required in Level Set approaches that utilize the Hamilton-Jacobi equation to control the model's evolution. Hence, these results also suggest a workflow where ILP could be a first step in the reconstruction, with a Hamilton-Jacobi based Level Set approach such as from Albuquerque, Laurain e Yousept (2021b) being used to refine the results obtained.
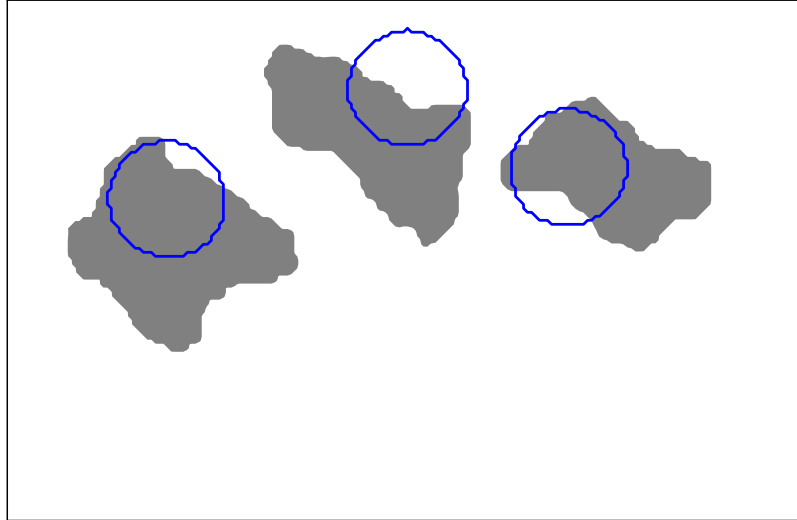
Figure 5.32 – Non-homogeneous initial guess. The number of inclusions is the same as that of the reference model.

Inversion parameters			
1-norm constraint M	0.00175	objective function threshold τ_J	1×10^{-16}
Filtering radius r	0.05	gradient threshold τ_G	1×10^{-14}
Damping weights γ_m, γ_v	0.999	Maximum number of iterations N_{max}	500

Table 5.11 – Inversion parameters used in case with three inclusions.

Quality measure Q	
Level Set, three circular inclusions as initial guess	0.062173
ILP, three circular inclusions as initial guess	0.091188
ILP, homogeneous initial guess	0.099987

Table 5.12 – Quality measures for case with three inclusions.

5.2.2 Sharpness influence

Full-Waveform Inversion (FWI) is known to be more challenging when there is strong contrast in material parameters, as opposed to when they are smoothly varying with small perturbations (KADU; LEEUWEN; MULDER, 2016). In order to assess how our approach handles different contrast levels, the impact of the ratio $v_{p,ratio}$ between the maximum and minimum acoustic velocities $v_{p,max}$ and $v_{p,min}$ was evaluated by simulating the case from Section 5.2.1 with ratios of 1.2, 2.11, 3, 4, 5 and 6. While $v_{p,min}$ was fixed to 1.95 km/s, the inclusion velocity $v_{p,max}$ varied from 2.34 to 11.7 km/s.

All problem and inversion parameters were the same, except for the timestep Δt, which had to be changed for inclusions with higher velocities in order to still satisfy the stability condition. Their values are shown in Table 5.13.

A frequency content analysis is shown in Figure 5.34. Figure 5.34a illustrates the effect
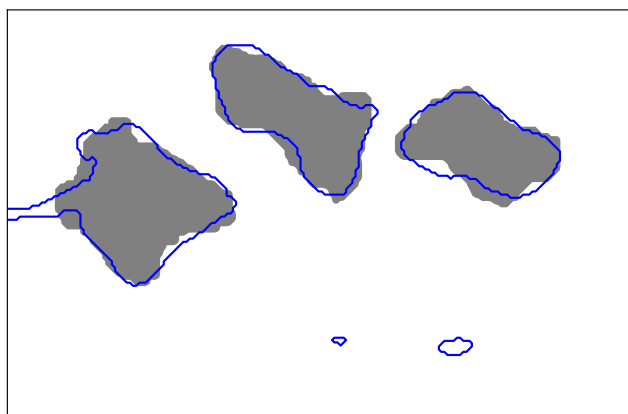
(a) Inversion result for homogeneous initial guess.
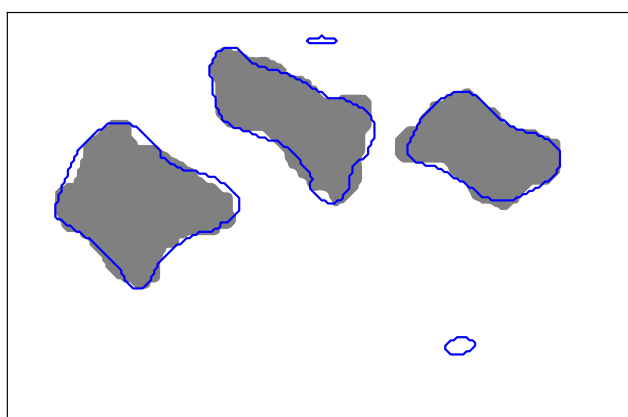
(b) Inversion result for initial guess with three circular inclusions.
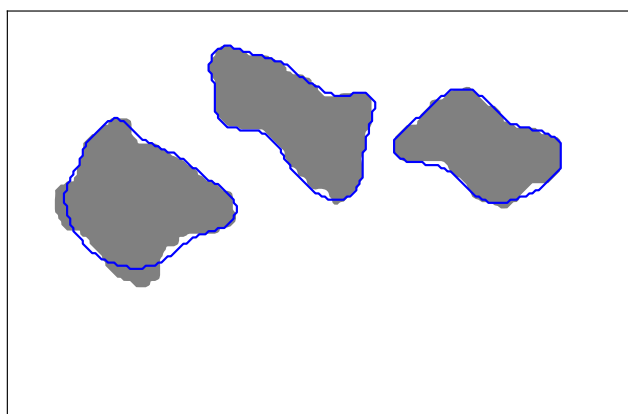
(c) Result obtained through Level Set (ALBUQUERQUE; LAURAIN; YOUSEPT, 2021b).

Figure 5.33 – Figures (a) and (b) show a comparison between inversions with and without circular inclusions as initial guess. Figure (c) shows the result obtained in the referenced article.

vp_{ratio}	time step Δt [s]	maximum time step Δt_{max} [s]
1.2	0.000485	0.002094
2.11	0.000485	0.001214
3	0.000485	0.000868
4	0.000242	0.000651
5	0.000242	0.000521
6	0.000242	0.000434

Table 5.13 − Time step used for each simulation in Section 5.2.2, and the maximum value allowed according to the stability criterion from **??**).

the added noise has over the signal. Figure 5.34b shows the frequency content of the same signals, which are all concentrated around the 5Hz central frequency of the source, with significant contributions up to 10 Hz. As pointed in previous sections, time steps as low as 0.000485 s and 0.000242 s comfortably cover that frequency range.
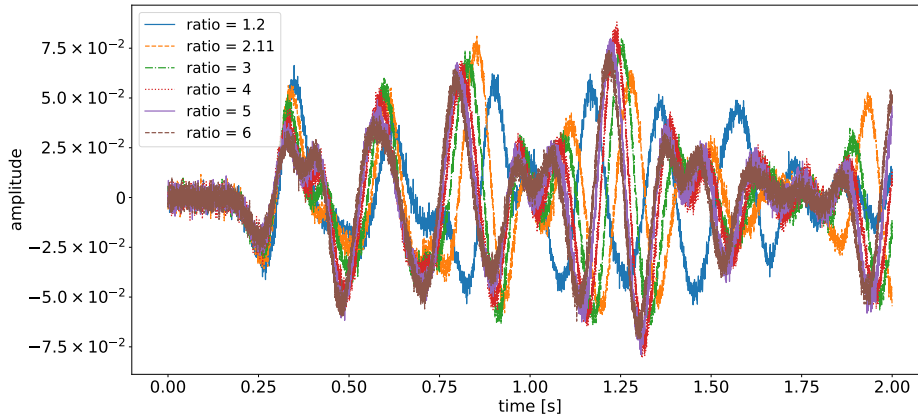
(a) Signal at receiver for different vp_{max}/vp_{min} ratios in the time domain.
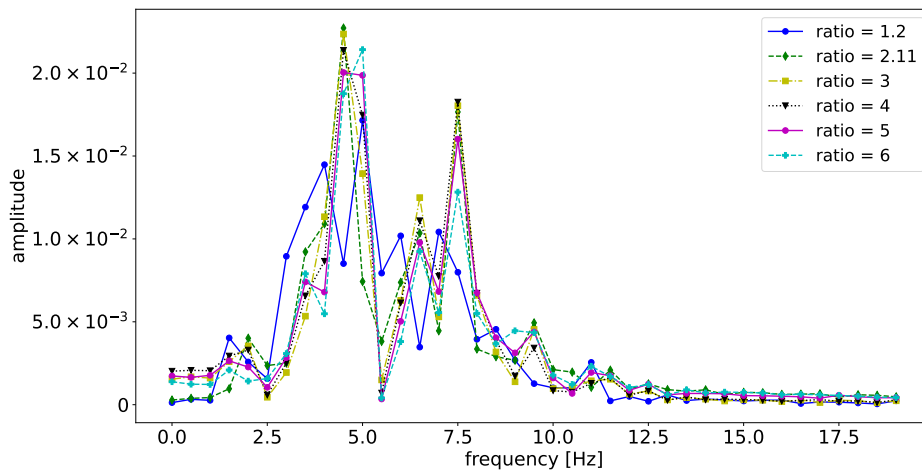
(b) Signal at receiver for different vp_{max}/vp_{min} ratios in the frequency domain.

Figure 5.34 − Reference data generated from source point located at $(0.65, 0.26)$. Receiver at $(0.65, 0.45)$, source and receiver positioning corresponding to case IV.

In table 5.14 the drop in value of the Q measure with respect to its value at the start

$v_{p,ratio}$	1.2	2.11	3	4	5	6
Q/Q_0	51%	61%	59%	26%	55%	47%

Table 5.14 − Drop in value of the Q measure for each $v_{p,ratio}$..

of the inversion procedure Q_0 is shown. It can be seen that, for the most part, all cases had a drop between 47% to 61%, and did not show dependency on the contrast value. The only exception was for $v_{p,ratio} = 4$, which had a drop of only 25%. Inversion results are shown in Figure 5.35, except for $v_{p,ratio} = 2.11$, the case covered in the previous Section. The most prominent feature is that the contrast ratio does not strongly correlate with the quality of the result. The poorer results for $v_{p,ratio} = 4$ (Figure 5.35c) highlight how the acoustic inversion problem is highly dependent on problem characteristics such as source/receiver position, dimensions and, in this case, acoustic velocities.

5.2.3   Santos Basin velocity field

In this section, the problem of inverting an acoustic velocity model representative of the Santos Basin is considered. In particular, the model features a thick salt layer with a thin reservoir underneath, as shown in Figure 5.36. There are five geological units in the model. The seawater, post salt, salt layer, pre salt (reservoir) and basement have corresponding acoustic velocities of 1.5 km/s, 2.5 km/s, 4.5 km/s, 5.5 km/s and 7.0 km/s. The two-dimensional model has 14.5 km in length and depth of 5 km.

In order to fully explore the capability of the proposed method, two geometry acquisitions are used. Figure 5.36a shows a setup with 8 sources placed on the top boundary, and 73 receivers at a depth of 900 meters, which is representative of an Ocean Bottom Node (OBN) seismic survey. Figure 5.36b, on the other hand, displays a reflection-transmission setup which, albeit not realistic, is useful in later analyses. It features an extra row of 73 receivers at a depth of 4.5 km. The parameters describing domain dimensions, source signal, experiment duration and acquisition configuration are summarized in Table 5.15. Furthermore, a transparency condition (Eq A) is imposed on all computational boundaries except the top one in order to emulate a semi infinite medium.

Problem parameters			
Number of sources	8	Number of receivers N_s	73
length	14.5 km	source distance from surface	0 km
depth	5 km	receiver distance from surface	0.9 km
source central frequency	2 Hz	source offset	2.07 km
event duration	5 s	receiver offset	0.199 km

Table 5.15 − Parameters that describe the salt basin inversion problem.

Time was discretized with a timestep of 0.001 seconds, and the domain was discretized with a triangular mesh of 58000 elements for all examples, unless explicitly stated otherwise.

Since the water layer location is given, the gradient information in that region is muted
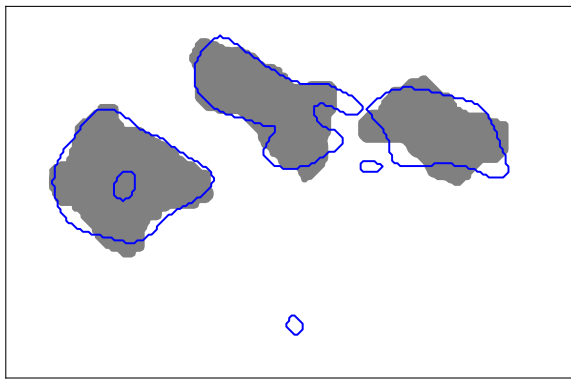
(a) $v_{p,max}/v_{p,min} = 1.2$.
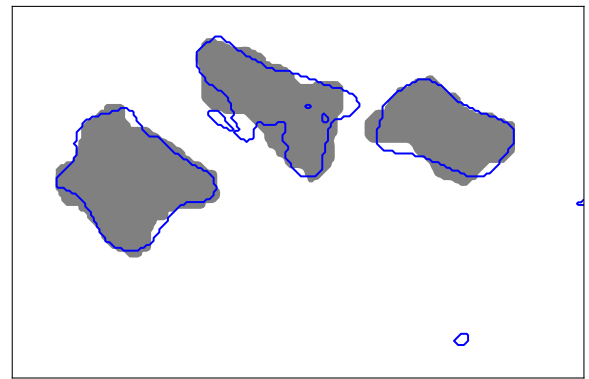
(b) $v_{p,max}/v_{p,min} = 3$.
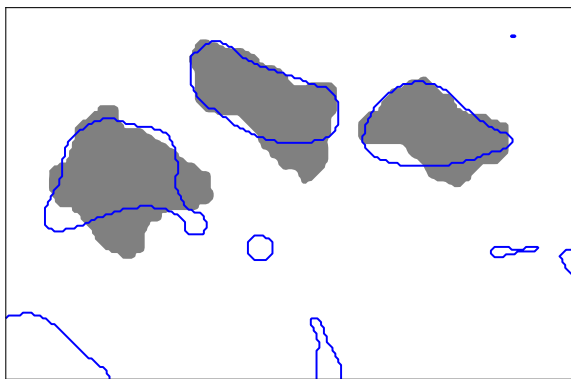
(c) $v_{p,max}/v_{p,min} = 4$.
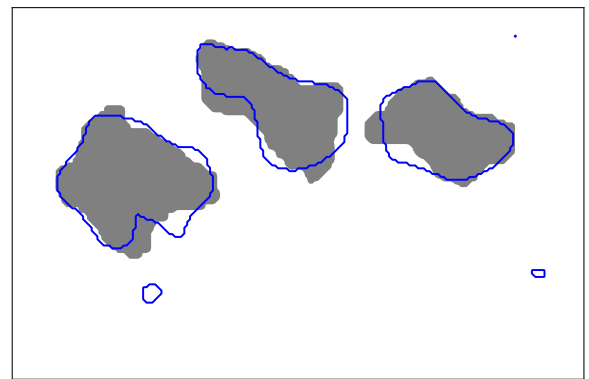
(d) $v_{p,max}/v_{p,min} = 5$.
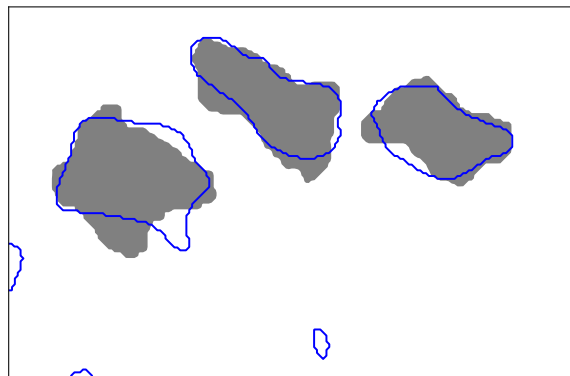
(e) $v_{p,max}/v_{p,min} = 6$.

Figure 5.35 − Reference data generated from source point located at $(0.65, 0.26)$. Receiver at $(0.65, 0.45)$, source and receiver positioning corresponding to case IV.

for all cases. The inversion parameters are presented together with each example, as well as the initial velocity model being used.
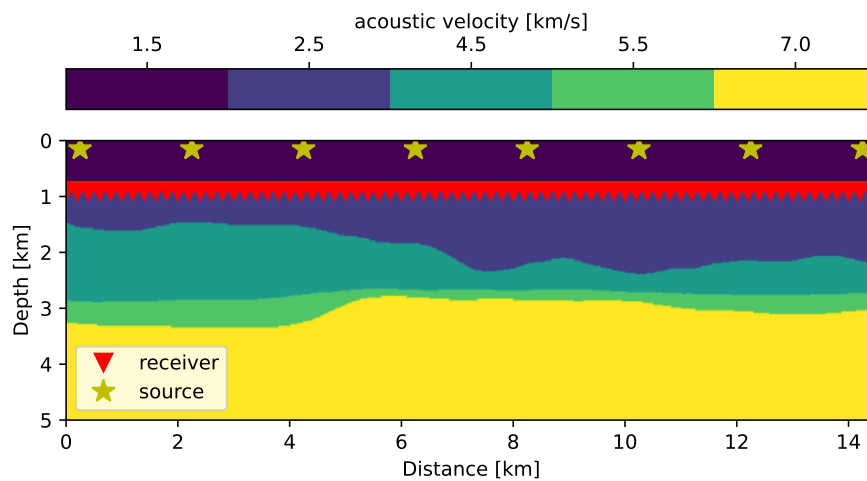
(a) "Poorly" illuminated case.
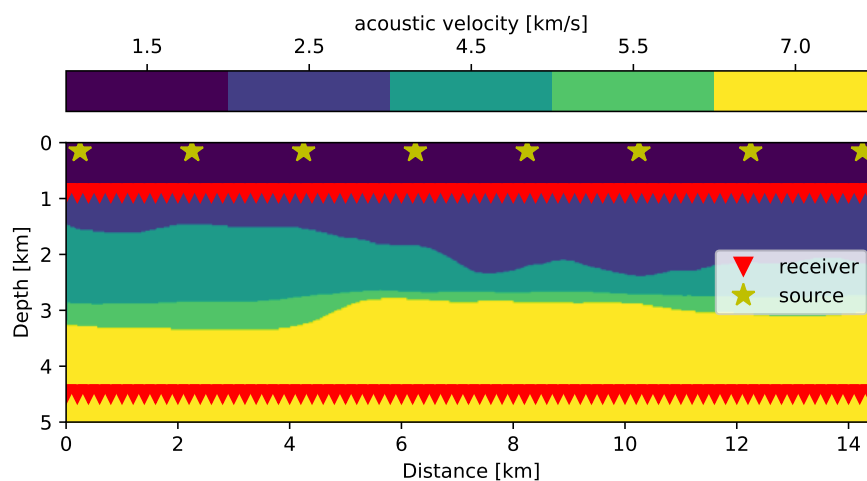
(b) "Well" illuminated case.

Figure 5.36 − The two geometry acquisitions considered for the Santos Basin model.

5.2.4   Regular FWI

In order to motivate the integer variable approach, "traditional" FWI was applied to the salt basin case, i.e., the continuous acoustic velocity field was taken as the control variable. The gradient was evaluated by the adjoint method and the velocity was updated using the Broyden-Fletcher-Goldfarb-Shanno (BFGS) method (NOCEDAL; WRIGHT, 1999). At first the spatial and stabilization filters were not employed.

(a) Initial guess used.

(b) Inversion result.

(c) Gradient at iteration 2.

(d) Gradient ploted over the velocity model. The gradient follows a linear transparency scale, so values close to zero are transparent.
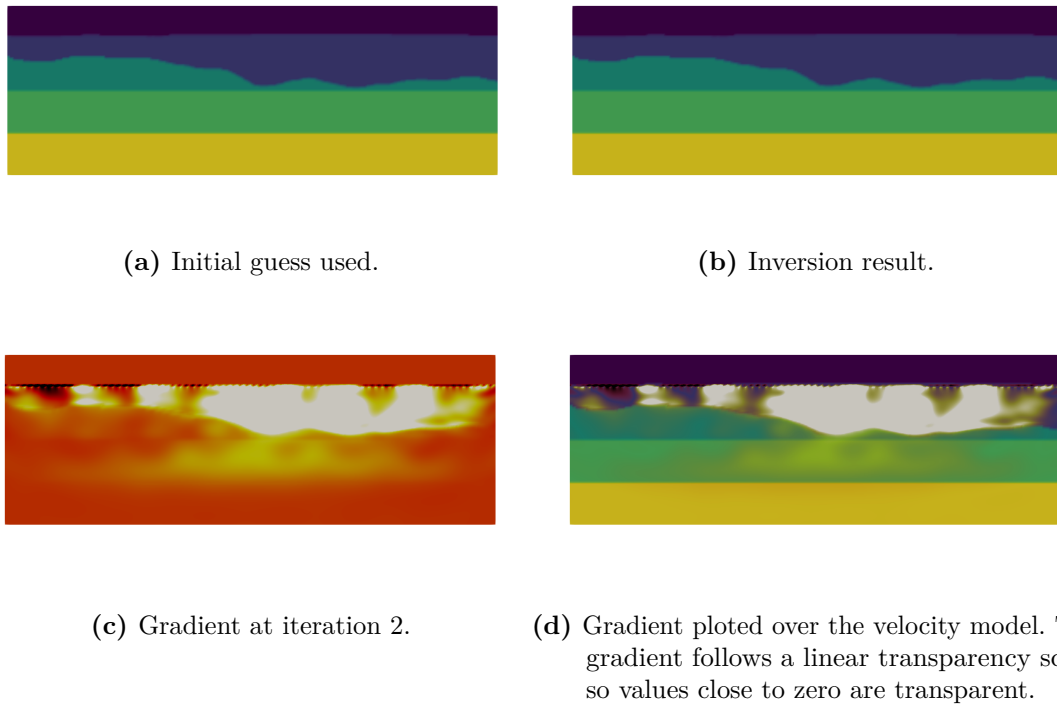
Figure 5.37 − FWI applied to salt basin velocity model.

Figure 5.37 shows the initial guess, final result, and the gradient information for one of the first few iterations. The velocity model changes during the inversion are so subtle that they are not visible in the original scale going from 1.5 km/s to 7 km/s. In addition, the gradient is ploted by itself in Figure 5.37c and superimposed over the velocity model in Figure 5.37d. It can be seen that the information is concentraded over the salt layer, and that the signal is much weaker underneath, which aligns with the results that fail to adjust for salt and subsalt regions.

In salt imaging it is often the case that the top of the salt is reasonably known, and the target area to be imaged is imediately underneath it. In that context, FWI for the salt and subsalt region was carried out by disregarding the gradient information above the known top of salt. In addition, the problem was facilitated by using the geometry acquisition with two lines of receivers, see Figure 5.36b. Four cases were considered, using the spatial filter, stabilization filter, both or nome of them, as displayed in Figure 5.38.

While fixing the top of salt and adding receivers did help in advancing the algorithm, Figure 5.38a shows that no significant improvement was achieved. From Figure 5.38b it can also be seen that the spatial filter had negligible impact on the inversion, contrary to the stabilization filter (5.38c), which moved most of the salt and subsalt region towards higher velocity values. The combination of both filters, shown in Figure 5.38d, did not yield better results, stopping the optimization after a few iterations due being unable of improving the misfit value.

(a) Regular FWI.

(b) FWI and spatial filter.

(c) FWI and stabilization filter.

(d) FWI combined with spatial and stabilization filter.
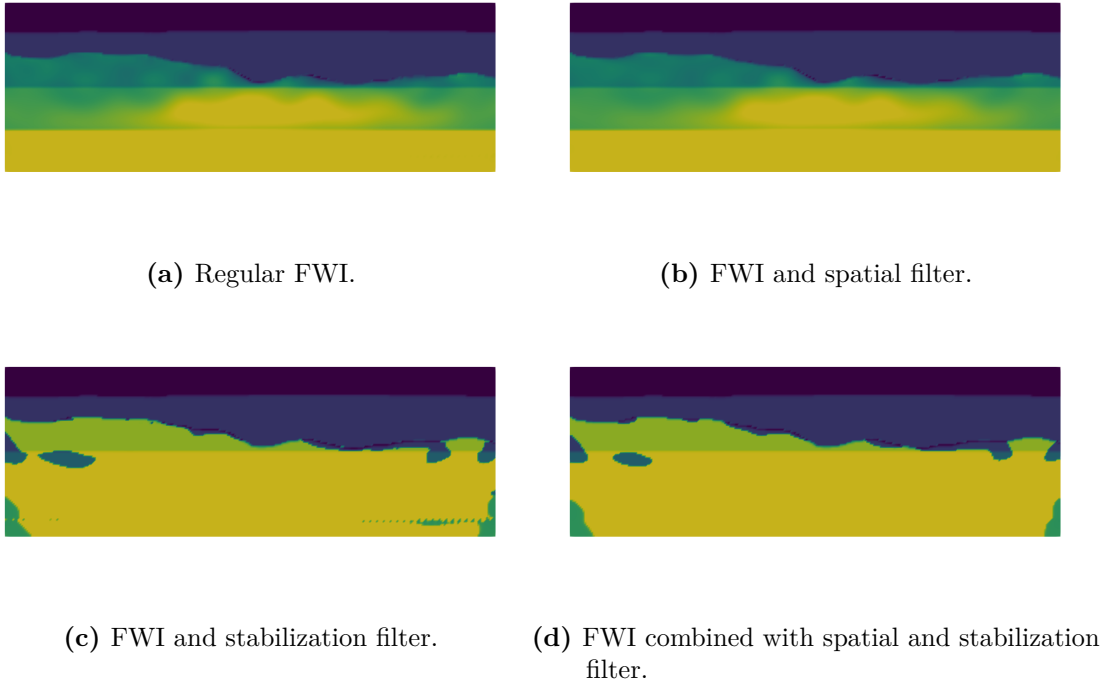
Figure 5.38 − FWI applied to salt basin velocity model. The top of salt is fixed and and an extra line of receivers was added to the bottom region of the domain.

5.2.5 Salt delineation

In order to study the viability of an integer control variable method to image the salt and subsalt region, an incremental approach was taken. In this section, the challenge of imaging the salt layer is considered. The problem parameters, as well as the discretization were the same as in Section 5.2.4, while the acquisition geometry employed was the reflective one (Figure 5.36a).

All the models so far inverted by ILP have only considered homogeneous background velocities. From the material model (3.3) it can be seen that there is no restriction over whether the background value v_p^{min} may vary spatially. That expression is slightly rearanged as follow, with spatial dependency made explicit, and a notation adapted to the FWI problem applied to salt imaging:

$$v_p(a(\mathbf{x})) = v_{p,back}(\mathbf{x})(1 - a^p(\mathbf{x})) + v_{p,salt}a^p(\mathbf{x}) \tag{5.3}$$

where $v_{p,back}$ is the spatially varying acoustic velocity background, and $v_{p,salt}$ is the scalar acoustic velocity value within the salt body. The background velocity model and the control variable a corresponding to the reference model are shown in Figure 5.39.

The inversion parameters used regarding sensitivity weights, step size and stopping criteria can be seen in Table 5.16.

The ILP approach was then applied to the problem of delineating the salt layer.
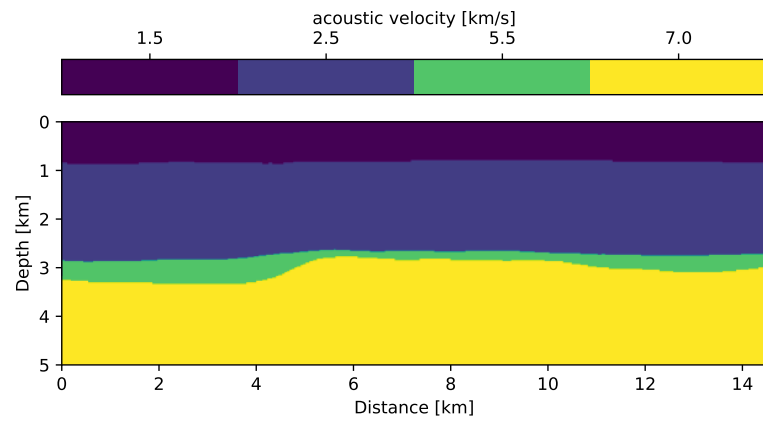
(a) Background velocity model $v_{p,back}(\mathbf{x})$.
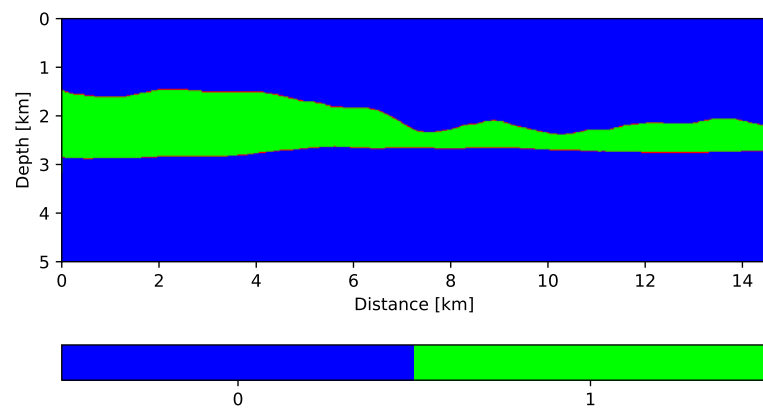
(b) Optimization variable $a(\mathbf{x})$.
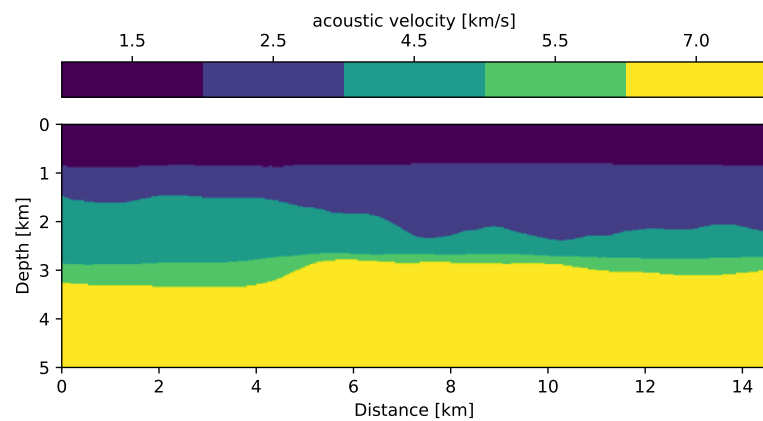
(c) Acoustic velocity field $v_p(\mathbf{x})$.

Figure 5.39 − Background and optimization field which combined result in the field $v_p(\mathbf{x})$.

Figure 5.40 shows the initial guess and the obtained velocity model, both for optimization variable and velocity model. It can be seen that the true salt model is well approximated, except for a spurious inclusion in the bottom left of velocity model, a region which is not well illuminated by the acquisition geometry being used. In a more general sense, this result validates the posibility of imaging salt bodies embedded within non-homogeneous background mediums. In this particular case, background acoustic velocities can be either

Inversion parameters			
1-norm constraint M	0.01	objective function threshold τ_J	1×10^{-16}
Filtering radius r	0.1	gradient threshold τ_G	1×10^{-14}
Damping weights γ_m, γ_v	0.99	Maximum number of iterations N_{max}	200

Table 5.16 − Inversion parameters used in the salt delineation case.

lower or higher than that of the salt layer.

(a) Initial guess for optimization variable.

(b) Ininitial guess for velocity model.

(c) Result for optimization variable.

(d) Result for velocity model.
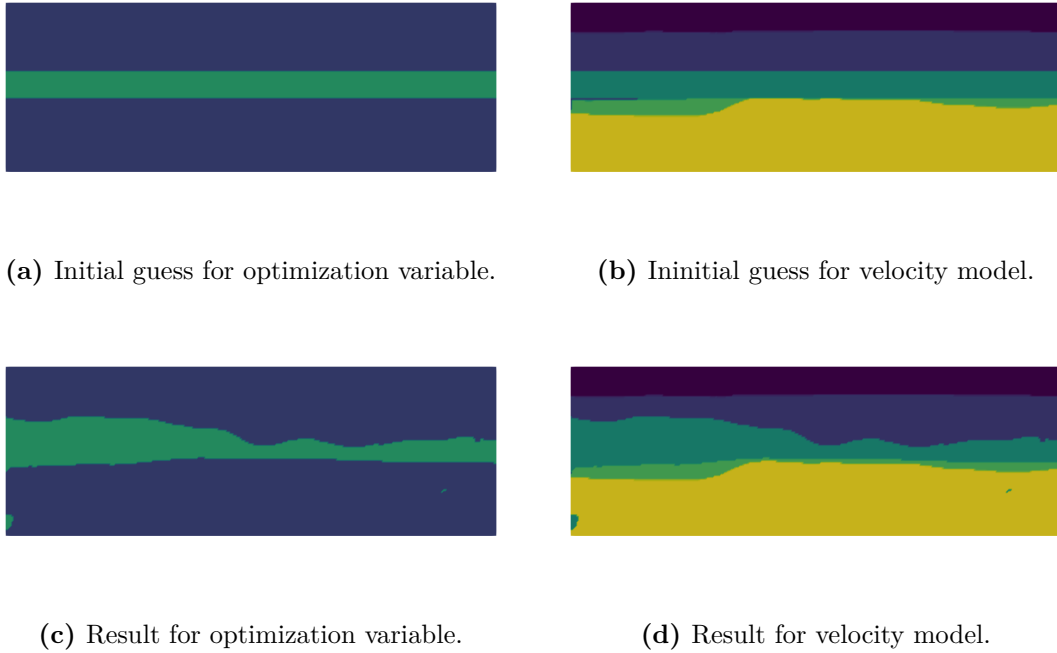
Figure 5.40 − ILP FWI applied to the salt basin velocity model. Both control variable and velocity model are shown.

The velocity model obtained in 5.40 raises the question if the relatively good fit can be attributed to a favourable initial guess. In order to investigate this possibility, the inversion is repeated with a totally homogeneous initial guess for the optimization variable, i.e, $a(\mathbf{x}) = 0$ everywhere. Beside initial guess, the only change in parameters was the maximum number of iterations N_{max}, raised to 300. Results are shown in Figure 5.41.

(a) Result for optimization variable.

(b) Result for velocity model.
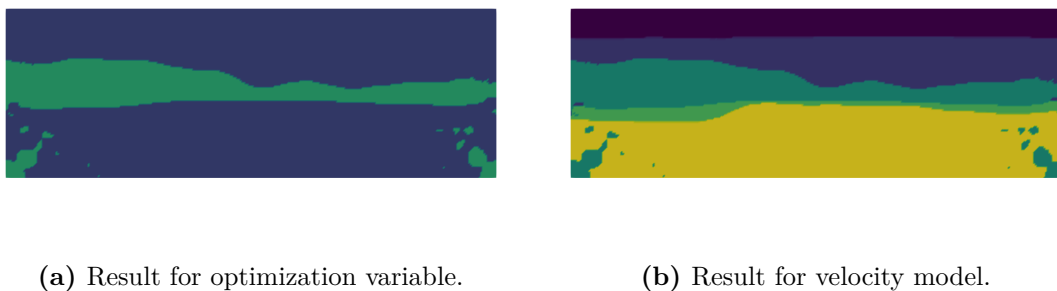
Figure 5.41 − ILP FWI applied to the salt basin velocity model with a homogeneous initial guess.

The quality of the recovered salt in the upper portion of the layer is similar, which is

$a_1(\mathbf{x})$	$a_2(\mathbf{x})$	$v_p(\mathbf{x})$
0	0	$v_{p,back}$
1	0	$v_{p,salt}$
1	1	$v_{p,res}$

Table 5.17 − Relationship between optimization variables and velocity values following Sivapuram et al. (2021).

to be expected since that is the most well illuminated region. The bottom of the layer also track relatively well with respect to the true body, except for the areas near the left and right border. In particular, the bottom corners, poorly illuminated regions in a reflective acquisition setup, display spurious salt inclusions. Nevertheless, similarly to the behaviour observed in Section 5.2.1, here it can be seen that the ILP approach was able to recovered the salt layer despite the unfavourable homogeneous initial guess.

5.2.5.1 Multimaterial

In hydrocarbon exploration, seismic imaging of saline structures is relevant mainly due to the presence of hydrocarbon reservoirs underneath them or in their vicinity. It is therefore natural to extend the inversion procedure in order to locate the reservoirs in addition to the salt region. In this section, we tackle this problem by allowing the integer control variable to assume three values, thus identifying each point in the domain either as background, salt or reservoir. The reflective geometry acquisition scheme from Figure 5.36a was used. The problem parameters, inversion parameters and discretization were the same as in previous sections.

In order to use non-binary integer variables, the generalized material models from Section 3.2.1 were employed. In the case considered, they map the integer values $\{0, 1, 2\}$ to $\{v_{p,back}, v_{p,salt}, v_{p,res}\}$, where $v_{salt} = 4.5$ km/s, $v_{res} = 5.5$ km/s, and $v_{p,back}$ varies throughout the domain. Figure 5.42 shows the optimization variable $a(\mathbf{x})$ and inhomogeneous background $v_{p,back}(\mathbf{x})$ that combined generate the reference velocity model.

In addition to those, the material interpolation law from Sivapuram et al. (2021) was used. In the generalized SIMP interpolation, instead of a single optimization variable $a(\mathbf{x})$ which may assume several integer values, several optimization binary fields $a_1(\mathbf{x}), \ldots, a_N(\mathbf{x})$ corresponding to each material are used. In the current case there would be two optimization variables, $a_1(\mathbf{x})$ and $a_2(\mathbf{x})$, associated with the salt structures and reservoir, respectively. The interpolation law read as follow:

$$v_p = (1 - a_1)v_{p,back} + a_1 \left[(1 - a_2)v_{p,salt} + a_2 v_{p,res} \right] \tag{5.4}$$

Table 5.17 shows the relationship between the optimization variables and the resulting velocity model $v_p(\mathbf{x})$, while Figure 5.43 displays it visually. The background is the same as in Figure 5.42a.
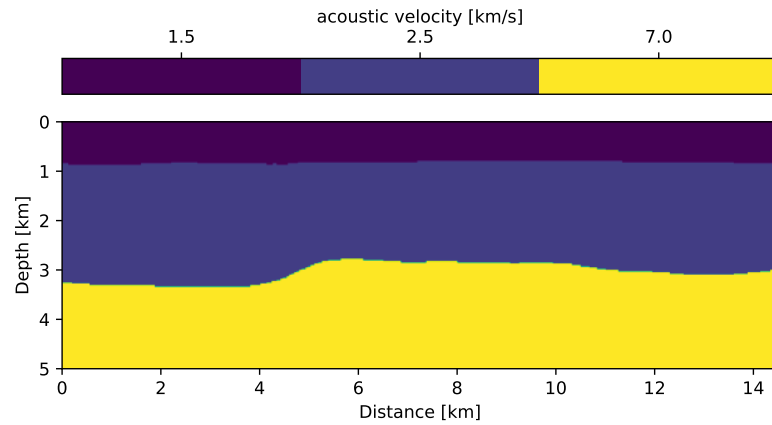
(a) Background velocity model $v_{p,back}(\mathbf{x})$.
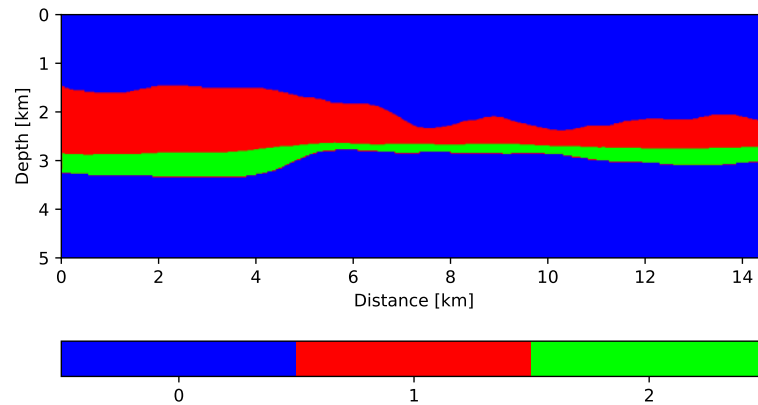
(b) Optimization variable $a(\mathbf{x})$.

Figure 5.42 − Background and optimization field for the generalized material models.
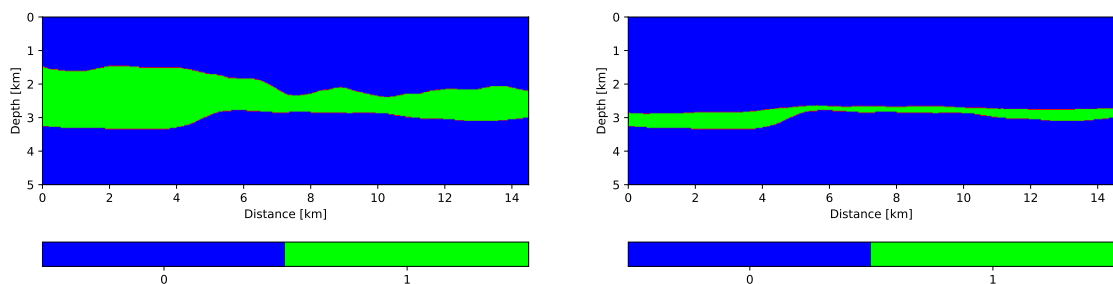
(a) Variable $a_1(\mathbf{x})$ indicates the presence of salt or reservoir.

(b) Variable $a_2(\mathbf{x})$ indicates the presence of a reservoir.

Figure 5.43 − Optimization variables that generate the reference model. Note how a_1 and a_2 overlap in the reservoir region, in accordance with Table 5.17.

The inversion was carried out with the single field approaches using the polynomial and the peak interpolation model, as well as the many fields approach. Initial guess and results are shown in Figure 5.44. It can be seen that the recovered velocity values steer towards

either the background or the reservoir, with barely any salt presence. Salt corresponds to the intermediate optimization variable value $a = 1$ in the single field approach, and to $a_1 = 1, a_2 = 0$ for the extended SIMP case. Indeed, the oscilation of the optimization variables between extreme values, irrespective of material model or number of fields used, is a consequence of the stabilization filter.

(a) Initial guess.

(b) Result obtained with polynomial model.

(c) Result obtained with peak model.

(d) Result obtained with generalized SIMP interpolation (SIVAPURAM et al., 2021).

Figure 5.44 – ILP FWI applied to the problem of locating both salt and reservoir, with different material interpolation laws.

Figure 5.45 shows the gradient value at depth = 1 km, distance = 7 km for the inversion using the peak material model for different stabilization filter weights. When the filter is not active ($\gamma = 0$), an unstable, oscilatory behaviour similar to that described in Section 5.1.1 appears. As the weight grows, this pattern dampens. This phenomenon is generally present in unfiltered integer variable TO (HUANG; XIE, 2007), so its manifestation in this application is not unexpected. In fact, the weight $\gamma = 0.5$ corresponds to the arithmetic average of the gradient from the two last iterations, which is the most common stabilization technique for integer TO (XIA et al., 2018; SIVAPURAM; PICELLI; XIE, 2018a). For acoustic inversion however, the weight γ has to be closer to unity as shown in Section 5.1.3. This in turn causes the gradient to vary smoothly, with no steep variation from one iteration to the next. Consequently, when a DoF associated with the background ($a = 0$) is updated to salt ($a = 1$), in the very next iteration the gradient will still mostly point towards the same direction, leading to a further update to reservoir ($a = 2$). The same holds true when the gradient points in the oposite direction, hence the tendency of the optimization variable to get "stuck" in upper or lower bound values.

Concerning the generalized SIMP approach, from the gradient expression 3.24 and
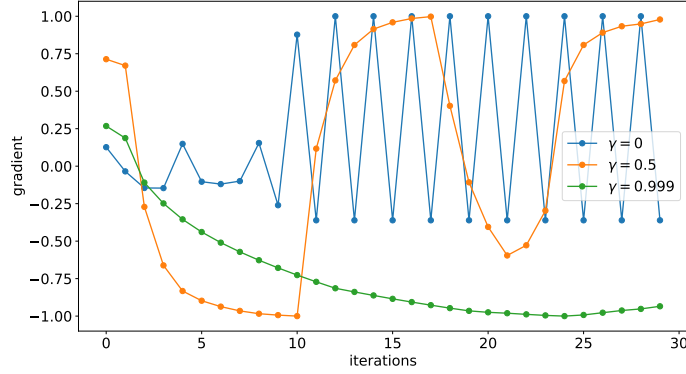
Figure 5.45 − Gradient evaluation at depth = 1 km, distance = 7 km.

from the derivatives of (5.4) it can be seen that, for each point in the domain, the gradients with respect to a_1 and a_2 are the same apart from a multiplicative constant. Therefore, in general, if the gradient leads a_1 to switch from 0 to 1, it will induce the same change to a_2. The same happens in the opposite direction, resulting in a state where the optimization variables are sinchronized at either the lower or upper bound, as exemplified in Figure 5.44d.

In fact, the stabilization filter limits the range of gradient variation from one iteration to the next. This can be highlighted by looking at how the gradient varies from one iteration to the next with and without filter, and how these two quantities are related. The stabilization filter equations are repeated here for clarity sake:

$$
\begin{aligned}
m_k &= \gamma_m m_{k-1} + (1 - \gamma_m) g_{bef}^k \\
v_k &= \gamma_v v_{k-1} + (1 - \gamma_v) g_{bef}^k \odot g_{bef}^k \\
g_{aft}^k &= \frac{m_k}{\sqrt{v_k + \varepsilon}}
\end{aligned}
\tag{5.5}
$$

where g_{bef}^k and g_{aft}^k are the gradient at the kth iteration before and after passing through the stabilization filter, respectively. Combining the three equations from Eq. (5.5) (and assuming $\gamma_m = \gamma_v = \gamma, \varepsilon = 0$) allows us to write:

$$
g_{aft}^k = \frac{m_k}{\sqrt{v_k}} = \frac{\gamma m_{k-1} + (1 - \gamma) g_{bef}^k}{\sqrt{\gamma v_{k-1} + (1 - \gamma) g_{bef}^k \odot g_{bef}^k}}
\tag{5.6}
$$

The gradient variation between iterations Δ is introduced, leading to:

$$
g_{aft}^k = g_{aft}^{k-1} + \Delta_{aft}^k = \frac{\gamma m_{k-1} + (1 - \gamma)(g_{bef}^{k-1} + \Delta_{bef}^k)}{\sqrt{\gamma v_{k-1} + (1 - \gamma)(g_{bef}^{k-1} + \Delta_{bef}^k) \odot (g_{bef}^{k-1} + \Delta_{bef}^k)}}
\tag{5.7}
$$

Using Eq. (5.5) to express g_{aft}^{k-1}, m_{k-1} and v_{k-1} in terms of g_{bef}^{k-1}, it is possible to write the
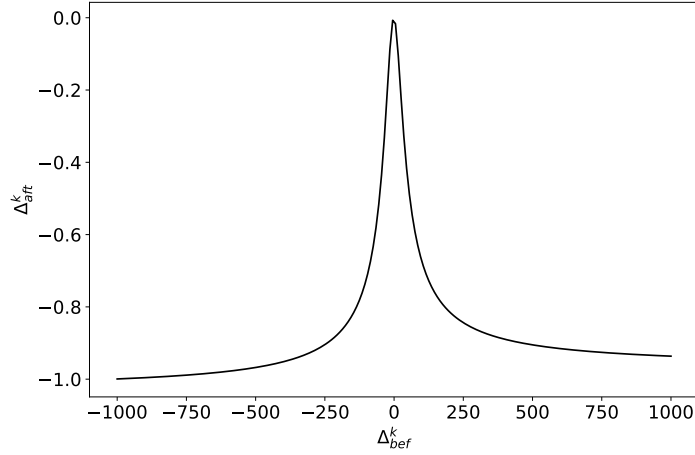
Figure 5.46 − Relationship between filtered and unfiltered gradient variation at iteration k.

variation Δ_{aft}^k as a function of Δ_{bef}^k as follows:

$$
\Delta_{aft}^k = \frac{\gamma^2 m_{k-2} + \gamma(1-\gamma)g_{bef}^{k-1} + (1-\gamma)(g_{bef}^{k-1} + \Delta_{bef}^k)}{\sqrt{\gamma^2 v_{k-2} + \gamma(1-\gamma)g_{bef}^{k-1} \odot g_{bef}^{k-1} + (1-\gamma)(g_{bef}^{k-1} + \Delta_{bef}^k) \odot (g_{bef}^{k-1} + \Delta_{bef}^k)}}
$$
$$
- \frac{\gamma m_{k-2} + (1-\gamma)g_{bef}^{k-1}}{\sqrt{\gamma v_{k-2} + (1-\gamma)g_{bef}^{k-1} \odot g_{bef}^{k-1}}} \tag{5.8}
$$

In order to visualize the relationship γ is set to 0.999, a value used in several examples in this work. The quantities m_{k-2}, v_{k-2} and g_{k-1} are arbitrarily set to 1, however, different values for any of them do not change the behaviour of the curve shown in Figure 5.46. It can be seen that gradient variations with large magnitude $|\Delta_{bef}^k|$ are dampened considerably. In addition, the slope of the curve decreases as $|\Delta_{bef}^k|$ increases, meaning that the magnitude of the filtered values $|\Delta_{aft}^k|$ is limited and the difference between their values decreases as $|\Delta_{bef}^k|$ grows.

The implication is that the multimaterial interpolation scheme investigated above is unlikely to succeed. In particular, consider a problem where the allowed design variables are $\{0, 1, 2\}$. A DoF in which the design variable shifted from 0 to 1 at iteration k may need a big variation $|\Delta_{aft}^{k+1}|$ in the gradient at iteration $k + 1$ so that the design value remains at 1 instead of going from 1 to 2. However, if this larger variation is simply not possible, the design values will change and the "locking" phenomenom will appear.

5.2.5.2 Sequential Multimaterial

In order to combine a non-binary integer design variable with the stabilization filter, a sequential approach is proposed. The interpolation laws from Section 3.2.1 are still used, however, the ILP problem is adapted to allow only a binary subset of design variables to change at a time. For a given problem with $a \in \{0, \dots, N_m\}$, a lower bound $0 \leq L < N_m$

Inversion parameters			
1-norm constraint M	0.005	objective function threshold τ_J	1×10^{-16}
Filtering radius r	0.15	gradient threshold τ_G	1×10^{-14}
Damping weights γ_m, γ_v	0.999	Maximum number of iterations N_{max}	1000

Table 5.18 − Inversion parameters used in pseudomultimaterial case.

and a upper bound $0 < U \le N_m$ are defined such that L and U are neighboring integers. By modifying the bound constraints in the ILP problem it is possible to allow only design variable changes when $a \in \{L, U\}$, which is a binary approach. By shifting L and U it is possible to switch the target material properties, sweeping all materials from 0 to N_m, thus resulting in a pseudo multimaterial scheme.

Figure 5.47 illustrates two choices of bounds L, U for the salt basin problem. Figure 5.47a shows the velocity model composed of water layer ($v_p = 1.5$ mk/s), sediment ($v_p = 2.5$ mk/s), salt layer ($v_p = 4.5$ mk/s), reservoir ($v_p = 5.5$ mk/s) and basement ($v_p = 7$ mk/s). Figure 5.47b shows the design values associated to the reference model, which can assume the values $\{0, 1, 2\}$. There are two possible choices of inner bounds, either $(0, 1)$ or $(1, 2)$. The first case is displayed in Figure 5.47c, where only the active regions appear, and the subdomain where $a = 2$, which stays fixed, is transparent. On the same vein, Figure 5.47d shows the active regions when the design variable bounds are $(1, 2)$. In that case, the background corresponding to $a = 0$ stays fixed.

The pseudo multimaterial sub-optimization ILP problem can be written as:

$$
\begin{aligned}
\underset{\Delta a^k}{\text{minimize}} \quad & \nabla_a f \cdot \Delta a^k \\
\text{subject to} \quad & \Delta a^k = \Delta a_P^k + \Delta a_N^k \\
& \|\Delta a_P^k\|_1 \le M/2 \\
& \|\Delta a_N^k\|_1 \le M/2 \\
& \Delta a_P^k \in \{0, \delta(a - L^k)\} \\
& \Delta a_N^k \in \{-\delta(a - U^k), 0\} \\
& L^k, U^K \in \{0, \dots, N_m\} \quad \wedge \quad U^k = L^k + 1
\end{aligned}
\tag{5.9}
$$

This approach is applied to the problem of salt and reservoir identification presented in Section 5.2.5.1. The problem parameters and discretization used were kept the same. Inversion parameters are presented in Table 5.18.

Since the multimaterial interpolation law is retained, the reference model for the design variables remains as shown in Figure 5.42, with $a \in \{0, 1, 2\}$ mapping to $\{v_{p,back}, v_{p,salt}, v_{p,res}\}$. The initial guess features only a central salt layer, without assigning a reservoir region anywhere, as depicted in Figure 5.48. The first example considers the favourable geometry acquisition depicted in Figure 5.36b. The polynomial interpolation law is chosen for material

(a) Reference velocity model.

(b) Design variable. $a = 1$ corresponds to salt, $a = 2$ to the reservoir. When $a = 0$ the acoustic velocity corresponds to the fixed background.

(c) Active region when the bounds (L, U) of a are $L = 0$, $U = 1$. Salt (red) is distributed within the fixed background (blue).

(d) Active region when the bounds (L, U) of a are $L = 1$, $U = 2$. Reservoir (green) is distributed within the salt layer (red).
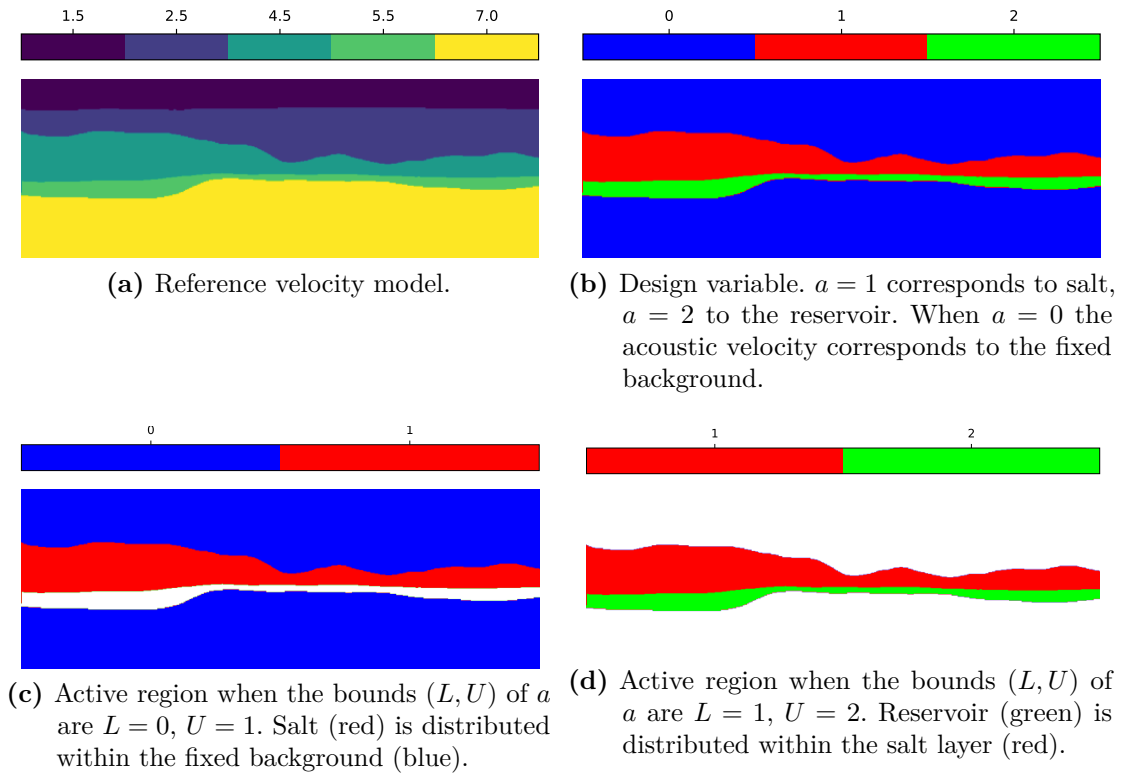
Figure 5.47 − Illustration of the pseudomultimaterial approach.

modelling. The binary inversion problem switch bounds L and U at every $N_{switch} = 200$ iterations.

Figure 5.49 show the evolution of the process at different points of the inversion. At first the bounds are $(0, 1)$, and the region corresponding to 2 is fixed. Since the reservoir ($a = 2$) is not present in the initial guess, there is only salt ($a = 1$) being distributed within the fixed background ($a = 0$). In Figure 5.49a, at iteration 51, salt is still being distributed, with the right portion mostly unresolved. In Figure 5.49b, at iteration 151, the salt is already mostly defined. At iteration 200 the design variable bounds are switched to $(1, 2)$. The fixed background ($a = 0$) is now fixed, and reservoir ($a = 2$) is distributed within the salt layer ($a = 1$). In Figure 5.49c, at iteration 201, a small clear spot appears inside the salt, which corresponds to reservoir. At iteration 216, as shown in Figure 5.49d, the reservoir layer is already taking form. At iteration 301 (5.49e), the layer is mostly defined and changes little up to the 400th iteration, when there is a new bound switch. At this point the process starts over again, halting when the stopping criteria for the inversion is met.

The history of the objective function during inversion, in addition to selected snapshots of the velocity model, are shown in Figure 5.50. It can be seen that approximatedly 100 iterations are needed to correctly locate the salt layer, and no abrupt variations occur thereafter. At iteration 200 there is a sudden drop associated with the switch in upper and lower design variable bounds. Once again, the value of the objective function mostly settles
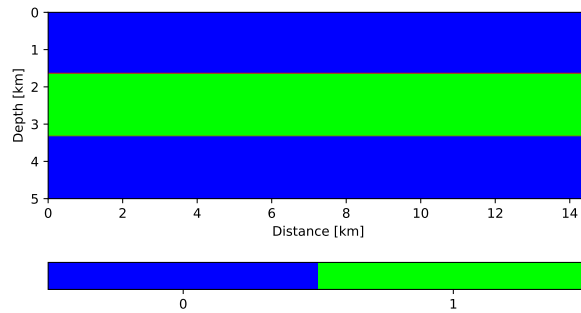
(a) Initial guess for $a(\mathbf{x})$.
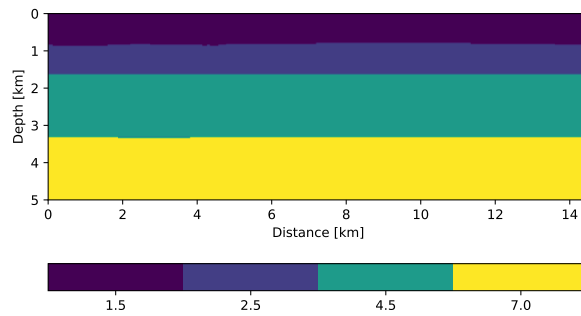
(b) Initial guess for $v_p(\mathbf{x})$.

Figure 5.48 − Initial guess for salt and reservoir reconstruction.

until a new switch is introduced at iteration 400. From that point until iteration 600 the behaviour is mostly chaotic since the salt region is already well defined. Nevertheless, the value of the objective function still decreases slightly until the procedure stops.

Quality measure Q

material model	peak function	polynomial interpolation
well illuminated	4.289×10^2	5.5304×10^2
poorly illuminated	7.9207×10^2	8.5034×10^2

Table 5.19 − Quality measures in the pseudomultimaterial case.

The next inversion example draws a comparison between the two interpolation laws being considered. In addition, both geometry acquisitions from Figure 5.36 were employed. With regard to illumination, it can be seen that, once more, the ILP approach ends up with artifacts in the shadow regions when the regular reflective acquisition setup was used. With respect to material model, Figure 5.36 and Table 5.19 suggest that both interpolations perform similarly. Albeit that being the case here, the peak model is still more flexible given the free parameter σ_j associated to each acoustic velocity $v_{p,back}$, $v_{p,salt}$ and $v_{p,res}$, which allows controlling the slope at material transitions (see Equation (3.5) and Figure

(a) 51th iteration: salt within fixed background. **(b)** 151th iteration: Salt mostly defined. Reservoir ($a = 2$) out of the bounds (0, 1).

(c) 201th iteration: Bounds switched to (1, 2) Reservoir region appears. **(d)** 216th iteration: Reservoir layer taking form within salt layer. Background ($a = 0$) fixed.

(e) 301th iteration: Reservoir layer reasonably well defined.
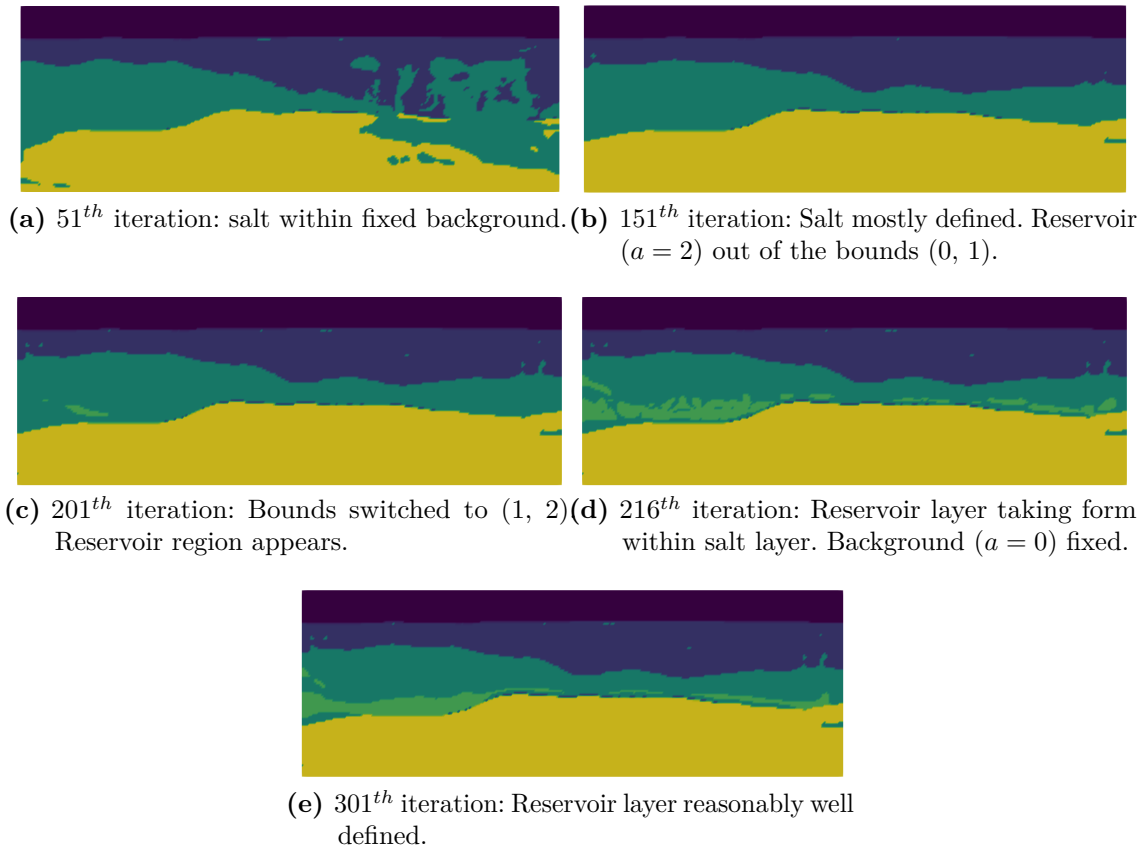
Figure 5.49 − Sequential approach at various points of the inversion.

3.2). Most importantly, the experiments with the pseudo multimaterial approach have shown to be relatively successfull in recovering both salt and reservoir.

5.2.5.3 Fixed Top of Salt

FWI reconstruction of velocity models in the presence of salt bodies is challenging because of the sensitivity of subsalt images with respect to the salt model. One approach used in the industry is to build the sediment velocity model, followed by top-of-salt (ToS) identification, base-of-salt (BoS) interpretation and finally salt scenario testing (WANG et al., 2019). The salt interface contrast combined with the high acoustic velocity makes it harder to estimate the BoS in comparison to the ToS. Therefore, in this section we consider the scenario where the ToS is known, and the objective is to correctly reconstruct the reservoir and basement regions beneath it.

In order to highlight the need of incorporating the salt body restriction in such a scenario, FWI with a continous variable was applied to the salt basin case with a known ToS. The ToS geometry was imposed by muting the gradient information above it, thus avoiding any model update in that region. The continuous acoustic velocity field was taken as the control variable, and the velocity was updated using the BFGS method (NOCEDAL; WRIGHT, 1999). In addition, neither spatial nor stabilization filters were employed.
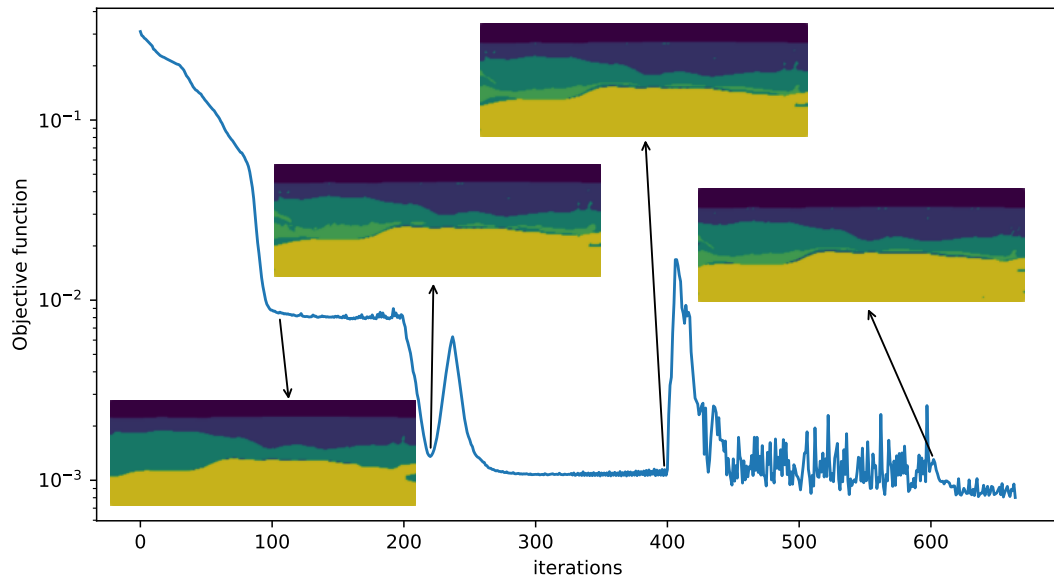
Figure 5.50 − Optimization history and snapshots at iterations 100, 220, 399 and 599.

(a) peak function material model, well illuminated.

(b) polynomial interpolation material model, well illuminated.

(c) peak function material model, poorly illuminated.

(d) polynomial interpolation material model, poorly illuminated.
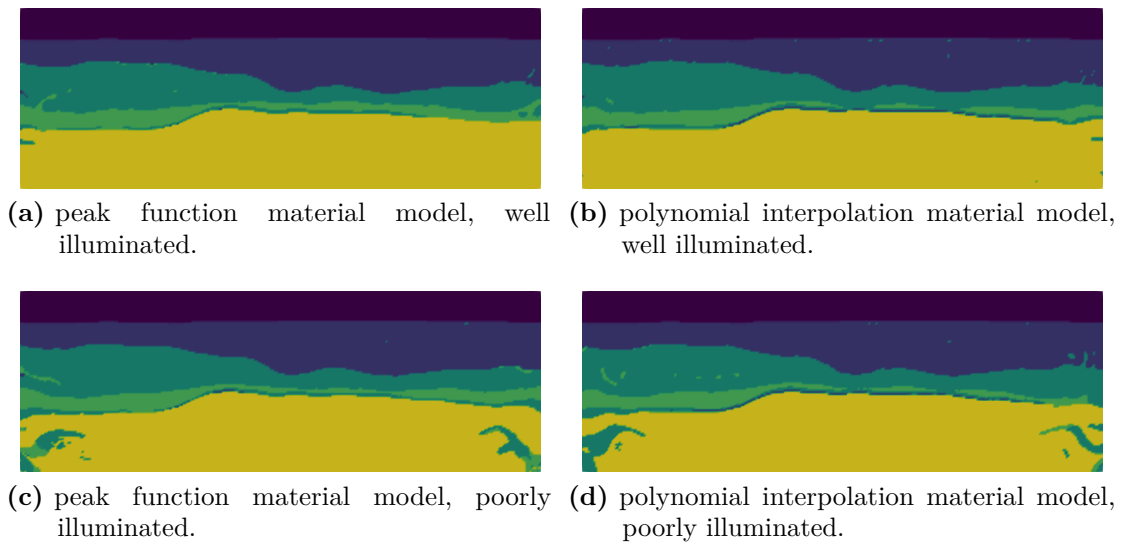
Figure 5.51 − Inversion result for well and poorly illuminated geometry acquisitions, considering both peak function and polynomial interpolation material models .

Figure 5.52 presents the inversion results. Figure 5.52a shows the initial guess, which assumes just the presence of reservoir and basement layers below the salt. In Figure 5.52b, it's difficult to discern a clear separation between the basement (colored in yellow), reservoir (light green), and salt (darker green). In the subsequent Figure 5.52c, the gradient at the fourth iteration of the inversion process is displayed. There is a narrow region below the Top of Salt (ToS) where the gradient is more pronounced, as indicated by higher absolute values. Figure 5.52d overlays these higher values on the inversion results, highlighting that in the target area encompassing the reservoir and basement, the gradient values are relatively lower, complicating the reconstruction in this region. This observation emphasizes the importance of integrating prior information about the distinct nature of

(a) Initial guess.

(b) Result obtained.

(c) Gradient at 4th iteration.

(d) Gradient ploted over the obtained velocity model.
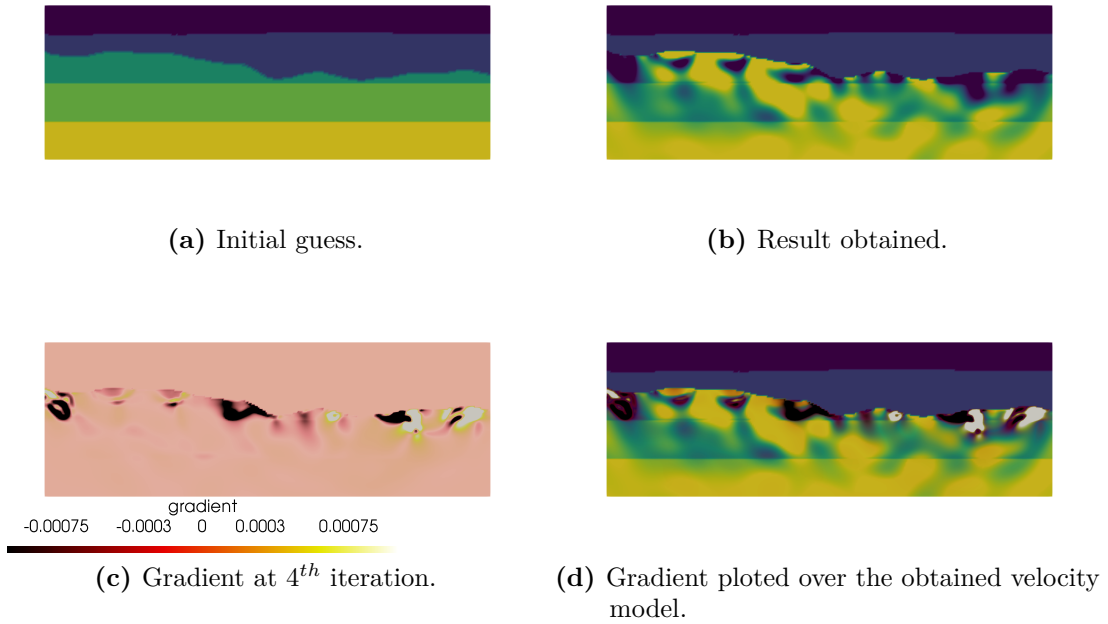
Figure 5.52 − Inversion result for fixed ToS and continous design variable.

the acoustic velocity distribution to effectively guide the inversion.

To implement the discretized scheme in this case, the multimaterial mapping used for $v_p(\mathbf{x})$ is:

$$v_p(\mathbf{x}) = \begin{cases} v_{p,back}(\mathbf{x}) & \text{if} \quad a(\mathbf{x}) = 0 \\ v_{p,res} & \text{if} \quad a(\mathbf{x}) = 1 \\ v_{p,base} & \text{if} \quad a(\mathbf{x}) = 2 \end{cases} \tag{5.10}$$

where $v_{p,res} = 5.5$ km/s and $v_{p,base} = 7.0$ km/s. The fields $v_{p,back}$ and $a(\mathbf{x})$, which combined reconstruct the reference velocity model, are shown in Figure 5.53. In particular, the peak function interpolation law from Equation 3.5 was chosen to connect a and v_p.

The reflective acquisition geometry acquisition from Figure 5.36a is applied to the subsalt identification problem. Problem parameters and discretization are the same as in Section 5.2.5.3. For all problems considered, the initial guess consists of horizontal layers of the two material parameters expected to be found beneath the salt, reservoir and basement, as shown in Figure 5.53c.

In this example, the peak function interpolation law is used. The inversion algorithm follows the same sequential approach, with N_{switch} set to 150. The updating schemes starts with U=0, L=1, meaning that the reservoir region is distributed within the fixed background region. At the 151th iteration, the bounds switch to U=1, L=2, setting the basement structure to be distributed within the reservoir region. After 150 iterations the bounds U and L switch back and the procedure starts again.
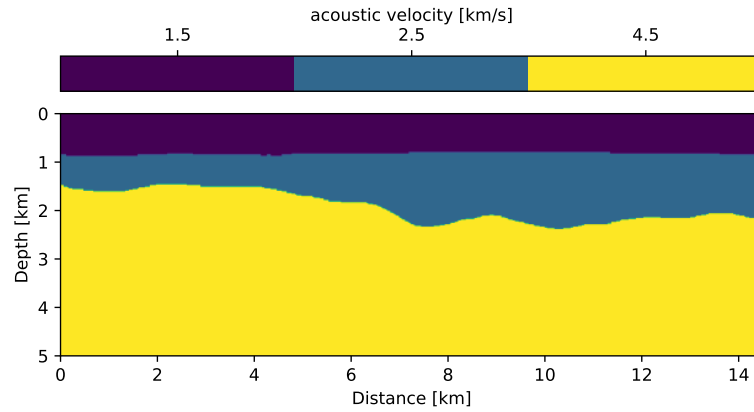
(a) Background velocity model $v_{p,back}(\mathbf{x})$.
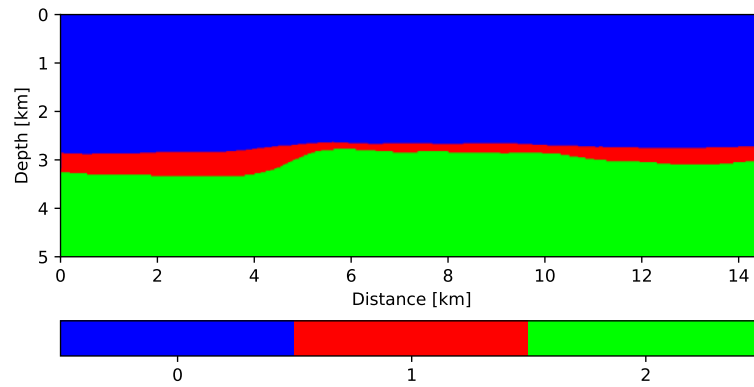
(b) Optimization variable $a(\mathbf{x})$.
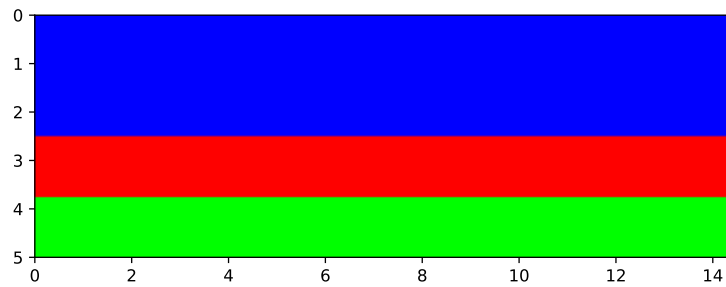
(c) Initial guess for optimization variable $a(\mathbf{x})$.

Figure 5.53 − The background and optimization fields which combined result in the field $v_p(\mathbf{x})$ for fixed top of salt are displayed in Figure (a) and (b). Figure (c) shows the control variable initial guess used in this Section .

While the current approach located somewhat sucessfully the salt layer in Section 5.2.5.3, it also suffered from artifacts in the poorly illuminated bottom corner regions. In order to investigate the influence of the spatial and stabilization filter parameters on the reconstruction, a sweeping experiment was performed. Based on what has been observed to be an "effective range", the inversion was carried out considering radii $r \in \{0, 0.05, 0.1, 0.15, 0.2, 0.25\}$ for the spatial filter and weights $\gamma \in \{0.25, 0.5, 0.75, 0.9, 0.99, 0.999\}$ for the stabilization filters. The result for all these inversions was put together and shown

in Figure 5.54.
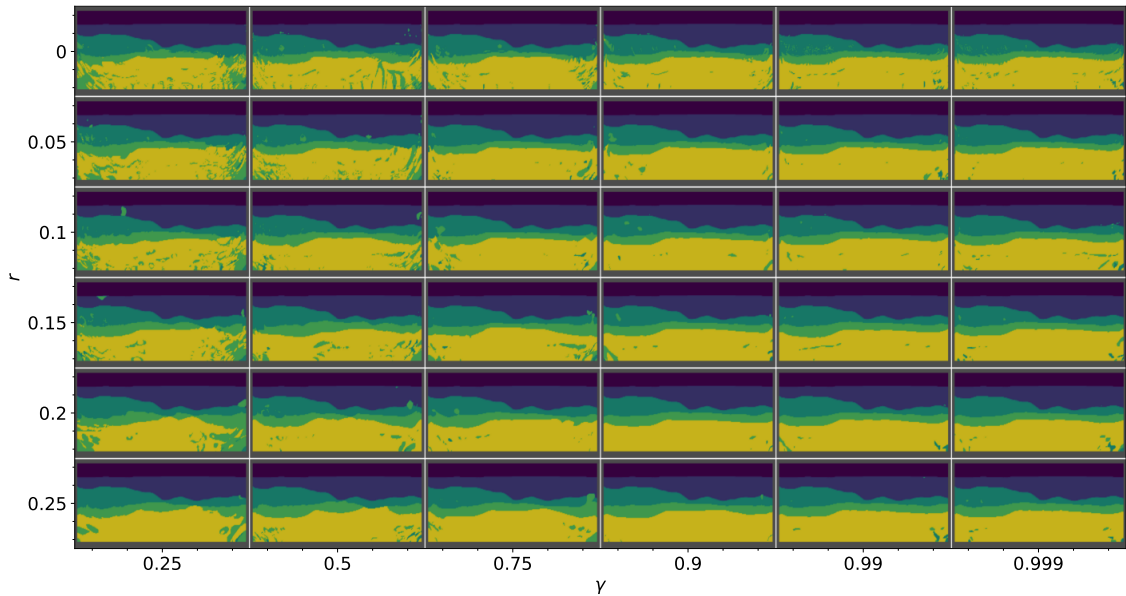
Figure 5.54 − Final result for inversion with fixed top of salt considering several choices for the spatial filter parameter r and weight γ for the stabilization filter.

From the plot it can be seen that weights γ up to 0.75 control very poorly for the appearance of artifacts, irrespective of the radius r used. Considering results with $\gamma \geq 0.9$, small artifacts are less present as r increases (top to bottom). For $r \geq 0.2, \gamma \geq 0.9$, the velocity models obtained have a clearly defined salt layer and diminished corner artifacts. Although the result for $\gamma = 0.9, r = 0.25$ may seem the best one given the absence of artifacts at the bottom, a qualitative analysis shows that may not be the case.
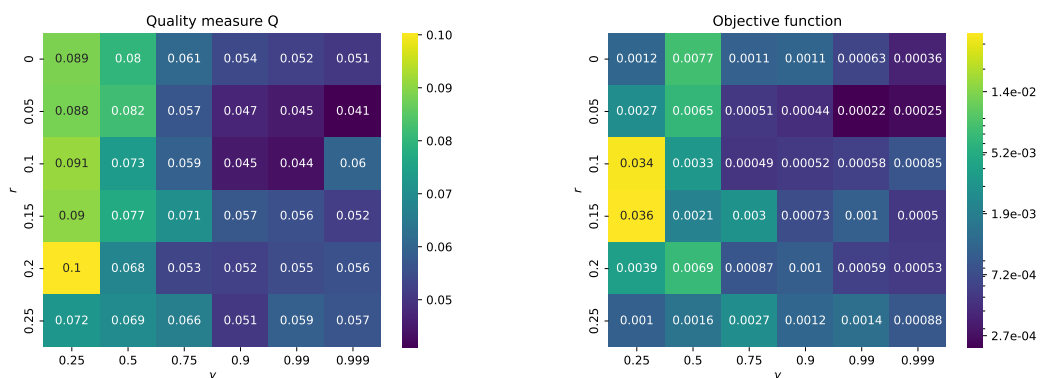
(a) Measure of the difference between recovered and reference model.

(b) Objective function value.

Figure 5.55 − Quality measure (a) and final value of the objective function (b) for all cases.

Figure 5.55 shows heat maps for both quality measure Q (Equation 5.1) and objective function value for the cases considered. It can be seen that, while the case $r = 0.25, \gamma = 0.9$ has a low Q score and no corner artifacts, it is not the result with biggest agreement

to the reference model. The velocity models obtained in the range $0.05 \leq r \leq 0.1$, $0.9 \leq \gamma \leq 0.999$ achieve similar or lower Q measures despiste the artifacts due to a better salt layer reconstruction. This difference is highlighted in Figure 5.56, where the interfaces for case $r = 0.25, \gamma = 0.999$ and $r = 0.05, \gamma = 0.9$ are superimposed. There, it can be seen that the result with higher γ, but lower r (in black), fits much closer the reference model salt layer (in red) than the lower γ, higher r case, despite having more regions corresponding to artifacts. This relationship illustrates the main impact of the r parameter, since higher values are more effective in reducing artifacts, while at the same time sacrificing precision in the salt layer reconstruction. Therefore, in these circumstances the radius r used depends on the priority being interface definition in the upper portion of the model, or freedom from artifacts in the shadow regions of the domain.
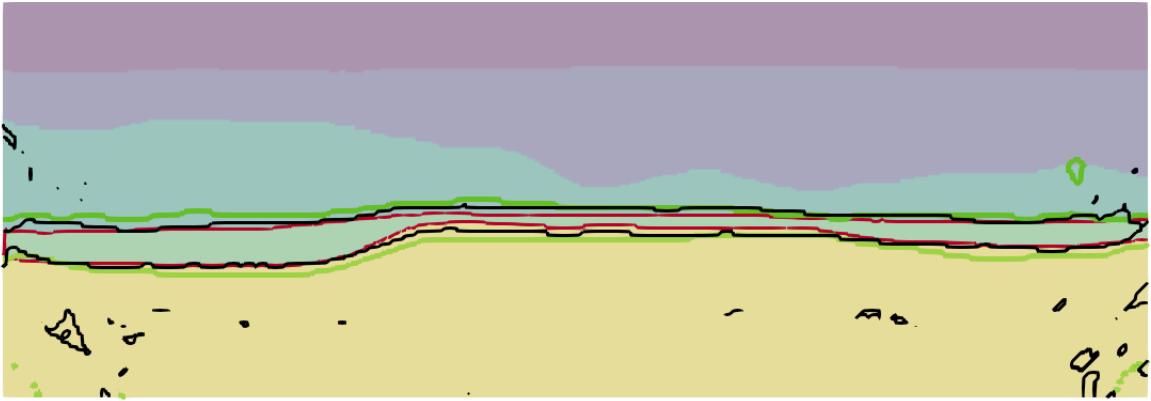
Figure 5.56 − Contour lines of the salt layer obtained for i) case $r = 0.05$, $\gamma = 0.999$ (black), ii) case $r = 0.25$, $\gamma = 0.9$ (green), iii) reference model (red) .

The best results in Figure 5.55a still display artifacts, mostly in the bottom corner regions. This is to be expected, and these so-called shadow regions are bound to have poorer recontruction (KADU; LEEUWEN; MULDER, 2016). To eliminate the influece from these artifacts the analysis is repeated without taking these corners into account. If before Q was calculated considering the whole computational domain Ω, now the integral from (5.1) is calculated excluding the shadow zone Ω_s (See Figure 5.57a). The reassessment was done for circular regions with radius ranging from 1 to 3 km. Their impact on the Q values grew in tandem with the size of the area excluded. Nevertheless, the results did not qualitatively change, regardless of the circle size. This can be seen in Figure 5.57b, wich considers the case with the largest exclusion zone. The order relation between cases with regards to Q values did not change, indicating that the measure adequately evaluated the quality of the inversion, and did not get "contaminated" by the discrepancies at the shadow corner regions.

5.2.5.4   Fixed ToS: no inverse crime

In the last examples that considered the salt layer model, the existence of inverse crime was ignored. In this section this problem is addressed as was done in Section 5.2.1, by

(a) Reference velocity model with shadow region Ω_s marked. The corners are occupied by quarter circles with 3 km radius.
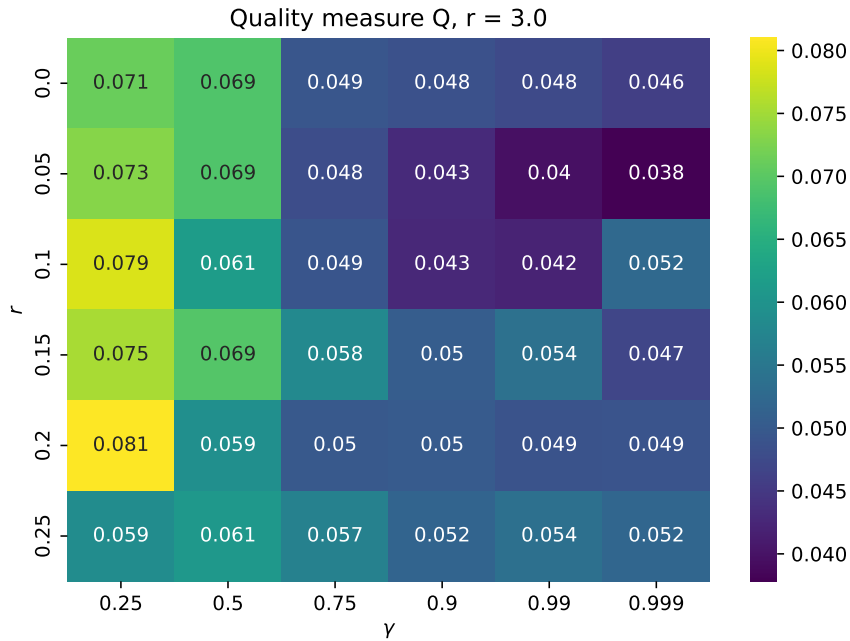
(b) Inversion quality measure when shadow zone is ignored.

Figure 5.57 − Quality measure for several choices of parameters r, γ when the poorly illuminated region, shown in Figure (a), is excluded.

adding gaussian noise to the reference signal. Inversions were carried out for four different filter parameter configurations with low Q scores:

- $r = 0.05$, $\gamma = 0.999$

- $r = 0.1$, $\gamma = 0.99$

- $r = 0.05$, $\gamma = 0.99$

- $r = 0.25$, $\gamma = 0.9$

The configuration was kept the same, a reflective geometry acquisition setup in conjunction with the peak function material model using the sequential pseudo-multimaterial approach, switching between distributing reervoir or basement material at every $N_{switch} = 150$

iterations was used. Figure 5.58 presents the results for these cases, and a side-by-side comparison to the original inversion with crime. The MNL used was 9,5% for all examples.

(a) $r = 0.05$, $\gamma = 0.999$, no inverse crime.

(b) $r = 0.05$, $\gamma = 0.999$, with inverse crime.

(c) $r = 0.1$, $\gamma = 0.99$, no inverse crime.

(d) $r = 0.1$, $\gamma = 0.99$, with inverse crime.

(e) $r = 0.05$, $\gamma = 0.99$, no inverse crime.

(f) $r = 0.05$, $\gamma = 0.99$, with inverse crime.

(g) $r = 0.25$, $\gamma = 0.9$, no inverse crime.

(h) $r = 0.25$, $\gamma = 0.9$, with inverse crime.
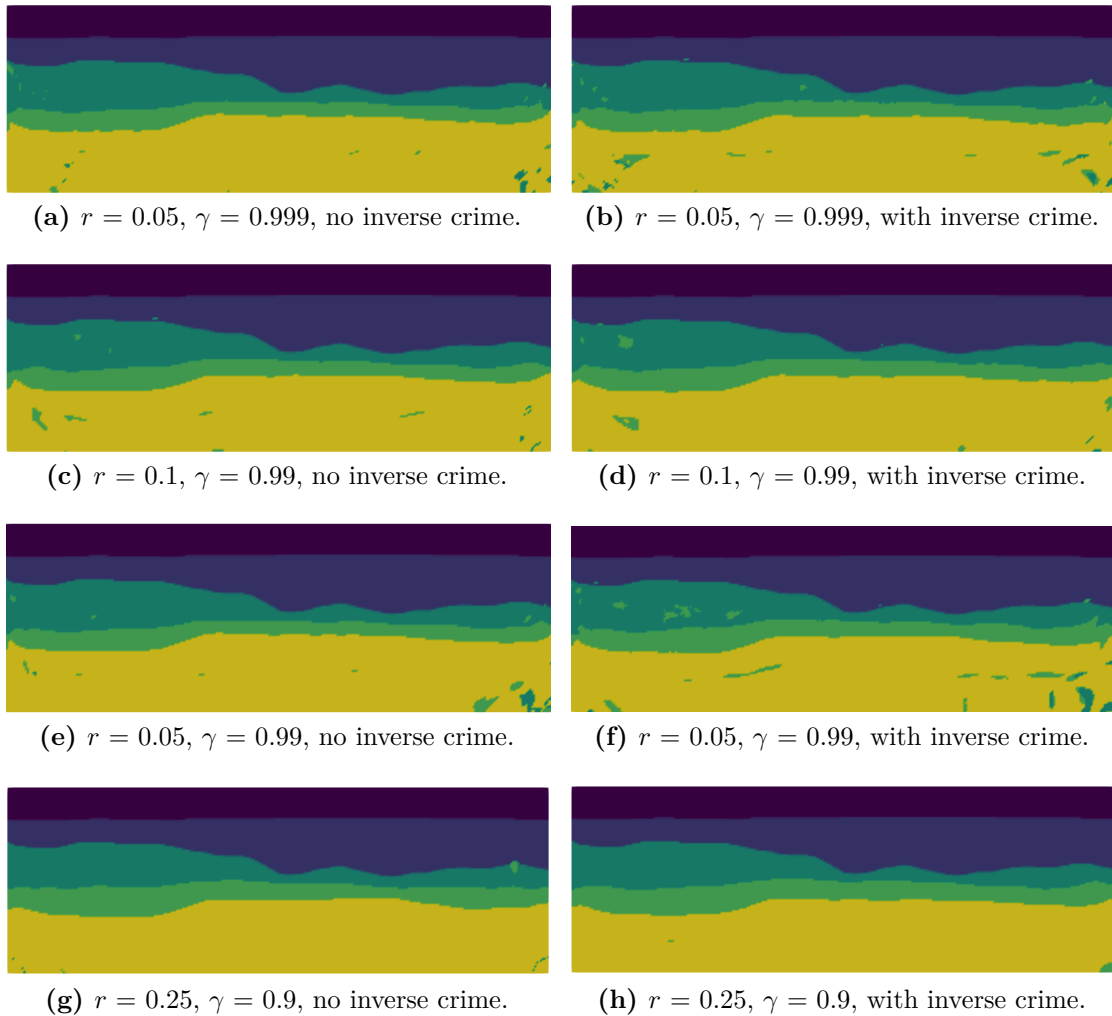
Figure 5.58 − Fixed ToS taking inverse crime into account on the right column, and ignoring it on the left.

In general, the expected trend of more artifacts when the inverse crime is avoided can be observed. In particular, in Figures 5.58d and 5.58f reservoir artifacts appear more frequently on the otherwise well defined salt layer, besides the spurious inclusions at the depper layers, more visible in Figures 5.58b and 5.58f. Most notably, Figures 5.58d and 5.58h indicates that higher spatial filter weights r can dampen the impact of noise, while the same effect cannot be observed for the stabilization filter weight ranging from 0.9 to 0.999.

Figure 5.59 presents the comparative plots of the objective function both under inverse crime condition (in blue) and with addition of gaussian white noise (in red) for the four cases considered. In general, the values are at aleast one order of magnitude higher when white noise is added. Furthermore, when there is a switch in lower and upper bounds L and U at iteration 750, while there is a change in the value of the objective function for

(a) $r = 0.05$, $\gamma = 0.999$.

(b) $r = 0.1$, $\gamma = 0.99$.

(c) $r = 0.05$, $\gamma = 0.99$.

(d) $r = 0.25$, $\gamma = 0.9$.
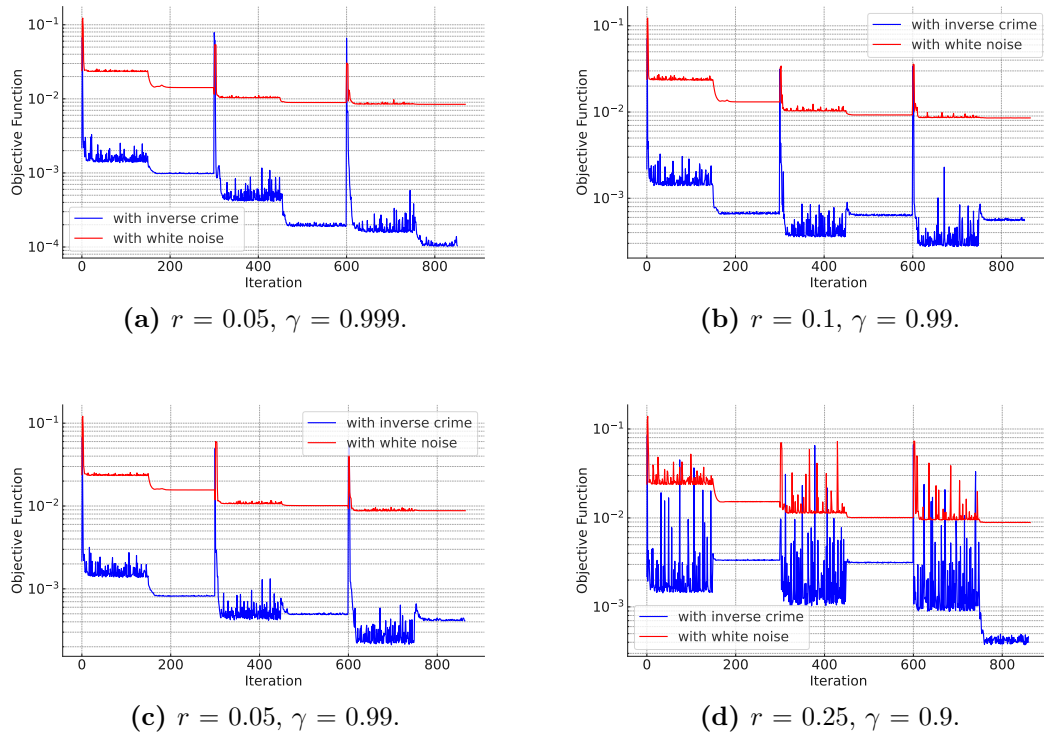
Figure 5.59 − Comparison of objective function with and without taking inverse crime into account.

the cases with inverse crime, the crimeless cases remain at the same level, indicating a possible threshold related to the amount of noise present. It is also of notice that oscilations in value are bigger when $L = 0$ and $U = 1$, that is, when the reservoir region is being distributed within the fixed background. This is reasonable since when $L = 1$ and $U = 2$ the basement is distributed within the reservoir while the background, which occupies a lerger portion of the domain, remains locked out of the inversion.

It can also be observed that higher values of γ dampen considerably the oscilation amplitude. On the other hand, the effect of varying r is not as evident on the behaviour of the objective function.

6 CONCLUSIONS

In this work, a discrete design variable approach to acoustic inversion in the presence of sharp interfaces was investigated. In particular, the velocity model update was performed by solving an Integer Linear Programming problem. Several cases with varying complexity were studied, and the design variable employed varied accordingly. For single material obstacles a binary field described their location, while in cases corresponding to subsurfaces, a multivalued field associated one integer to each structure of interest. The wave propagation was modeled in the time domain, time stepping was performed with an explicit scheme, and the spatial discretization chosen was the finite element method. The adjoint method was used in the sensitivity analysis formulated through a differentiate-then-discretize approach. Two filters were applied to the sensitivities in order to mitigate the appearance of artifacts, and shown to improve the inversion process.

Regarding the numerical examples, first a generic acoust inverse problem was considered. For a few cases taken from the literature, the proposed methodology was as effective as the Level Set method updated by a reaction-diffusion equation, thus indicating its feasibility. At first, a single obstacle case was studied. The parameter sweeping experiment showed the considerable effect that the spatial and stabilization filters have and how the choice of weights is decisive in the sucess of the inversion. In particular, these results demonstrated how the spatial filter is useful in improving reconstruction quality by alleviating the appearance of spurious inclusions. The stabilization filter, on the other hand, was shown to be an essential component to the ILP based approach. The frequency content analysis showed that the whole spectrum was being taken into account because of the restrictiveness of the stability condition over the time step selection, and the sharpness evaluation indicated that the presence of a velocity discontinuity is more impactful than how large the discontinuity is. The case with two obstacles had poor results, showcasing the high dependency of the reconstruction on the source/receiver illumination, which is to be expected. The inversion then was improved by a continuation approach that limited the frequency content of the data with low-pass filters. Next, a 3D example was presented as evidence of the feasibility of applying the methodology to three dimensional problems.

Subsequently, cases pertaining to Full Waveform were studied. A salt identification problem highlighted differences with respect to a Level Set method that employs the Hamilton–Jacobi equation for the curve update. Thereafter, a subsurface velocity model representative of the Santos basin was inverted with different approaches. After showing the limitations with a "regular" continuous FWI approach, the salt layer was located using the binary design variable used throughout the work. Afterwards, the multimaterial

approach with multivalued integer design variables was shown to be incompatible with the stabilization filter, a fundamental component in the proposed integer variable procedure. This prompted the introduction of a multimaterial sequential approach still compatible with the Adam based suavization scheme. The sequential strategy was shown to be reasonably successfull in identifying the salt layer and reservoir, and also in locating the reservoir when the top of salt region is known. The impact of the weights of the stabilization and spatial filters were evaluated for the fixed top of salt case, and the impact of the inverse crime on the results obtained was discussed.

In summary, the work showed the reasonability of the Integer Linear Programming approach if combined with appropriate filters, in this instance taken from Topology Optimization and Machine Learning. Furthermore, the strategy was able to recover obstacles and structures in a more generic acoustic medium setting, and additionally in the specific context of Full Waveform Inversion. In this application, the proposed methodology succeeded in locating not only the salt layer, it also identified the reservoir region where the top of salt is known. In particular, the fixed top of salt represents a more realistic scenario for FWI in a subsurface imaging workflow.

Nevertheless, there are limitations to the current methodology. In the same way that information below the salt layer is amplified with the introduction of the integer approach, so is the noise. The artifacts which appear in the bottom corner regions are present in almost all cases, and currently can only be suppressed by increasing the spatial filter. Since this filter also harms the identification of the reservoir interface, a compromise between artifact suppression and interface detection has to be made. In that regard, delineating the reservoir while avoiding artifacts remains a challenge.

In face of these challenges and considering the scope of the current work, one possible next step would be exploring artifact mitigation strategies. Perhaps morphologic operations like erosion (SIGMUND, 2007) to eliminate small inclusions, or maybe higher order local approximation to improve the direction search. In addition, more realistic physics models could be taken into account, such as elastic wave propagation and orthotropic constitutive models. Another improvement would be to do the explicit time stepping wave propagation with GPUs, since this type of architecture is ideal for the repeated matrix vector multiplications typical of the time domain approach.

REFERENCES

AFANASIEV, M.; BOEHM, C.; DRIEL, M. van; KRISCHER, L.; RIETMANN, M.; MAY, D. A.; KNEPLEY, M. G.; FICHTNER, A. Modular and flexible spectral-element waveform modelling in two and three dimensions. **Geophysical Journal International**, v. 216, n. 3, p. 1675–1692, 2019. Cited 4 times in pages 18, 28, 29, and 70.

AGUDO, O. C.; GUASCH, L.; HUTHWAITE, P.; WARNER, M. 3d imaging of the breast using full-waveform inversion. In: **Proc. Int. Workshop Med. Ultrasound Tomogr.** [S.l.: s.n.], 2018. p. 99–110. Cited in page 20.

AKI, K.; RICHARDS, P. G. **Quantitative seismology**. [S.l.: s.n.], 2002. Cited in page 27.

ALBUQUERQUE, Y. F.; LAURAIN, A.; YOUSEPT, I. Level set–based shape optimization approach for sharp-interface reconstructions in time-domain full waveform inversion. **SIAM Journal on Applied Mathematics**, v. 81, n. 3, p. 939–964, 2021. Disponível em: ⟨https://doi.org/10.1137/20M1378090⟩. Cited in page 23.

ALBUQUERQUE, Y. F.; LAURAIN, A.; YOUSEPT, I. Level set–based shape optimization approach for sharp-interface reconstructions in time-domain full waveform inversion. **SIAM Journal on Applied Mathematics**, SIAM, v. 81, n. 3, p. 939–964, 2021. Cited 5 times in pages 25, 74, 76, 78, and 80.

ALKHALIFAH, T. Scattering-angle based filtering of the waveform inversion gradients. **Geophysical Journal International**, v. 200, n. 1, p. 363–373, 11 2014. ISSN 0956-540X. Disponível em: ⟨https://doi.org/10.1093/gji/ggu379⟩. Cited in page 22.

ALNÆS, M.; BLECHTA, J.; HAKE, J.; JOHANSSON, A.; KEHLET, B.; LOGG, A.; RICHARDSON, C.; RING, J.; ROGNES, M. E.; WELLS, G. N. The fenics project version 1.5. **Archive of Numerical Software**, v. 3, n. 100, 2015. Cited in page 49.

ALNÆS, M. S.; LOGG, A.; ØLGAARD, K. B.; ROGNES, M. E.; WELLS, G. N. Unified form language: A domain-specific language for weak formulations of partial differential equations. **ACM Transactions on Mathematical Software (TOMS)**, ACM New York, NY, USA, v. 40, n. 2, p. 1–37, 2014. Cited in page 50.

ANAGAW, A. Y.; SACCHI, M. D. Full waveform inversion with total variation regularization. In: **Recovery-CSPG CSEG CWLS Convention**. [S.l.: s.n.], 2011. p. 1–4. Cited in page 23.

ANDREASEN, C. S.; ELINGAARD, M. O.; AAGE, N. Level set topology and shape optimization by density methods using cut elements with length scale control. **Structural and Multidisciplinary Optimization**, Springer, v. 62, p. 685–707, 2020. Cited in page 70.

ATKIN, R. J.; FOX, N. **An introduction to the theory of elasticity**. [S.l.]: Courier Corporation, 2005. Cited in page 32.

BALAY, S.; GROPP, W. D.; MCINNES, L. C.; SMITH, B. F. Efficient management of parallelism in object oriented numerical software libraries. In: ARGE, E.; BRUASET, A. M.; LANGTANGEN, H. P. (Ed.). **Modern Software Tools in Scientific Computing**. [S.l.]: Birkhäuser Press, 1997. p. 163–202. Cited in page 50.

BARCLAY, F.; BRUUN, A.; RASMUSSEN, K. B.; ALFARO, J. C.; COOKE, A.; COOKE, D.; SALTER, D.; GODFREY, R.; LOWDEN, D.; MCHUGO, S. et al. Seismic inversion: Reading between the lines. **Oilfield Review**, v. 20, n. 1, p. 42–63, 2008. Cited in page 18.

BENDSØE, M. P. Optimal shape design as a material distribution problem. **Structural optimization**, Springer, v. 1, n. 4, p. 193–202, 1989. Cited 2 times in pages 25 and 38.

BENDSØE, M. P.; KIKUCHI, N. Generating optimal topologies in structural design using a homogenization method. **Computer methods in applied mechanics and engineering**, Elsevier, v. 71, n. 2, p. 197–224, 1988. Cited 3 times in pages 19, 24, and 25.

BENDSØE, M. P.; SIGMUND, O. Material interpolation schemes in topology optimization. **Archive of applied mechanics**, Springer, v. 69, n. 9, p. 635–654, 1999. Cited in page 24.

BERENGER, J.-P. A perfectly matched layer for the absorption of electromagnetic waves. **Journal of computational physics**, Elsevier, v. 114, n. 2, p. 185–200, 1994. Cited in page 34.

BILLETTE, F.; BRANDSBERG-DAHL, S. The 2004 bp velocity benchmark. In: EUROPEAN ASSOCIATION OF GEOSCIENTISTS & ENGINEERS. **67th EAGE Conference & Exhibition**. [S.l.], 2005. p. cp–1. Cited in page 23.

BOURDIN, B. Filters in topology optimization. **International journal for numerical methods in engineering**, Wiley Online Library, v. 50, n. 9, p. 2143–2158, 2001. Cited in page 53.

BRIGHAM, E. O. **The fast Fourier transform and its applications**. [S.l.]: Prentice-Hall, Inc., 1988. Cited in page 57.

BUNKS, C.; SALECK, F. M.; ZALESKI, S.; CHAVENT, G. Multiscale seismic waveform inversion. **Geophysics**, Society of Exploration Geophysicists, v. 60, n. 5, p. 1457–1473, 1995. Cited in page 66.

BYUN, J.-K.; LEE, J.-H.; PARK, I.-H.; LEE, H.-B.; CHOI, K.; HAHN, S.-Y. Inverse problem application of topology optimization method with mutual energy concept and design sensitivity. **IEEE Transactions on Magnetics**, IEEE, v. 36, n. 4, p. 1144–1147, 2000. Cited in page 25.

CARCIONE, J. M. **Wave fields in real media: Wave propagation in anisotropic, anelastic, porous and electromagnetic media**. [S.l.]: Elsevier, 2007. Cited in page 31.

CERJAN, C.; KOSLOFF, D.; KOSLOFF, R.; RESHEF, M. A nonreflecting boundary condition for discrete acoustic and elastic wave equations. **Geophysics**, Society of Exploration Geophysicists, v. 50, n. 4, p. 705–708, 1985. Cited in page 33.

CHAILLAT, S.; BONNET, M.; SEMBLAT, J.-F. A multi-level fast multipole bem for 3-d elastodynamics in the frequency domain. **Computer Methods in Applied Mechanics and Engineering**, Elsevier, v. 197, n. 49-50, p. 4233–4249, 2008. Cited in page 27.

CHARARA, M.; BARNES, C.; TARANTOLA, A. Full waveform inversion of seismic data for a viscoelastic medium. **Methods and applications of inversion**, Springer, p. 68–81, 2005. Cited in page 21.

CHIN-JOE-KONG, M.; MULDER, W. A.; VELDHUIZEN, M. V. Higher-order triangular and tetrahedral finite elements with mass lumping for solving the wave equation. **Journal of Engineering Mathematics**, Springer, v. 35, n. 4, p. 405–426, 1999. Cited in page 49.

COHEN, G. **Higher-order numerical methods for transient wave equations**. [S.l.]: Springer Science & Business Media, 2001. Cited 2 times in pages 32 and 33.

COHEN, G.; PERNET, S. **Finite element and discontinuous Galerkin methods for transient wave equations**. [S.l.]: Springer, 2017. Cited in page 34.

COLTON, D. L.; KRESS, R.; KRESS, R. **Inverse acoustic and electromagnetic scattering theory**. [S.l.]: Springer, 1998. v. 93. Cited in page 68.

DEATON, J. D.; GRANDHI, R. V. A survey of structural and multidisciplinary continuum topology optimization: post 2000. **Structural and Multidisciplinary Optimization**, Springer, v. 49, n. 1, p. 1–38, 2014. Cited 2 times in pages 24 and 26.

DORN, O.; WU, Y. Shape reconstruction in seismic full waveform inversion using a level set approach and time reversal. **Journal of Computational Physics**, Elsevier, v. 427, p. 110059, 2021. Cited 2 times in pages 23 and 25.

ENGL, H. W.; HANKE, M.; NEUBAUER, A. **Regularization of inverse problems**. [S.l.]: Springer Science & Business Media, 1996. v. 375. Cited 2 times in pages 19 and 53.

ENGQUIST, B.; MAJDA, A. Absorbing boundary conditions for numerical simulation of waves. **Proceedings of the National Academy of Sciences**, National Acad Sciences, v. 74, n. 5, p. 1765–1766, 1977. Cited 2 times in pages 33 and 34.

EPANOMERITAKIS, I.; AKÇELIK, V.; GHATTAS, O.; BIELAK, J. A newton-cg method for large-scale three-dimensional elastic full-waveform seismic inversion. **Inverse Problems**, IOP Publishing, v. 24, n. 3, p. 034015, 2008. Cited in page 22.

ESSER, E.; GUASCH, L.; HERRMANN, F. J.; WARNER, M. Constrained waveform inversion for automatic salt flooding. **The Leading Edge**, Society of Exploration Geophysicists, v. 35, n. 3, p. 235–239, 2016. Cited in page 23.

ETIENNE, V.; OPERTO, S.; VIRIEUX, J.; JIA, Y. Computational issues and strategies related to full waveform inversion in 3d elastic media: Methodological developments. In: **SEG Technical Program Expanded Abstracts 2010**. [S.l.]: Society of Exploration Geophysicists, 2010. p. 1050–1054. Cited in page 22.

FICHTNER, A. **Full seismic waveform modelling and inversion**. [S.l.]: Springer Science & Business Media, 2010. Cited 7 times in pages 21, 27, 28, 29, 31, 48, and 57.

GAO, K.; HUANG, L. Acoustic-and elastic-waveform inversion with total generalized p-variation regularization. **Geophysical Journal International**, Oxford University Press, v. 218, n. 2, p. 933–957, 2019.   Cited in page 23.

GAUTHIER, O.; VIRIEUX, J.; TARANTOLA, A. Two-dimensional nonlinear inversion of seismic waveforms: Numerical results. **Geophysics**, Society of Exploration Geophysicists, v. 51, n. 7, p. 1387–1403, 1986.   Cited in page 21.

GÉLIS, C.; VIRIEUX, J.; GRANDJEAN, G. Two-dimensional elastic full waveform inversion using born and rytov formulations in the frequency domain. **Geophysical Journal International**, Blackwell Publishing Ltd Oxford, UK, v. 168, n. 2, p. 605–633, 2007.   Cited in page 21.

GONÇALVES, J.; SILVA, E. Salt reconstruction in full-waveform inversion using topology optimization techniques. **Geophysical Journal International**, Oxford University Press, v. 234, n. 2, p. 1484–1504, 2023.   Cited in page 25.

GONCALVES, J. F.; MOREIRA, J. B.; SALAS, R. A.; GHORBANI, M. M.; RUBIO, W. M.; SILVA, E. C. Identification problem of acoustic media in the frequency domain based on the topology optimization method. **Structural and Multidisciplinary Optimization**, Springer, v. 62, n. 3, p. 1041–1059, 2020.   Cited 3 times in pages 25, 30, and 38.

GONCALVES, J. F.; SILVA, E. C. An adaptive material interpolation for the reconstruction of p-wave velocity models with sharp interfaces using the topology optimization method. **Journal of Theoretical and Computational Acoustics**, World Scientific, p. 2150016, 2021.   Cited in page 25.

GROETSCH, C. W.; GROETSCH, C. **Inverse problems in the mathematical sciences**. [S.l.]: Springer, 1993. v. 52.   Cited in page 17.

GROTE, M. J.; SIM, I. Efficient pml for the wave equation. **arXiv preprint arXiv:1001.0319**, 2010.   Cited in page 34.

GUASCH, L. 3d elastic full-waveform inversion. Imperial College London, 2012.   Cited 2 times in pages 20 and 21.

GUASCH, L.; AGUDO, O. C.; TANG, M.-X.; NACHEV, P.; WARNER, M. Full-waveform inversion imaging of the human brain. **NPJ digital medicine**, Nature Publishing Group, v. 3, n. 1, p. 1–12, 2020.   Cited 2 times in pages 18 and 20.

GUASCH, L.; WARNER, M.; HERRMANN, F. Constrained waveform inversion - automatic salt flooding with inclusions. European Association of Geoscientists & Engineers, v. 2016, n. 1, p. 1–5, 2016. ISSN 2214-4609. Disponível em: ⟨https://www.earthdoc.org/content/papers/10.3997/2214-4609.201601547⟩.   Cited in page 23.

GUASCH, L.; WARNER, M.; STEKL, I.; UMPLEBY, A. 3d elastic wavefield inversion in the time domain. In: EUROPEAN ASSOCIATION OF GEOSCIENTISTS & ENGINEERS. **72nd EAGE Conference and Exhibition incorporating SPE EUROPEC 2010**. [S.l.], 2010. p. cp–161.   Cited in page 22.

GUEST, J. K.; PRÉVOST, J. H.; BELYTSCHKO, T. Achieving minimum length scale in topology optimization using nodal design variables and projection functions. **International journal for numerical methods in engineering**, Wiley Online Library, v. 61, n. 2, p. 238–254, 2004. Cited in page 25.

GUO, Z.; HOOP, M. V. de. Shape optimization in full waveform inversion with sparse blocky model representations. **Proceedings of the Project Review**, v. 1, p. 189–208, 2012. Cited in page 23.

GUO, Z.; HOOP, M. V. de. Shape optimization and level set method in full waveform inversion with 3d body reconstruction. In: **SEG Technical Program Expanded Abstracts 2013**. [S.l.]: Society of Exploration Geophysicists, 2013. p. 1079–1083. Cited in page 23.

HAM, D.; HOMOLYA, M.; LANGE, M.; KIRBY, R.; MITCHELL, L. Finat/finat: a smarter library of finite elements. Cited in page 50.

HINZE, M.; PINNAU, R.; ULBRICH, M.; ULBRICH, S. **Optimization with PDE constraints**. [S.l.]: Springer Science & Business Media, 2008. v. 23. Cited in page 42.

HOMOLYA, M.; MITCHELL, L.; LUPORINI, F.; HAM, D. A. Tsfc: a structure-preserving form compiler. **SIAM Journal on Scientific Computing**, SIAM, v. 40, n. 3, p. C401–C428, 2018. Cited in page 50.

HU, W.; CHEN, J.; LIU, J.; ABUBAKAR, A. Retrieving low wavenumber information in fwi: An overview of the cycle-skipping phenomenon and solutions. **IEEE Signal Processing Magazine**, IEEE, v. 35, n. 2, p. 132–141, 2018. Cited in page 22.

HUANG, X.; XIE, Y. Convergent and mesh-independent solutions for the bi-directional evolutionary structural optimization method. **Finite elements in analysis and design**, Elsevier, v. 43, n. 14, p. 1039–1049, 2007. Cited in page 91.

HUANG, X.; XIE, Y. M. Bi-directional evolutionary topology optimization of continuum structures with one or multiple materials. **Computational Mechanics**, Springer, v. 43, n. 3, p. 393–401, 2009. Cited in page 26.

HUDEC, M. R.; JACKSON, M. P. Terra infirma: Understanding salt tectonics. **Earth-Science Reviews**, Elsevier, v. 82, n. 1-2, p. 1–28, 2007. Cited 2 times in pages 19 and 20.

HUGHES, T. J. **The finite element method: linear static and dynamic finite element analysis**. [S.l.]: Courier Corporation, 2012. Cited 2 times in pages 35 and 49.

IRONS, T. **Sigsbee2 Models**. 2001. Disponível em: ⟨https://reproducibility.org/RSF/book/data/sigsbee/paper_html/node3.html⟩. Cited in page 23.

KADU, A.; LEEUWEN, T. V.; MULDER, W. A parametric level-set approach for seismic full-waveform inversion. In: _____. **SEG Technical Program Expanded Abstracts 2016**. [s.n.], 2016. p. 1146–1150. Disponível em: ⟨https://library.seg.org/doi/abs/10.1190/segam2016-13870276.1⟩. Cited 4 times in pages 23, 25, 79, and 102.

KELLER, J. B. Inverse problems. **The American Mathematical Monthly**, Mathematical Association of America, v. 83, n. 2, p. 107–118, 1976. ISSN 00029890, 19300972. Disponível em: ⟨http://www.jstor.org/stable/2976988⟩. Cited in page 17.

KINGMA, D. P.; BA, J. Adam: A method for stochastic optimization. **arXiv preprint arXiv:1412.6980**, 2014. Cited 2 times in pages 46 and 54.

KIRSCH, A. et al. **An introduction to the mathematical theory of inverse problems**. [S.l.]: Springer, 2011. v. 120. Cited in page 17.

KOHN, R. V.; STRANG, G. Optimal design and relaxation of variational problems, i. **Communications on Pure and Applied Mathematics**, v. 39, n. 1, p. 113–137, 1986. Disponível em: ⟨https://onlinelibrary.wiley.com/doi/abs/10.1002/cpa.3160390107⟩. Cited 2 times in pages 19 and 25.

KOMATITSCH, D.; VILOTTE, J.-P. The spectral element method: an efficient tool to simulate the seismic response of 2d and 3d geological structures. **Bulletin of the seismological society of America**, The Seismological Society of America, v. 88, n. 2, p. 368–392, 1998. Cited 2 times in pages 28 and 49.

KUZUOGLU, M.; MITTRA, R. Frequency dependence of the constitutive parameters of causal perfectly matched anisotropic absorbers. **IEEE Microwave and Guided wave letters**, IEEE, v. 6, n. 12, p. 447–449, 1996. Cited in page 34.

LAILLY, P.; BEDNAR, J. The seismic inverse problem as a sequence of before stack migrations. 1983. Cited in page 20.

LANZNASTER, D.; CASTRO, P. de; EMMENDOERFER, H.; MENDONÇA, P.; SILVA, E.; FANCELLO, E. A level-set approach based on reaction–diffusion equation applied to inversion problems in acoustic wave propagation. **Inverse Problems**, IOP Publishing, v. 37, n. 2, p. 025009, 2021. Cited 4 times in pages 25, 52, 61, and 63.

LARSEN, U. D.; SIGMUND, O.; BOUWSTA, S. Design and fabrication of compliant micromechanisms and structures with negative poisson's ratio. **Journal of microelectromechanical systems**, IEEE, v. 6, n. 2, p. 99–106, 1997. Cited in page 25.

LAZAROV, B. S.; SIGMUND, O. Filters in topology optimization based on helmholtz-type differential equations. **International Journal for Numerical Methods in Engineering**, Wiley Online Library, v. 86, n. 6, p. 765–781, 2011. Cited in page 45.

LI, Y.; ALKHALIFAH, T. Extended full waveform inversion with matching filter. **Geophysical Prospecting**, v. 69, n. 7, p. 1441–1454, 2021. Cited in page 22.

LI, Y. E.; DEMANET, L. Full-waveform inversion with extrapolated low-frequency data. **Geophysics**, Society of Exploration Geophysicists, v. 81, n. 6, p. R339–R348, 2016. Cited in page 22.

LIMA, C. R. de; MELLO, L. A.; LIMA, R. G.; SILVA, E. C. Electrical impedance tomography through constrained sequential linear programming: a topology optimization approach. **Measurement Science and Technology**, IOP Publishing, v. 18, n. 9, p. 2847, 2007. Cited in page 25.

LIN, Y.; HUANG, L. Acoustic-and elastic-waveform inversion using a modified total-variation regularization scheme. **Geophysical Journal International**, Oxford University Press, v. 200, n. 1, p. 489–502, 2014. Cited 2 times in pages 23 and 25.

LIU, Y.; TENG, J.; XU, T.; WANG, Y.; LIU, Q.; BADAL, J. Robust time-domain full waveform inversion with normalized zero-lag cross-correlation objective function. **Geophysical Journal International**, v. 209, n. 1, p. 106–122, 12 2016. ISSN 0956-540X. Disponível em: ⟨https://doi.org/10.1093/gji/ggw485⟩. Cited in page 22.

LOUIS, A. K. Medical imaging: state of the art and future development. IOP Publishing, v. 8, n. 5, p. 709–738, oct 1992. Disponível em: ⟨https://doi.org/10.1088/0266-5611/8/5/003⟩. Cited in page 17.

LUCKA, F.; PÉREZ-LIVA, M.; TREEBY, B. E.; COX, B. T. High resolution 3d ultrasonic breast imaging by time-domain full waveform inversion. **Inverse Problems**, IOP Publishing, v. 38, n. 2, p. 025008, 2021. Cited in page 70.

MANUAL, C. U. Ibm ilog cplex optimization studio. **Version**, v. 12, p. 1987–2018, 1987. Cited in page 29.

Large-scale 3D Gravity Data Space Inversion in Hydrocarbon Exploration, All Days de **SEG International Exposition and Annual Meeting**, (SEG International Exposition and Annual Meeting, All Days). SEG-2014-1078. Cited in page 17.

M.C.E, A. G. M. M. LVIII. The limits of economy of material in frame-structures. **The London, Edinburgh, and Dublin Philosophical Magazine and Journal of Science**, v. 8, n. 47, p. 589–597, nov. 1904. ISSN 1941-5982. Disponível em: ⟨https://doi.org/10.1080/14786440409463229⟩. Cited in page 24.

MELLO, L. A. M.; LIMA, C. R. D.; AMATO, M. B. P.; LIMA, R. G.; SILVA, E. C. N. Three-dimensional electrical impedance tomography: a topology optimization approach. **IEEE Transactions on Biomedical Engineering**, IEEE, v. 55, n. 2, p. 531–540, 2008. Cited in page 25.

MOREIRA, J. B.; GONÇALVES, J. F.; SIVAPURAM, R.; CARMO, B. S.; SILVA, E. C. Topology optimization applied to the acoustic medium inverse problem in the time domain using integer linear programming. **Structural and Multidisciplinary Optimization**, Springer, v. 66, n. 4, p. 78, 2023. Cited 3 times in pages 25, 29, and 30.

MUNK, W. H.; WORCESTER, P. F. Ocean acoustic tomography. **Oceanography**, Oceanography Society, v. 1, n. 1, p. 8–10, 1988. ISSN 10428275, 2377617X. Disponível em: ⟨http://www.jstor.org/stable/43925296⟩. Cited in page 17.

NGUYEN, L. T.; NESTOROVIĆ, T. Reconstructing disturbance zones ahead of the tunnel face by elastic waveform inversion supported by a parametric level-set representation. **Soil Dynamics and Earthquake Engineering**, Elsevier, v. 115, p. 606–621, 2018. Cited in page 19.

NOCEDAL, J.; WRIGHT, S. J. **Numerical optimization**. [S.l.]: Springer, 1999. Cited 2 times in pages 84 and 97.

PETERSOHN, E. Pre-salt: Exploration trend and 5 years perspective. European Association of Geoscientists and; Engineers, v. 2021, n. 1, p. 1–5, 2021. ISSN 2214-4609. Disponível em: ⟨https://www.earthdoc.org/content/papers/10.3997/2214-4609.202183026⟩. Cited in page 22.

PICELLI, R.; RANJBARZADEH, S.; SIVAPURAM, R.; GIORIA, R.; SILVA, E. Topology optimization of binary structures under design-dependent fluid-structure interaction loads. **Structural and Multidisciplinary Optimization**, Springer, v. 62, n. 4, p. 2101–2116, 2020. Cited 2 times in pages 29 and 41.

PLESSIX, R.-E.; MICHELET, S.; RYNJA, H.; KUEHL, H.; PERKINS, C.; MAAG, J. de; HATCHELL, P. Some 3d applications of full waveform inversion. In: EUROPEAN ASSOCIATION OF GEOSCIENTISTS & ENGINEERS. **72nd EAGE Conference and Exhibition-Workshops and Fieldtrips**. [S.l.], 2010. p. cp–162. Cited in page 22.

PRATT, R. G. Seismic waveform inversion in the frequency domain, part 1: Theory and verification in a physical scale model. **Geophysics**, Society of Exploration Geophysicists, v. 64, n. 3, p. 888–901, 1999. Cited in page 21.

PRATT, R. G.; SHIPP, R. M. Seismic waveform inversion in the frequency domain, part 2: Fault delineation in sediments using crosshole data. **Geophysics**, Society of Exploration Geophysicists, v. 64, n. 3, p. 902–914, 1999. Cited in page 21.

RATHGEBER, F.; HAM, D. A.; MITCHELL, L.; LANGE, M.; LUPORINI, F.; MCRAE, A. T. T.; BERCEA, G.-T.; MARKALL, G. R.; KELLY, P. H. J. Firedrake: Automating the finite element method by composing abstractions. **ACM Trans. Math. Softw.**, Association for Computing Machinery, New York, NY, USA, v. 43, n. 3, dec 2016. ISSN 0098-3500. Disponível em: ⟨https://doi.org/10.1145/2998441⟩. Cited in page 29.

RATHGEBER, F.; HAM, D. A.; MITCHELL, L.; LANGE, M.; LUPORINI, F.; MCRAE, A. T. T.; BERCEA, G.-T.; MARKALL, G. R.; KELLY, P. H. J. Firedrake: Automating the finite element method by composing abstractions. **ACM Trans. Math. Softw.**, Association for Computing Machinery, New York, NY, USA, v. 43, n. 3, dec 2016. ISSN 0098-3500. Disponível em: ⟨https://doi.org/10.1145/2998441⟩. Cited 2 times in pages 48 and 49.

ROBERTS, K. J.; OLENDER, A.; FRANCESCHINI, L. **spyro V0.1.0**. Zenodo, 2021. Disponível em: ⟨https://doi.org/10.5281/zenodo.5164113⟩. Cited 2 times in pages 49 and 50.

ROBERTS, K. J.; OLENDER, A.; FRANCESCHINI, L.; KIRBY, R. C.; GIORIA, R. S.; CARMO, B. S. spyro: a firedrake-based wave propagation and full-waveform-inversion finite-element solver. **Geoscientific Model Development**, Copernicus GmbH, v. 15, n. 23, p. 8639–8667, 2022. Cited 3 times in pages 21, 29, and 57.

ROMDHANE, A.; QUERENDEZ, E. Co2 characterization at the sleipner field with full waveform inversion: Application to synthetic and real data. **Energy procedia**, Elsevier, v. 63, p. 4358–4365, 2014. Cited in page 20.

RUDER, S. An overview of gradient descent optimization algorithms. **arXiv preprint arXiv:1609.04747**, 2016. Cited in page 46.

RYUZONO, K.; YASHIRO, S.; NAGAI, H.; TOYAMA, N. Topology optimization-based damage identification using visualized ultrasonic wave propagation. **Materials**, MDPI, v. 13, n. 1, p. 33, 2019. Cited in page 25.

SANTOSA, F. et al. **Inverse problems of acoustic and elastic waves**. [S.l.]: Siam, 1984. v. 14. Cited in page 20.

SEARS, T.; SINGH, S.; BARTON, P. Elastic full waveform inversion of multi-component obc seismic data. **Geophysical Prospecting**, European Association of Geoscientists and; Engineers, v. 56, n. 6, p. 843–862, 2008. ISSN 1365-2478. Disponível em: ⟨https://www.earthdoc.org/content/journals/10.1111/j.1365-2478.2008.00692.x⟩. Cited in page 21.

SEIDL, R.; RANK, E. Iterative time reversal based flaw identification. **Computers & Mathematics with Applications**, Elsevier, v. 72, n. 4, p. 879–892, 2016. Cited 4 times in pages 20, 29, 39, and 40.

SEIDL, R.; RANK, E. Full waveform inversion for ultrasonic flaw identification. In: AIP PUBLISHING LLC. **AIP Conference Proceedings**. [S.l.], 2017. v. 1806, n. 1, p. 090013. Cited in page 36.

SHEN, X.; JIANG, L.; DELLINGER, J.; BRENDERS, A.; KUMAR, C.; JAMES, M.; ETGEN, J.; MEAUX, D.; WALTERS, R.; ABDULLAYEV, N. High-resolution full-waveform inversion for structural imaging in exploration. In: _____. **SEG Technical Program Expanded Abstracts 2018**. [s.n.], 2018. p. 1098–1102. Disponível em: ⟨https://library.seg.org/doi/abs/10.1190/segam2018-2997202.1⟩. Cited in page 23.

SHERIFF, R. E.; GELDART, L. P. **Exploration seismology**. [S.l.]: Cambridge university press, 1995. Cited in page 19.

SHRAGGE, J. Acoustic wave propagation in tilted transversely isotropic media: Incorporating topography. **Geophysics**, Society of Exploration Geophysicists, v. 81, n. 5, p. C265–C278, 2016. Cited in page 28.

SIGMUND, O. Morphology-based black and white filters for topology optimization. **Structural and Multidisciplinary Optimization**, Springer, v. 33, p. 401–424, 2007. Cited in page 107.

SIGMUND, O.; MAUTE, K. Sensitivity filtering from a continuum mechanics perspective. **Structural and Multidisciplinary Optimization**, Springer, v. 46, n. 4, p. 471–475, 2012. Cited in page 54.

SIGMUND, O.; MAUTE, K. Topology optimization approaches. **Structural and Multidisciplinary Optimization**, Springer, v. 48, n. 6, p. 1031–1055, 2013. Cited 2 times in pages 26 and 37.

SIGMUND, O.; PETERSSON, J. Numerical instabilities in topology optimization: a survey on procedures dealing with checkerboards, mesh-dependencies and local minima. **Structural optimization**, Springer, v. 16, n. 1, p. 68–75, 1998. Cited 3 times in pages 24, 25, and 45.

SIGMUND, O.; TORQUATO, S. Composites with extremal thermal expansion coefficients. **Applied Physics Letters**, American Institute of Physics, v. 69, n. 21, p. 3203–3205, 1996. Cited in page 25.

SIRGUE, L.; BARKVED, O.; GESTEL, J. V.; ASKIM, O.; KOMMEDAL, J. 3d waveform inversion on valhall wide-azimuth obc. In: EUROPEAN ASSOCIATION OF GEOSCIENTISTS & ENGINEERS. **71st EAGE Conference and Exhibition incorporating SPE EUROPEC 2009**. [S.l.], 2009. p. cp–127. Cited in page 22.

SIVAPURAM, R.; PICELLI, R. Topology optimization of binary structures using integer linear programming. **Finite Elements in Analysis and Design**, Elsevier, v. 139, p. 49–61, 2018. Cited in page 40.

SIVAPURAM, R.; PICELLI, R. Topology design of binary structures subjected to design-dependent thermal expansion and fluid pressure loads. **Structural and Multidisciplinary Optimization**, Springer, v. 61, n. 5, p. 1877–1895, 2020. Cited 2 times in pages 27 and 29.

SIVAPURAM, R.; PICELLI, R.; XIE, Y. M. Topology optimization of binary microstructures involving various non-volume constraints. **Computational Materials Science**, Elsevier, v. 154, p. 405–425, 2018. Cited 3 times in pages 26, 29, and 91.

SIVAPURAM, R.; PICELLI, R.; XIE, Y. M. Topology optimization of binary microstructures involving various non-volume constraints. **Computational Materials Science**, Elsevier, v. 154, p. 405–425, 2018. Cited in page 26.

SIVAPURAM, R.; PICELLI, R.; YOON, G. H.; YI, B. On the design of multimaterial structural topologies using integer programming. **Computer Methods in Applied Mechanics and Engineering**, Elsevier, v. 384, p. 114000, 2021. Cited 3 times in pages 11, 89, and 91.

SOCHACKI, J.; KUBICHEK, R.; GEORGE, J.; FLETCHER, W.; SMITHSON, S. Absorbing boundary conditions and surface waves. **Geophysics**, Society of Exploration Geophysicists, v. 52, n. 1, p. 60–71, 1987. Cited in page 75.

SOUZA, J. F. de; MOREIRA, J. B. D.; ROBERTS, K. J.; GAIOSO, R. d. R. A.; GOMI, E. S.; SILVA, E. C. N.; SENGER, H. `simwave`–a finite difference simulator for acoustic waves propagation. **arXiv preprint arXiv:2201.05278**, 2022. Cited in page 30.

SPENCER, A. J. M. **Continuum mechanics**. [S.l.]: Courier Corporation, 2004. Cited in page 31.

STOLPE, M.; SVANBERG, K. An alternative interpolation scheme for minimum compliance topology optimization. **Structural and Multidisciplinary Optimization**, Springer, v. 22, n. 2, p. 116–124, 2001. Cited in page 37.

SUN, H.; DEMANET, L. Extrapolated full-waveform inversion with deep learning efwi-cnn. **Geophysics**, GeoScienceWorld, v. 85, n. 3, p. R275–R288, 2020. Cited in page 22.

TAKEUCHI, N.; GELLER, R. J. Optimally accurate second order time-domain finite difference scheme for computing synthetic seismograms in 2-d and 3-d media. **Physics of the earth and planetary interiors**, Elsevier, v. 119, n. 1-2, p. 99–131, 2000. Cited in page 28.

TARANTOLA, A. Inversion of seismic reflection data in the acoustic approximation. **Geophysics**, Society of Exploration Geophysicists, v. 49, n. 8, p. 1259–1266, 1984. Cited in page 20.

TRINH, P.-T.; BROSSIER, R.; MÉTIVIER, L.; TAVARD, L.; VIRIEUX, J.; WELLINGTON, P. Efficient 3d elastic fwi using a spectral-element method on cartesian-based mesh. In: ONEPETRO. **2017 SEG International Exposition and Annual Meeting**. [S.l.], 2017. Cited in page 21.

VIRIEUX, J.; ASNAASHARI, A.; BROSSIER, R.; MÉTIVIER, L.; RIBODETTI, A.; ZHOU, W. An introduction to full waveform inversion. In: **Encyclopedia of exploration geophysics**. [S.l.]: Society of Exploration Geophysicists, 2017. p. R1–1. Cited 2 times in pages 35 and 36.

VIRIEUX, J.; CALANDRA, H.; PLESSIX, R.-É. A review of the spectral, pseudo-spectral, finite-difference and finite-element modelling techniques for geophysical imaging. **Geophysical Prospecting**, European Association of Geoscientists & Engineers, v. 59, n. Modelling Methods for Geophysical Imaging: Trends and Perspectives, p. 794–813, 2011. Cited 2 times in pages 27 and 28.

VIRIEUX, J.; OPERTO, S. An overview of full-waveform inversion in exploration geophysics. **Geophysics**, Society of Exploration Geophysicists, v. 74, n. 6, p. WCC1–WCC26, 2009. Cited in page 48.

WANG, P.; ZHANG, Z.; MEI, J.; LIN, F.; HUANG, R. Full-waveform inversion for salt: A coming of age. **The Leading Edge**, v. 38, n. 3, p. 204–213, 03 2019. ISSN 1070-485X. Disponível em: ⟨https://doi.org/10.1190/tle38030204.1⟩. Cited 5 times in pages 23, 29, 39, 40, and 97.

WANG, Y. Frequencies of the ricker wavelet. **Geophysics**, Society of Exploration Geophysicists, v. 80, n. 2, p. A31–A37, 2015. Cited 2 times in pages 34 and 53.

WARNER, M.; GUASCH, L. Adaptive waveform inversion: Theory. **GEOPHYSICS**, v. 81, n. 6, p. R429–R445, 2016. Disponível em: ⟨https://doi.org/10.1190/geo2015-0387.1⟩. Cited in page 22.

WARNER, M.; STEKL, I.; UMPLEBY, A. Full wavefield seismic tomography–iterative forward modelling in 3d. In: EUROPEAN ASSOCIATION OF GEOSCIENTISTS & ENGINEERS. **69th EAGE Conference and Exhibition incorporating SPE EUROPEC 2007**. [S.l.], 2007. p. cp–27. Cited in page 22.

WOLSEY, L. A. **Integer programming**. [S.l.]: John Wiley & Sons, 2020. Cited in page 50.

XIA, L.; XIA, Q.; HUANG, X.; XIE, Y. M. Bi-directional evolutionary structural optimization on advanced structures and materials: a comprehensive review. **Archives of Computational Methods in Engineering**, Springer, v. 25, p. 437–478, 2018. Cited in page 91.

YAO, G.; SILVA, N. V. da; WARNER, M.; WU, D.; YANG, C. Tackling cycle skipping in full-waveform inversion with intermediate data. **Geophysics**, Society of Exploration Geophysicists, v. 84, n. 3, p. R411–R427, 2019. Cited in page 22.

YIN, L.; ANANTHASURESH, G. Topology optimization of compliant mechanisms with multiple materials using a peak function material interpolation scheme. **Structural and Multidisciplinary Optimization**, Springer, v. 23, n. 1, p. 49–62, 2001. Cited 2 times in pages 24 and 37.

ZAOUI, A.; MENANA, H.; FELIACHI, M.; BERTHIAU, G. Inverse problem in nondestructive testing using arrayed eddy current sensors. **Sensors**, v. 10, n. 9, p. 8696–8704, 2010. ISSN 1424-8220. Disponível em: ⟨https://www.mdpi.com/1424-8220/10/9/8696⟩. Cited in page 17.

ZHANG, Z.; MEI, J.; LIN, F.; HUANG, R.; WANG, P. Correcting for salt misinterpretation with full-waveform inversion. In: _____. **SEG Technical Program Expanded Abstracts 2018**. [s.n.], 2018. p. 1143–1147. Disponível em: ⟨https://library.seg.org/doi/abs/10.1190/segam2018-2997711.1⟩. Cited in page 23.

ZHEBEL, E.; MINISINI, S.; KONONOV, A.; MULDER, W. A. A comparison of continuous mass-lumped finite elements with finite differences for 3-d wave propagation. **Geophysical Prospecting**, European Association of Geoscientists & Engineers, v. 62, n. 5, p. 1111–1125, 2014. Cited in page 28.

ZHOU, M.; ROZVANY, G. The coc algorithm, part ii: Topological, geometrical and generalized shape optimization. **Computer methods in applied mechanics and engineering**, Elsevier, v. 89, n. 1-3, p. 309–336, 1991. Cited in page 25.

ZUO, W.; SAITOU, K. Multi-material topology optimization using ordered simp interpolation. **Structural and Multidisciplinary Optimization**, Springer, v. 55, p. 477–491, 2017. Cited in page 24.